

Optomechanical Sensors in the Silicon Photonic Platform

Jesper Max Olof Håkansson

Promotor: prof. dr. ir. D. Van Thourhout
Proefschrift ingediend tot het behalen van de graad van
Doctor in de ingenieurswetenschappen: fotonica



Vakgroep Informatietechnologie
Voorzitter: prof. dr. ir. B. Dhoedt
Faculteit Ingenieurswetenschappen en Architectuur
Academiejaar 2018 - 2019

ISBN 978-94-6355-265-3
NUR 950
Wettelijk depot: D/2019/10.500/73



Universiteit Gent
Faculteit Ingenieurswetenschappen en Architectuur
Vakgroep Informatietechnologie

Promotor: Prof. Dr. Ir. Dries Van Thourhout

Examencommissie:

Em. Prof. Dr. Ir. Daniël De Zutter (voorzitter)	Universiteit Gent
Prof. Dr. Ir. Dries Van Thourhout (promotor)	Universiteit Gent
Prof. Dr. Ir. Peter Bienstman (secretaris)	Universiteit Gent
Prof. Dr. Ir. Bart Kuyken	Universiteit Gent
Dr. Ir. Raphael Van Laer	Universiteit Gent
Prof. Dr. Ir. Filip Beunis	Universiteit Gent
Prof. Dr. Ir. Remy Braive	Université Paris-Sud

Universiteit Gent
Faculteit Ingenieurswetenschappen en Architectuur
Vakgroep Informatietechnologie
Technologiepark-Zwijnaarde 126 iGent, 9052 Gent, België
Tel.: +32 (0)9264 3316

Proefschrift tot het behalen van de graad van
Doctor in de ingenieurswetenschappen:
fotonica
Academiejaar 2018-2019

Acknowledgement

Wow, this has been a journey. It took longer than originally planned but sometimes that is just the way things must be.

First I would like to thank Dries who took a chance hiring me and then gave me the freedom to do this my way. Even though it can't have been without its frustrations. I also want to thank all the other professors of the group: Roel, Geert, Peter, Wim, Gunther, Nicolas, Bart and Stephane. You have always taken the time to answer my countless questions over the years.

We are a large group and so many people have come and gone over the years. Many of you have been not only colleagues but also friends. From great lunch discussions and coffee breaks to ping-pong matches and movie nights it has been a good group to work in.

Thanks to the big office in Technicum, it was great but you are too many to mention by name.

A large thank you go to my office: Jing, Ali, Chupao, Clemens, Alex, Leila, Guilherme and Tommaso. Especially Mattias who helped me translate the summary to dutch and for answering endless questions on what makes this country special.

Thanks to the optomechanics group: Raphael, Paul, Alex, Khannan and Irfan for enduring endless lines of questions often chasing the tiniest spark of an idea.

Alfonso and Dorian you two really know how to party. A special thanks to Andrew and Paul, you have always been there when I have needed to vent my frustrations over a beer.

Thanks to Liesbeth, Steven and Muneeb for all the help you have given in the cleanroom. Your hard work is what has made much of my efforts see the light of day.

Thanks to Jeroen, Jelle, Jasper and especially Michael for a Herculean effort in bringing some measure of order to the measurement room. I don't know how you manage to stay sane.

Thanks to Ilse Van Royen, Ilse Meersman and Kristien De Meulder for always going the extra mile helping me with paperwork and many of perhaps the dumbest questions I have needed to ask anyone here in Belgium.

Outside the group I especially want to thank Thomas, Marie and Philipp. You have been a great support and I have enjoyed every moment I have spent with you.

Thanks also to my family back home in Sweden. Ni betyder något oerhört mycket för mig och det är med ert stöd det här har varit möjligt. Jag älskar er.

It has truly been a privilege,

Gent, April 2019
Jesper Håkansson

Table of Contents

Acknowledgement	i
Nederlandse samenvatting	xvii
Referenties	xxi
English summary	xxiii
References	xxvii
1 Introduction	1
1.1 Mass sensing	1
1.2 State of the art mass sensing	2
1.3 Silicon photonics	3
1.4 The design of our mass sensor	4
1.5 Brillouin scattering	5
1.6 Algorithmic design and optimization of Brillouin active waveguides	6
1.7 Outline	8
1.8 Publications	9
1.8.1 Publications in international journals	9
1.8.2 Publications in international conferences	9
References	10
2 Optomechanical Resonators	15
2.1 Introduction	15
2.2 Mechanical resonators	15
2.2.1 Resonance frequency	16
2.2.2 Lumped parameters models	17
2.2.3 Analytical solutions to cantilevers	18
2.2.4 Perturbing the mechanical resonator	21
2.3 Material properties	22
2.3.1 Optical	22
2.3.2 Crystal Orientations	23
2.3.3 Mechanical	24
2.3.4 Photoelastic properties	27
2.4 Mechanical losses	27
2.4.1 Air damping	28

2.4.2	Clamping losses	29
2.4.3	Surface oxide	31
2.4.4	Thermomechanical losses	33
2.4.5	Akhiezer losses	34
2.5	Displacement Sensing	34
2.5.1	Capacitive detection	34
2.5.2	Piezoresistive Detection	35
2.5.3	External interferometric detection	35
2.5.4	Integrated optical phase detection	35
2.5.5	Integrated optical intensity detection	36
2.6	Actuation	36
2.6.1	Electrostatic	36
2.6.2	Thermoelastic	36
2.6.3	Piezoelectric	37
2.6.4	Optical forces	37
2.6.4.1	Electrostriction	38
2.6.4.2	Radiation pressure	39
2.7	Mechanical non-linearities	40
2.7.1	Solving the critical amplitude for a nonlinear drive and resonator	41
2.7.2	Other optical non-linearities	45
2.8	Coupled resonators	47
2.8.1	Individual resonators in a coupled system	48
2.9	Understanding frequency noise	50
2.9.1	Sources of the frequency noise	51
	References	53
3	Strong optical forces in slot waveguide mass sensor	57
3.1	Introduction	57
3.2	Mass responsivity	57
3.2.1	Sensitivity to sample distribution	58
3.2.2	Mass sensitivity	59
3.3	Designing the mass sensor	60
3.3.1	Measuring the coupling between the cantilevers	61
3.3.2	Dissipatively coupled resonators as mass sensors	62
3.3.3	Slot waveguides for optomechanics	65
3.3.3.1	Optomechanical forces in slot waveguides	65
3.3.4	Designing the slot	68
3.3.5	Optical stiffness and damping	68
3.3.6	Displacement sensitivity	69
3.3.7	Thermal calibration	70
3.4	Optical Circuit	72
3.5	Fabrication	74
3.5.1	Optical proximity correction	74
3.5.2	Under-etching	75

3.5.3	Stiction	77
3.6	Optically driven measurements	79
3.7	Measured noise	80
3.8	Conclusion	81
	References	83
4	Designing waveguides for stimulated Brillouin scattering with genetic algorithms	85
4.1	Introduction	85
4.1.1	The history of genetic algorithms	85
4.1.2	The language of genetic algorithms	86
4.2	The algorithm	87
4.2.1	Parallel computing	88
4.2.2	Choosing the right genotype space	88
4.2.2.1	Binary representation	88
4.2.2.2	Integer representation	90
4.2.2.3	Real-valued representation	90
4.2.2.4	Permutation representation	91
4.2.2.5	Tree representation	92
4.2.3	Parent selection	93
4.2.3.1	Fitness proportional selection	93
4.2.3.2	Ranking selection	93
4.2.3.3	Uniform parent selection	93
4.2.4	Survivor Selection	94
4.2.4.1	$(\mu + \lambda)$ selection	94
4.2.4.2	(μ, λ) selection	94
4.2.4.3	Generational selection	94
4.2.5	Parameterizing a waveguide	94
4.2.6	Genetic operators for waveguides	96
4.2.7	Choosing an initial population	96
4.2.8	Selecting the parameters	98
4.2.9	Functionalizing via context	98
4.2.10	The importance of diversity	99
4.3	Multiple objective optimization	99
4.3.1	Multiple objective optimization	99
4.3.2	Constraint handling	100
	References	102
5	Brillouin Scattering	103
5.1	Introduction	103
5.2	Stimulated Brillouin scattering	103
5.3	Simulating the coupling	106
5.4	The individual waveguides generated by the algorithm	107
5.4.1	Introduction	107
5.4.2	Unique waveguides	108

5.5	Local Optimization	111
5.5.1	Optimising the matrix representation of the waveguide . .	111
5.5.2	Reparametrizing the waveguide	112
5.6	The fitness landscape	113
5.7	Conclusion	116
	References	118
6	Conclusions and perspectives	119
6.1	Conclusions	119
6.2	Future Work	120
6.2.1	A full integration of the mass sensor	120
6.2.2	A more robust mass sensor	120
6.2.3	Expanding the genetic algorithm	121
	References	121
	123

List of Figures

1	a) Illustratie van de werking van een massasensor. b) Het verplaatsingsgevoeligheidsschema c) hoe de transmissie afhangt van de verplaatsing	xvii
2	a) Een SEM afbeelding van de massasensor. B) Een spectrum van de sensorrespons wanneer een optische kracht gemoduleerd is. . .	xviii
3	a) De golfgeleider met de hoogste gestimuleerde Brillouinverstrooiingsversterking. Oranje komt overeen met silicium en zwart met siliciumoxide. Een cel is 50 nm x 50 nm. b) and c) represent the mechanical and optical modes in this waveguide.	xx
4	a) Alle optomechanische modeparen van alle golfgeleiders die geëvalueerd zijn door het genetisch algoritme. B) Een onafhankelijk geoptimaliseerde golfgeleider. De zwarte lijn in a) is een projectie van golfgeleider b) voor het hele frequentiebereik.	xx
5	a) Illustration of the operation of a mass sensor. b) The displacement sensitivity scheme and c) how the transmission depends on the displacement.	xxiii
6	a) A SEM image of the mass sensor. b) A spectrum of the sensor response when the optical force is modulated.	xxiv
7	a) The waveguide with the highest stimulated Brillouin scattering gain. Orange indicating silicon and black silica. The rectangles each representing a 50 nm by 50 nm square. b) The mechanical mode and c) the optical mode.	xxv
8	a) All the optomechanical mode pairs of all the waveguides evaluated by the genetic algorithm. b) A separately optimized slot waveguide. The black line in a) is a projection of waveguide b) for the whole frequency span.	xxvi
1.1	a) A chip with integrated circuits at a measurement stage and two fibers for coupling light in and out of the circuit. b) The CAD schematic of such a circuit.	4

1.2	a) An illustration of the mass sensor and the coupling to and from it. 2) By guiding light in the slot between two cantilevers it generates a strong force between them driving a vibration. How well light couples to the other slot is dependent on how the first slot is deformed by the vibration.	5
2.1	Drawing of a cantilever.	18
2.2	Resonance frequency measurements of a series of cantilevers of different length compared to the inverse square dependency on length expected from classic beam theory.	19
2.3	The mode shapes of the first few orders of resonances of a cantilever. The equations are given in equation 2.15.	20
2.4	a) In-plane drawing of a (1,0,0) wafer with arrows in the [1,0,0] and [1,1,0] direction. b) SOI material stack provided by the IMEC standard passives MPW. The top silicon layer is intended to guide the light and the buried oxide keeps that guiding layer far enough from the silicon substrate underneath.	22
2.5	The measured mechanical quality factor of the mass sensing cantilever pair plotted against air pressure.	30
2.6	Mechanical mode leaking from the resonator into the substrate and then being absorbed in the outer circle to simulate clamping losses. Shown with \log_{10} scale and normalized to the maximum displacement.	32
2.7	Measurements before removing the oxide give a Q-factor of 4000 which increases to 6300 after it is removed. The Q-factor then decreases to 5100 after an hour of air exposure.	33
2.8	a) Optical and (b) mechanical mode of a wire waveguide. The blue color signify the volumetric strain.	40
2.9	(a) is the amplitude response and (b) is the phase response of the susceptibility function of a nonlinear resonator for several different drive forces. The legend is valid for both figures. The orange line reaches the critical amplitude. The nonlinear parameters are taken from simulations of the mass sensor.	42
2.10	The (a) amplitude and (b) phase of the susceptibility function for resonators modeled with different orders of nonlinear constants. The P_{DC} terms includes the nonlinearities associated with continuous optical power in the waveguide. The P_{AC} terms includes the nonlinearities associated with the modulated drive force. The legend is valid for both figures.	44
2.11	The dashed orange line shows the critical amplitude and force acting on the slot waveguide as a function of cantilever width. The critical amplitude is calculated assuming a 1 mW CW optical power in the waveguide and a 100 nm slot width. For most cantilever widths the slot is the fundamental limit to the amplitude.	45

2.12	Diagram of coupled resonators. The variables signify: g and k are springs, c viscous damping and m the mass. a denotes displacement of the mass along the direction of the arrow.	46
3.1	The figure is showing the effective mass contribution, $\phi_n^2(x)$, for different mode order, n , against each other. The orange dots mark 10% percentiles of the cantilever length. The radial grey lines act as a visual guide for the fractions $\phi_n^2(x)/\phi_m^2(x)$	59
3.2	a) Normalized mass responsivity of a superposition of the first three orders of modes. The superposition is optimized for the top 20% of the cantilever (the blue region). b) Enlarged view of the optimized area.	60
3.3	Mechanical supermodes of the cantilever pair. The colors signify the volumetric strain.	61
3.4	a) Schematic for designing the coupling between the cantilevers. b) The resulting frequency splitting from tuning δ_{stem}	62
3.5	Mode splitting for the mass sensor cantilever pair described in the next chapter. The cantilevers are of equal and unequal length, unequal meaning one of them is 100 nm shorter than the other. The 2 and 3 μm equal length measurements are not available since the signal is too low.	62
3.6	The RF spectrum of two mass sensors. In one of the cantilever pair one of the cantilevers has been shortened by 100 nm. The difference in signal is largely due to a difference in input optical power.	63
3.7	a) Simulations of the phase difference between the two prongs. b) Mass sensitivity as a function of integration time. The two prongs double in effective mass as the coupling mediates the synchronisation ($(\Gamma_{12})^{-1} = 10^{-4}\text{s}$). The improvement in noise level is counteracted by the increase in mass.	64
3.8	Drawing of the mass sensor cantilevers with the purpose of naming the dimensions of each component. The blue line and arrows shows the first order mechanical mode of the cantilever.	65
3.9	Optical mode in slot waveguide (the electric field is displayed in red). The black arrows radiating from the interface show the direction and relative magnitude of the local force contribution in accordance with the perturbation theory used to calculate the radiation pressure.	66
3.10	Effective refractive index as it depends on the width of the silicon slab. As the slot waveguide grows wider the slot mode (TE_1) transitions into a symmetric supermode like the one in a directional coupler. Around that point another slot mode (TE_3) can be guided.	66
3.11	(a) The refractive index and (b) optical forces in a slot waveguide.	67
3.12	The force as a function of the width of the silicon slabs in the slot waveguide.	68

3.13	The forces in an asymmetric slot waveguide in silicon for the waveguide dimensions given in the plot.	69
3.14	The displacement sensitivity of the transmitting slot mapped as a function of of the two slot widths. The red cross marks the point we are operating at.	70
3.15	Setup and measurement of the thermal vibrations of the cantilever. By comparing with the expected thermal amplitude marked in the figure it is possible to verify the displacement sensitivity.	71
3.16	Shows the displacement sensitivity over a spectrum of wavelengths calculated from the amplitude of the thermal spectrum. The displacement sensitivity relative to the power leaving the sensor.	73
3.17	MMI coupling light from wire waveguide to slot mass sensor.	73
3.18	A SEM picture of the mass sensor. MMI has been shaded red and the cantilevers have been shaded purple.	74
3.19	The result of (a) $\delta_{opc} = 0$ nm, (b) 30 nm, (c) 60 nm designed cut into the base of the cantilevers (d) drawing of the mask design. As a result the radius of the corner is reduced from 91 nm to 76 nm. The largest cut is beginning to dig into the width of the cantilever.	76
3.20	Diagram of underetching a waveguide. The grey contours show the air-oxide interface as the etching progresses. The structure on the right would be underetched without the photoresist delaying the etch.	77
3.21	a) Outcome of stiction test on a group of mass sensors. Underetched with HF, washed with water then dried. An elastocapillary number above 1 should result in collapse. Only one cantilever pair that should not have collapsed did. b) SEM image of collapsed mass sensor where the tips are stuck together.	78
3.22	a) A measurement of the amplitude response of an optically driven cantilever. The cantilever is driven and the vibration detected at the same frequency. b) The setup of the optically driven measurement.	79
3.23	The amplitude response to an optical drive of the (a) second order and (b) third order mode. The third order mode only shows one peak because the low signal from symmetric mode disappears under to noise.	80
3.24	(a) Phase noise and (b) Frequency noise of a $6\mu m$ cantilever. The calculated thermomechanical noise is included in the figure as a reference. Also marked is the mechanical decay rate ω/Q_{mech} marking the rate with which noise decays.	82
4.1	Optimized satellite boom [2].	86
4.2	Flowchart of a standard genetic algorithm.	87
4.3	Example binary genome	89
4.4	Example binary mutation	89
4.5	Example binary crossover	89
4.6	Example integer genomes	90

4.7	Example real-valued genome	90
4.8	Example permutation genome	91
4.9	Three examples of permutation mutations	92
4.10	Example tree genome.	93
4.11	A sample rasterized waveguide. The different colors denote different materials.	96
4.12	Our mutation operators.	97
4.13	Our crossover operator.	97
4.14	Example illustration of the pareto optimal solutions. The red line mark the options where you can not get more without performance.	100
5.1	Illustrated spectrum of Brillouin scattering process. When the beat note between the two optical waves excite the mechanical resonance at Ω	104
5.2	Example dispersion diagram of an optical waveguide with a scattering event marked by the orange arrow.	105
5.3	The modes index and ranked according to (a) lowest mechanical frequency and (b) highest effective refractive index of the waveguide. (c) the ranks of the highest gain modes as per their respective frequency.	108
5.4	The gain and frequency of all simulated mode pairs. The modes and waveguides selected in table 5.1 are indicated by the dots labeled a-i.	109
5.5	Two different integers found next to each other indicates a boundary. That pattern is then replaced.	112
5.6	Optimized slot when the waveguide is re-expressed as a polynomial and the mechanical frequency independent of the optics.	113
5.7	The gain, frequency and group index of all simulated mode pairs. The black line indicates the frequency normalised gain of the optimised slot waveguide shown in the inset. The mechanical quality factor is set to 1000.	114
5.8	a) Gain as a function of group index and (b) effective mass. The color signify mechanical frequency. The effective mass is given relative to the maximum displacement.	115
5.9	The separate power-normalised force components: a) relative to each other as well as b) electrostriction and c) radiation pressure separately. The colour signifies the highest gain found at the indicated place in the graph.	116

List of Tables

2.1	The values of are assuming the crystal orientation $\langle 1, 0, 0 \rangle$	25
2.2	The values are assuming the crystal orientation $\langle 1, 0, 0 \rangle$ and are not necessarily at $1.55\mu m$ optical wavelength.	27
2.3	Critical amplitude of cantilevers and beams clamped on both sides. L is the length and W the width of the resonator.	41
3.1	Recepie for under-etching mass sensor	77
5.1	A selection of competitive, distinct and noteworthy waveguides. They are indicated in figure 5.4 with red points. Shown, starting from the left, in each row are: material composition and shape, mechanical mode, optical mode and simulated performance. The shape is shown on top of a 50 by 50 nm grid. ES and RP are the electrostrictive and radiation pressure force. The forces are in all the given examples interfering constructively.	111

List of Acronyms

List of Acronyms

AC	Alternating Current
CW	Continuous Wave
CD	Critical Dimension
CMOS	Complementary metaloxidesemiconductor
CPD	Critical Point Dryer
DC	Direct Current
EDFA	Erbium Doped Fiber Amplifier
ESA	Electrical Spectrum Analyzer
FEM	Finite Element Method
GA	Genetic Algorithm
MMI	Multi-Mode Interferometer
MEMS	Microelectromechanical systems
NEMS	Nanoelectromechanical systems
PML	Perfectly Matched Layer
PLL	Phase-Locked Loop
SNR	Signal to Noise Ratio
SBS	Stimulated Brillouin Scattering
TPA	Two-Photon Absorption
VCO	Voltage Controlled Oscillator

Nederlandse samenvatting –Summary in Dutch–

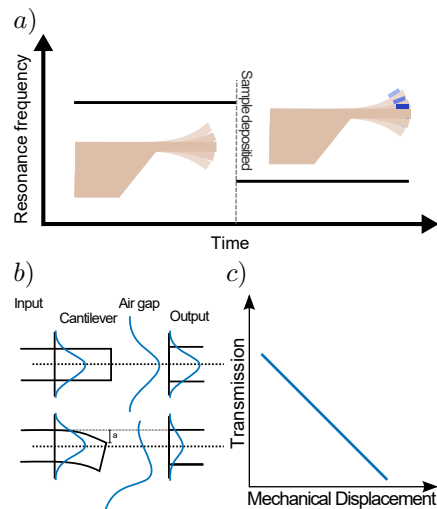
Introductie

In de laatste dagen van 1959 werd er een legendarische lezing gegeven door Richard Feynman met de titel 'There's Plenty of Room at the Bottom: An invitation to Enter a New Field of Physics'. Daarin beschrijft Feynman een toen nieuw en nog onontwikkeld wetenschappelijk veld van manipulatie en controle op kleine schaal. De lezing bleef lange tijd onopgemerkt, maar begin jaren tachtig werd ze door voorstanders van nanotechnologie aangehaald om de wetenschappelijke geloofwaardigheid van hun werk te ondersteunen.

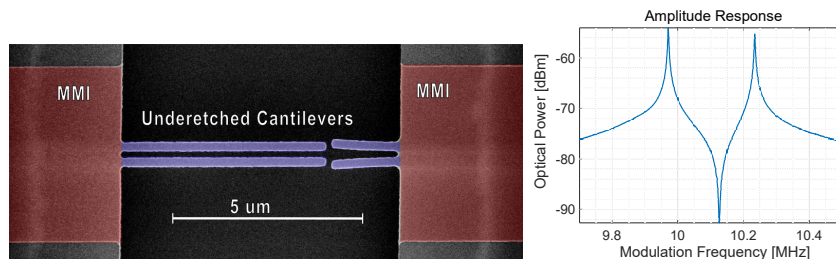
De schalingswetten zijn van die aard dat wanneer iets tot de helft wordt verkleind, het oppervlak wordt verkleind tot een kwart en het volume tot een achtste van wat ze waren. Dit betekent dat kleine mechanische structuren stijver zijn en dat hun massa lager

is, waardoor de resonantiefrequenties aanzienlijk toenemen. Dit is bijvoorbeeld van belang bij het ontwerpen van sensoren, omdat ze gevoeliger worden voor veranderingen in massa en omdat er minder thermische ruis is bij hogere frequenties. Daarom is het onderzoek in veel sensortoepassingen een race om de kleinste sensor te maken die nog steeds bruikbaar is en kan worden uitgelezen.

Kleine massa's zijn moeilijk te meten met behulp van de zwaartekracht, die te zwak is daarvoor. In plaats daarvan wordt hun inertie (traagheid) gemeten. De tweede wet van Newton zegt dat kracht gelijk is aan massa maal versnelling. Dus als een kracht, inwerkend op een monster, bekend is en de verandering in de snelheid van het monster kan worden gemeten, dan kan de massa van dat monster



Figuur 1: a) Illustratie van de werking van een massasensor. b) Het verplaatsingsgevoeligheidsschema c) hoe de transmissie afhangt van de verplaatsing



Figuur 2: a) Een SEM afbeelding van de massasensor. b) Een spectrum van de sensorrespons wanneer een optische kracht gemoduleerd is.

worden berekend. Een van de handigste manieren om dit te bereiken is om te meten hoe de resonantiefrequentie van een cantilever verandert als er een testmassa wordt opgeplaatst.

De reductie in dimensies van de cantilever maakt het echter alsmaar problematischer om ook een aandrijving en een detector met het systeem te integreren. Daarom is erg handig dat een goed micro-elektromechanisch systeem (MEMS) materiaal, zoals silicium, ook optisch transparant is. Als onze cantilever ook een optische golfgeleider is, dan kunnen we de richting van het licht meten dat de cantilever/golfgeleider verlaat en hoe die verandert wanneer de cantilever trilt.

Zoals onder andere de Nobelprijswinnaar Arthur Askin heeft aangetoond, worden materialen met een hoge brekingsindex aangetrokken tot het centrum van een gefocuste laserstraal. Dus wanneer het licht wordt gekoppeld aan een golfgeleider begint die andere golfgeleiders die zeer dichtbij zijn aan te trekken. Dit principe kan worden gebruikt om de eerder beschreven massasensor aan te drijven. Het gebruik van optische krachten om mechanische systemen aan te drijven is interessant omdat veel van de voordelen van het werken met licht, zoals hoge modulatiesnelheden en lage propagatieverliezen, behouden kunnen worden.

Optomechanische sensoren bestaan al een tijdje in optische vezels. Een sterke optische golf vervormt de vezel zodat deze begint te trillen en het licht wordt gereflecteerd door die trilling. Het proces wordt gestimuleerde Brillouinverstrooiing genoemd. De frequentie van die trillingen is materiaalafhankelijk en wordt direct beïnvloed door spanning en temperatuur in de vezel. Wanneer het licht wordt gefocust in de veel kleinere golfgeleiders die in geventreerde fotonica worden gebruikt, wordt de verstrooiingsefficiëntie veel hoger en is er daarom een focus op het overbrengen van de Brillouinverstrooiingsapparaten die in vezels bestaan naar een geventreerd platform.

Dit werk is verdeeld in twee delen: In het eerste deel hebben we een volledig optische actuatie en detectie van een massa traagheids sensor bestudeerd [1]. In het tweede deel hebben we genetische algoritmes gebruikt om optische golfgeleiders te vinden die de gestimuleerde Brillouinverstrooiing (SBS) versterking optimaliseren [2]. De SBS versterkingscoëfficiënt is daarbij een metriek voor de verstrooiingsefficiëntie van de golfgeleider.

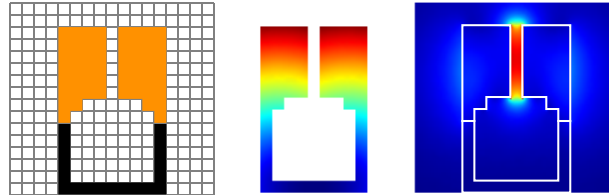
Resultaat

De resolutie van een massasensor is wordt bepaald door hoe sterk de ruis kan onderdrukt worden t.o.v. de amplitude van de coherente trillingen. In de literatuur is aangetoond dat optische slotgolfsgeleiders uitzonderlijk sterke optomechanische krachten genereren en deze kunnen dan ook gebruikt worden voor de aandrijving van een massa sensor. Het gebruik van een optisch aandrijving is interessant omdat dezelfde on-chip infrastructuur ook kan worden gebruikt voor de detectie van het signaal. In de door ons voorgestelde sensor wordt het licht gekoppeld in de slotgolfsgeleider met een multimode interferometer die een robuust anker biedt voor de mechanische resonator. Bovendien kan deze samen met decantilever in n enkele stap gedefinieerd worden, wat de herhaalbaarheid van de sensormetingen verbetert. Dit maakt het mogelijk om massasensoren met een zeer kleine on-chip footprint ($< 2000 \text{ um}^2$) te realiseren.

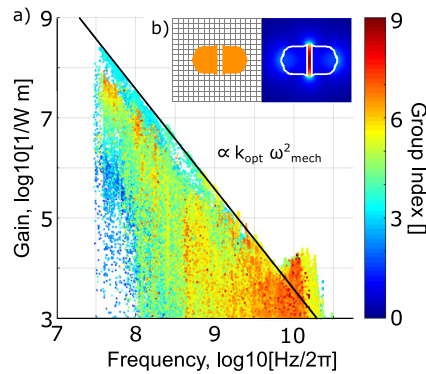
De performantie van een massasensor wordt voor een groot deel beoordeeld door twee karakteristieken: de massaresponsiviteit is de frequentieverschuiving per gemeten testmassa en de massagevoeligheid is het kleinste massaverschil dat kan worden onderscheden. Een van de in het kader van dit werk gefabriceerde sensoren heeft een massa-reactievermogen van 146 ZHz/kg en een massagevoeligheid van 500 kDa. Deze massa-gevoeligheid is in lijn met die van gepubliceerde sensoren [3, 4] en eerder voorgestelde volledig-fotonische massasensoren [5, 6], maar onze sensor heeft een beduidend kleiner vermogen om de vibratie aan te drijven. Samenvattend hebben we een massasensor ontworpen, gefabriceerd en gemeten die door gebruik te maken van een nieuwe actuatiemethode een competitieve prestatie levert. De kleine afmetingen, de keuze van het materiaalplatform en de fabricagemethoden maken een goedkope sensor compatibel met massaproductie mogelijk.

Om een golfsgeleider te ontwerpen met een sterke SBS versterking, is een compromis nodig tussen het bereiken van lage optische verliezen, een goede mechanische geleiding en een sterke koppeling tussen beide effecten, allemaal in dezelfde fysieke structuur. SBS in geventreerde fotonica is nog steeds een relatief nieuw onderwerp, en is nog maar enkele jaren geleden voor het eerst gedemonstreerd. De focus van de onderzoeksgemeenschap lag tot nu toe vooral op het vinden van het juiste materiaal om in te werken en minder op de vorm van de golfsgeleider.

In dit doctoraatsonderzoek hebben we gebruik gemaakt van genetische algoritmen om de golfsgeleiders met de hoogste SBS versterking over een reeks mechanische frequenties te vinden. De hoogste versterking onder de gegenereerde golfsgeleiders is $2,5 \times 10^8 \frac{1}{Wm}$, ruim boven wat bereikt werd in eerder aangetoonde golfsgeleiders. De voorgestelde golfsgeleider is gellustreerd in figuur 3. De geaccumuleerde resultaten van alle 24000 gesimuleerde golfsgeleiders zijn weergegeven in figuur 4. Met deze resultaten kunnen we ook iets zeggen over de meer algemene trends over het mechanische frequentiebereik. Als voorbeeld: de omgekeerde kwadratische afhankelijkheid van de mechanische frequentie is duidelijk



Figuur 3: a) De golfgeleider met de hoogste gestimuleerde Brillouinverstrooiingsversterking. Oranje komt overeen met silicium en zwart met siliciumoxide. Een cel is 50 nm x 50 nm. b) and c) represent the mechanical and optical modes in this waveguide.



Figuur 4: a) Alle optomechanische modeparen van alle golfgeleiders die gevalueerd zijn door het genetisch algoritme. B) Een onafhankelijk geoptimaliseerde golfgeleider. De zwarte lijn in a) is een projectie van golfgeleider b) voor het hele frequentiebereik.

zichtbaar, maar dat patroon wordt verstoord rond 10 GHz. In dat gebied verandert de koppelingsmechanica en begint de vervorming een significante invloed te hebben op de optische eigenschappen van de golfgeleider, waar deze voordien vaak genegeerd kon worden. Met deze resultaten toonden we aan dat genetische algoritmen een geschikte methode zijn voor multi-objectief optimalisatie van niet-lineaire golfgeleiders. Dit is interessant bij het ontwerpen van een SBS-golfgeleider voor sensortoepassingen of voor gebruik in een specifiek mechanisch frequentiebereik.

Referenties

- [1] Jesper Håkansson, Bart Kuyken, and Dries Van Thourhout. *Strong forces in optomechanically actuated resonant mass sensor*. Optics express, 25(25):30939–30945, 2017.
- [2] Jesper Håkansson and Dries Van Thourhout. *Generating novel waveguides for stimulated Brillouin scattering with genetic algorithms*. APL Photonics, 4(1):010803, 2019.
- [3] E Forsen, G Abadal, Sara Ghatnekar-Nilsson, J Teva, J Verd, R Sandberg, W Svendsen, Francesc Perez-Murano, J Esteve, E Figueras, et al. *Ultrasensitive mass sensor fully integrated with complementary metal-oxide-semiconductor circuitry*. Applied Physics Letters, 87(4):043507, 2005.
- [4] Gabriel Vidal-Álvarez, Jordi Agustí, Francesc Torres, Gabriel Abadal, Núria Barniol, Jordi Llobet, Marc Sansa, Marta Fernández-Regúlez, Francesc Pérez-Murano, Álvaro San Paulo, et al. *Top-down silicon microcantilever with coupled bottom-up silicon nanowire for enhanced mass resolution*. Nanotechnology, 26(14):145502, 2015.
- [5] Mo Li, WHP Pernice, and HX Tang. *Broadband all-photonic transduction of nanocantilevers*. Nature nanotechnology, 4(6):377, 2009.
- [6] Dmitry Yu Fedyanin and Yury V Stebunov. *All-nanophotonic NEMS biosensor on a chip*. Scientific reports, 5:10968, 2015.

English summary

Introduction

There is a legendary lecture given by Richard Feynman in the last days of 1959 called 'There's Plenty of Room at the Bottom: An Invitation to Enter a New Field of Physics'. Therein Feynman describes a then new and mostly undeveloped scientific field of manipulating and controlling things on a small scale. It mainly went unnoticed for a long while but beginning in the 1980s nanotechnology advocates cited it to establish the scientific credibility of their work.

The scaling laws are such that when something is shrunk down to half its size the surface is shrunk to a quarter and the volume an eighth of what it was. This means that small mechanical structures are stiffer and that their mass is lower so as a result the resonance frequencies increase substantially. This is significant when designing sensors e.g. as they become more sensitive to changes in mass when the sensor mass is smaller and because there is less thermal noise at higher frequencies. Therefore the research in many sensing applications is a race to make the smallest sensor where the relevant metric is still possible to measure.

Small masses are difficult to measure with the help of the gravitational force; it is too weak. It is instead measured via the inertia. Newton's second law says that force is mass times acceleration. So if a force acting upon a sample is known and the change in the speed of the sample can be measured, then the mass of that sample can be calculated. One of the more convenient ways of achieving this is to measure how the resonance frequency of a cantilever changes when a sample is attached to it.

The small size of the cantilever becomes a problem however as it becomes difficult to integrate a drive and a detector. It is very convenient than that a good

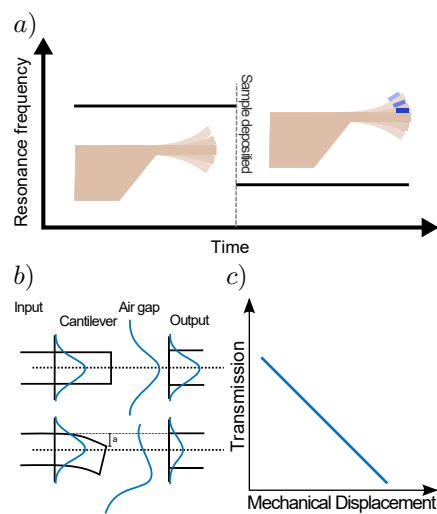


Figure 5: a) Illustration of the operation of a mass sensor. b) The displacement sensitivity scheme and c) how the transmission depends on the displacement.

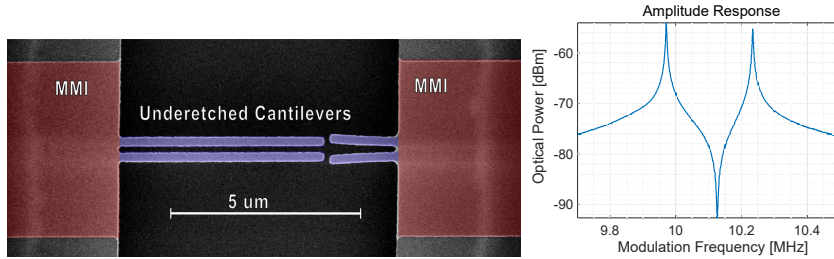


Figure 6: a) A SEM image of the mass sensor. b) A spectrum of the sensor response when the optical force is modulated.

micro-electro-mechanical systems (MEMS) material like silicon is transparent. If our cantilever is also an optical waveguide as well then we can measure the direction of the light leaving the cantilever/waveguide and how it changes when it vibrates.

As was demonstrated by among other last years Nobel prize laureate Arthur Askin, high refractive index materials are attracted to the centre of a focused laser beam. So when light is coupled to a waveguide it starts to pull in other waveguides that are very close by. This principle is used to drive the mass sensor described earlier. Using optical forces to drive mechanical systems is interesting because many of the advantages from working with light are kept like high modulation speeds and low propagation losses.

Optomechanical sensors have existed for a while already in optical fibres. A strong optical wave deforms the fibre so it starts to vibrate and then light is reflected by that vibration. The process is called stimulated Brillouin scattering. The frequency of those vibrations are material dependent and are directly affected by stress and temperature in the fibre. When the light is focused into the much smaller waveguides that are used in integrated photonics the scattering efficiency becomes much higher and there is, therefore, a focus on translating the Brillouin scattering devices that exist in fibres into an integrated platform.

Results

This work is split into two sections. In the first part, we have studied using an all-optical actuation and detection of an inertia mass sensor [1]. In the second part, we have used genetic algorithms to find the optical waveguide design with the optimal stimulated Brillouin scattering (SBS) gain [2]. The SBS gain coefficient is a metric for the scattering efficiency of the waveguide.

The resolution of an inertia mass sensor is dependent on the amplitude of the coherent vibrations over the frequency noise. Optical slot waveguides have been shown to generate exceptionally strong optomechanical forces and can, therefore, drive the waveguide to high vibrational amplitudes. Using an optical drive is interesting because it can use the same on-chip infrastructure as the detection scheme

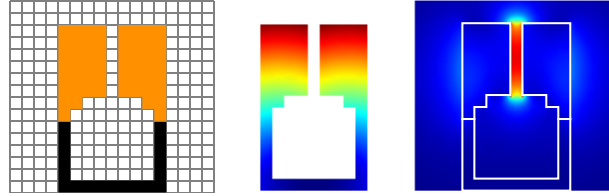


Figure 7: a) The waveguide with the highest stimulated Brillouin scattering gain. Orange indicating silicon and black silica. The rectangles each representing a 50 nm by 50 nm square. b) The mechanical mode and c) the optical mode.

and optical displacement detection has demonstrated sensitivity well below the thermal noise.

In our sensor we couple the light into a slot waveguide cantilever with a multi-mode interferometer. This way we provide a robust anchor for the optical waveguide so that it can be a good mechanical resonator and define the length of the waveguide in a single processing step which improves repeatability for the sensor metrics. We then collect the light leaving the slot with another slot waveguide fixed to another MMI after which the light is routed to a photo-detector. Altogether this allows for mass sensors with a very small on-chip footprint ($< 2000 \text{ um}^2$).

A mass sensor is qualified in large part by two metrics: the mass responsivity is the frequency shift per sample mass measured and the mass sensitivity is the smallest mass difference that can be resolved. One of the fabricated sensors which is operating at 10 MHz has a mass responsivity of 146 ZHz/kg and a mass sensitivity of 500 kDa. This mass sensitivity is in line with published sensors [3, 4] and previously suggested all-photonically transduced mass sensors [5, 6] while using a significantly smaller power to drive the vibration. In conclusion, we have designed, fabricated and measured a mass sensor that by using a novel actuation method achieves a competitive performance. The small sensor footprint, the choice of material platform and fabrication methods allows for cheap mass production.

To design a waveguide for a strong SBS gain, one needs to compromise between having a good optical waveguide, a good mechanical waveguide, and a strong coupling between the two, all in the same physical structure. SBS in integrated photonics is still a relatively new subject having been demonstrated only a few years ago. The focus of the research community has primarily been on finding the right material to work in and less on the shape of the waveguide.

In this PhD research we have used genetic algorithms to find the waveguides with the highest SBS gain over a range of mechanical frequencies. The highest gain among the generated waveguides is $2.5 \times 10^8 \frac{1}{Wm}$, well above any previously demonstrated SBS WG. The waveguide is illustrated in figure 7. The accumulated results of all 24000 simulated waveguides are shown in figure 8. Based on our results we can also say something about the more general trends across the mechanical frequency span. As an example, the inverse square dependence on the

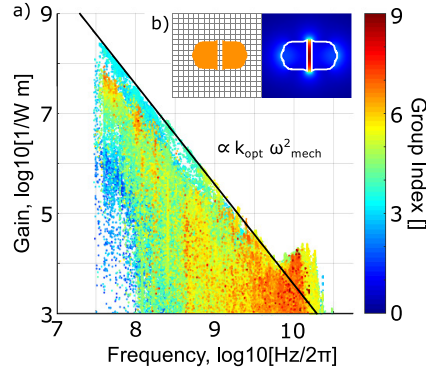


Figure 8: a) All the optomechanical mode pairs of all the waveguides evaluated by the genetic algorithm. b) A separately optimized slot waveguide. The black line in a) is a projection of waveguide b) for the whole frequency span.

mechanical frequency is clear to see but that pattern is broken around 10 GHz. In that region, the coupling mechanics changes and the strain starts to have a significant influence on the optical properties of the waveguide where earlier it could often be ignored. We show that genetic algorithms are a suitable method for multi-objective optimisation of nonlinear waveguides. This is interesting when designing an SBS waveguide for sensing or for use in a specific mechanical frequency span.

References

- [1] Jesper Håkansson, Bart Kuyken, and Dries Van Thourhout. *Strong forces in optomechanically actuated resonant mass sensor*. *Optics express*, 25(25):30939–30945, 2017.
- [2] Jesper Håkansson and Dries Van Thourhout. *Generating novel waveguides for stimulated Brillouin scattering with genetic algorithms*. *APL Photonics*, 4(1):010803, 2019.
- [3] E Forsen, G Abadal, Sara Ghatnekar-Nilsson, J Teva, J Verd, R Sandberg, W Svendsen, Francesc Perez-Murano, J Esteve, E Figueras, et al. *Ultrasensitive mass sensor fully integrated with complementary metal-oxide-semiconductor circuitry*. *Applied Physics Letters*, 87(4):043507, 2005.
- [4] Gabriel Vidal-Álvarez, Jordi Agustí, Francesc Torres, Gabriel Abadal, Núria Barniol, Jordi Llobet, Marc Sansa, Marta Fernández-Regúlez, Francesc Pérez-Murano, Álvaro San Paulo, et al. *Top-down silicon microcantilever with coupled bottom-up silicon nanowire for enhanced mass resolution*. *Nanotechnology*, 26(14):145502, 2015.
- [5] Mo Li, WHP Pernice, and HX Tang. *Broadband all-photonic transduction of nanocantilevers*. *Nature nanotechnology*, 4(6):377, 2009.
- [6] Dmitry Yu Fedyanin and Yury V Stebunov. *All-nanophotonic NEMS biosensor on a chip*. *Scientific reports*, 5:10968, 2015.

1

Introduction

1.1 Mass sensing

There are several ways of measuring the mass of an object. Ancient inventions such as the balanced scale and more modern versions using springs are familiar to most of us and have been instrumental in the development of fundamental aspects of civilisation such as trade. For small masses, however, these methods encounter difficulties. Gravity is a weak force in these situations and to find a spring soft enough or to operate a series of ultra-small counterweights quickly becomes a problem. Instead, the mass is measured via the inertia of the sample. By measuring the acceleration while experiencing a known force the mass can be calculated using Newton's second law. One option is to use a mass spectrometer but it does not measure the mass, instead it measures the mass-to-charge ratio. It is not trivial to ionise the particle to a known charge so while it is an excellent way to find the isotropic components of a molecule it does not directly measure the mass. Another option is to use MEMS or NEMS resonators as they offer low spring constants and low masses so the added sample mass makes a significant change to the resonator parameters. Some examples are the quartz crystal microbalance and the MEMS cantilever.

MEMS cantilevers came into prominence in 1986 with the experimental demonstration of the atomic force microscope (AFM) [1]. The AFM is essentially a minute record player where a needle traces the surface of the sample and records its topology and hardness. The needlepoint sharpened to a radius of a few nanometers is attached to a cantilever which deflects as the tip makes contact with the sample.

Similar to when measuring mass the cantilever needs to have a low spring constant to increase sensitivity and a high resonance frequency as it shields the cantilever from external vibrations.

Cantilever-based sensors appeared as a research field in the 1990s with the discovery that with a metal coating on one side these AFM cantilevers were sensitive to temperature, humidity and a series of chemicals [2–4].

Today it is a well-established technology for label-free sensing and with the advances made in CMOS fabrication promises cheap, portable, sensitive and highly parallel analysis systems. Examples of sensor applications are covering such diverse fields as drug discovery [5], bacteria detection [6], material characterisation [7] and explosives detection [8].

There are several ways cantilevers can be used as a sensor [9]. We can measure: the deflection from surface forces generated by an analyte absorbed at the surface, the deflection from the intrinsic properties of the resonator changing or the shift in resonance frequency as its properties as a resonator change. The inertia mass sensor measures that frequency shift as a sample mass is added to the mass of the cantilever, as is illustrated in figure 5a in the summary.

One of the difficulties with using MEMS devices for mass sensing is the sample deposition. These devices are often fragile and sensitive. A solution is to integrate a microfluidic channel into the MEMS device, then the delivery can be made easier and faster. Many potential samples are initially in liquid form [10] and are damaged by drying so this delivery method is very promising.

The detection limit of an inertia mass sensor is directly dependent on the smallest frequency shift it can measure. Since frequency noise decreases with amplitude a good mass sensor has a strong force driving the vibration. With that comes that a good mass sensor also has excellent nonlinear properties so it can work with large vibrations without coupling other noise sources to the phase noise.

1.2 State of the art mass sensing

Ultimately the performance of a mass sensor is very dependent on the conditions under which it operates. The current state of the art for mass sensors combines the incredibly low mass of a carbon nanotube resonator with the low noise environment at 4 Kelvin [11]. This way it is possible to resolve mass shifts of 1.7 yg ($yg=10^{-24}$ g). The results are impressive but nanotubes have proven to be complicated to introduce in a mass-produced process and that degree of cooling is time-consuming and expensive.

It is possible to suppress the frequency noise in the sensor with the help of cavity optomechanical effects [12]. This method has been successful but does in turn require very high optical quality factors, the sensor in question has a quality factor above 10^6 . The quality of the surface required to reach such values makes

it difficult to combine it with many kinds of samples or the surface preparation needed to make the surface adhesion selective to the sample.

The best beam mass sensor known to the author that gives values for operation in room temperature is a silicon carbide beam with a magnetomotive actuation and detection [13] that is able to resolve masses as low as 2.5 ag ($\text{ag}=10^{-18}$ g) or 1.5 MDa. More about the driving and detection methods can be found in the sections about actuation and displacement sensing.

1.3 Silicon photonics

There are many ways of detecting vibrations but one of the most competitive is an integrated optical approach [14]. The method we are proposing in this work relies on that by choosing a transparent high refractive index material such as silicon for the cantilever it can guide light. By shining light through the cantilever it is possible to detect the vibrations as they bring the tip of the cantilever in and out of alignment with a second waveguide that collects the light and routes it to a photo-detector.

Since the read-out of the proposed mass sensor is done with light it is necessary to address the optical component of the device. Luckily the CMOS technology that allowed the fabrication of MEMS devices was also followed by the rapid development of integrated photonics.

One of the most significant technological revolutions of the last century was how electronics once as big as a whole room now can fit into a pocket. Computers are now millions of times faster than its large counterpart from previous decades, at a fraction of the cost.

The silicon photonics community hopes that the same development is possible in photonics and bring our optical tables down to a more portable size and in a mass producible design. By using the same technology and materials as are used in the CMOS facilities to fabricate integrated electronics we benefit from the extensive work already done to provide high-quality performance in a mass-producible format [15].

Many of the needed components have already been demonstrated such as tunable filters, spectrometers, grating couplers, high-speed detectors and modulators [16, 17]. It is not without setbacks, however. A major roadblock is the lack of integrated light sources in the silicon platform. In large part, this is due to the difficulty to integrate the gain medium. Another roadblock is the difficulty in replicating the performance of a device consistently. Light is sensitive to defects even at the atom level and the resulting losses and reflections cascade through the circuit making intricate devices exceedingly challenging to realise.

Despite the challenges there are already a host of uses for integrated photonics, e.g. transmitters and receivers for fibre optic communication, a host of

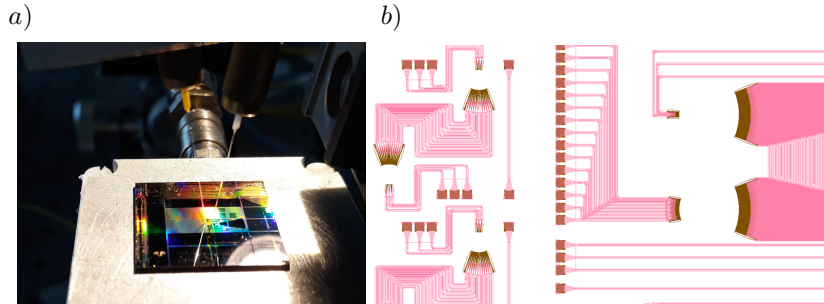


Figure 1.1: a) A chip with integrated circuits at a measurement stage and two fibers for coupling light in and out of the circuit. b) The CAD schematic of such a circuit.

different medical sensors focused on sensing insulin and other substances in the body. It demonstrates that the fabrication technology is mature enough for a micro-optomechanical sensor (MOEMS) such as the mass sensor.

Since an integrated optical vibration detection method has been proven to be competitive with other methods, it is interesting that it is also possible to drive the vibrations with an optical force. Two optical waveguides in very close proximity can be made to attract or repel each other when there is light in the waveguides [18]. This kind of all-optical drive and detection approach has been suggested before [19, 20] but in this work we propose using a slot waveguide which has been shown to generate more than ten times stronger force than standard waveguides for the same optical power.

The strong optical forces in a slot waveguide should be able to excite much stronger vibrations than comparable resonators using the same given optical power. The strong vibrations should lead to a reduction in the phase noise as well as an improved mass sensitivity. Since the device is not using any wavelength dependent components the vibrations can be detected by using broadband light sources or non-tuneable lasers which together with the simple fabrication process keeps the cost low.

Therefore, in the first part of this thesis we will investigate the use of slot waveguides as inertial mass sensors.

1.4 The design of our mass sensor

Our proposed mass sensor is illustrated in figure 1.2. By putting two thin silicon cantilevers very close to each other they will function as a slot waveguide. To focus light into the cantilever slot we have chosen to use a multimode interferometer (MMI). It is a very wide optical waveguide which uses interference between several optical modes to couple light between waveguides. The block-like MMI offers a good anchoring for a mechanical resonator. The sensor consists of 2 to

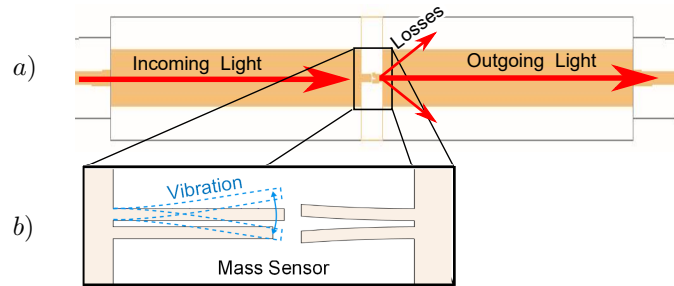


Figure 1.2: a) An illustration of the mass sensor and the coupling to and from it. 2) By guiding light in the slot between two cantilevers it generates a strong force between them driving a vibration. How well light couples to the other slot is dependent on how the first slot is deformed by the vibration.

$6\ \mu\text{m}$ long, $280\ \text{nm}$ wide cantilevers that are etched out of a $220\ \text{nm}$ thick layer of silicon. The slot between the cantilevers is $100\ \text{nm}$ wide. The receiving slot waveguide slot is widened to $280\ \text{nm}$ in order to increase the displacement sensitivity but then tapered down to the same dimensions as the sensor waveguide. In cases where it is not specified we are using the $6\ \mu\text{m}$ sensor cantilever as it gives the strongest signal.

1.5 Brillouin scattering

The optomechanical force that drives the mass sensor is present also in the waveguides used to route light around the circuit. If it were not for damping via the substrate these waveguides would vibrate as well. The difference is that unlike the single resonator case the waveguide acts as a continuous set of mechanical resonators coupled to the same optical drive. Physically the strain caused by an acoustic wave that is propagating through a waveguide results in a periodic change in the refractive index which in turn scatters the light. This process is called Brillouin scattering and is well studied in long conventional optical fibres but still relatively new in integrated optics where the interaction is much stronger but the length of the waveguide much shorter [21].

Brillouin scattering or "*the inelastic scattering of light caused by acoustic phonons*" was suggested by both Brillouin in 1922 [22] and Mandelstam in 1926 [23], the latter is believed to have recognised the phenomenon almost a decade before his publication. When the light amplifies these phonons it is called stimulated Brillouin scattering (SBS), and it was demonstrated in 1964 by Chiao et al [24]. It is capable of both up and down conversion of the frequency as well as forward and backwards scattering of the light.

SBS in fibres has been used to make distributed temperature or strain sensors

[25] which can be can be integrated into large and long structures such as bridges. The method is quite simple and can easily be understood when you know that the properties of silica that decide which acoustic frequencies can be excited are both temperature and strain dependent. The Brillouin frequency, as it is called, can be tracked by continuously measuring the frequency shift of the light reflected when coupling a strong laser to the fibre.

It has also been used to amplify weak signals [26]. A strong pump laser separated from the weak signal by the Brillouin frequency will generate an acoustic vibration proportional to the signal. The intensity of the light scattered from the pump to the signal frequency is proportional to the vibrations. A Brillouin waveguide can in this way function as a gain medium and be used to amplify the signal.

Brillouin scattering in regular optical fibres is mostly due to the strain induced by the acoustic wave and how it affects the refractive index but the acoustic wave also warps the shape of the waveguide itself. For waveguides with sub-wavelength features such as photonic crystal fibres and those used in integrated photonics, these shape changes can have a significant impact on the optical properties. It has been shown that this kind of optomechanical coupling, called radiation pressure, is in some waveguides able to generate stronger forces than the electrostrictive force.

Smaller waveguides also mean that the light is focused into a smaller optical mode increasing the intensity of the light and the nonlinear interaction. A host of promising applications like small footprint narrow linewidth lasers [27, 28] and tunable dynamic gratings [29] have already been demonstrated and there is the hope that many more will follow [30].

1.6 Algorithmic design and optimization of Brillouin active waveguides

The magnitude of the SBS coupling is dependent on both optical modes, the one mechanical mode, the overlap between them all, the optical group velocity and several other properties. It can be difficult without simulation tools to estimate how good a novel waveguide is for Brillouin scattering or what changes are needed to make it better. Since Brillouin scattering was first demonstrated the majority of the development has been focused on finding the right material system and not so much on the shape of the waveguide. A way of addressing this gap is to rely on computational aids.

For a computer to be able to run an algorithm with such a purpose, the waveguides need to be parametrised in a flexible way so that any shape can be described. We have chosen to rasterise the waveguide into a 17 by 14 pixel grid. With three possible materials to assign to each element (silicon, silicon oxide, air) it quickly expands to 10^{113} possible waveguide shapes. Even if many of these waveguides are functionally identical it is unrealistic to test the performance of all of them.

Evolutionary algorithms are a class of general purpose search algorithms based on an iterative approach and it has been used to solve optical problems before [31–33]. Evolutionary algorithms mimic evolutionary pressure, genetic crossover and mutation to generation by generation generate and select the best candidate solutions to a problem. With this approach, evolutionary algorithms have been shown to provide often counter-intuitive but educational answers in domains ranging from the growth of plants and website design to Othello strategies [34–36].

In the second part of this work, we will design a genetic algorithm that we then use to optimize the SBS gain over a wide range of mechanical frequencies. This way we find several different types of waveguides excelling their SBS gain while providing a diverse range of other metrics, such as group index, mass or frequency. We are also discussing the general trends in the accumulated data.

1.7 Outline

The thesis is organized as follows:

- Chapter 2 is focused on optomechanical interactions in optical waveguides. It aims at introducing the relevant analytic tools to model mechanical resonators and optomechanical forces. It also includes a brief presentation of the alternative to optomechanical designs to place the work in a relevant context. Finally, it includes an introduction to coupled resonator systems, nonlinear resonators and frequency noise.
- Chapter 3 is focused on the design, fabrication and measurement of the mass sensor. It starts with an introduction to the parameters that qualify a mass sensor: the mass responsivity and the mass sensitivity. Following that is an exposition on the mass sensor and the considerations taken around the slot waveguide design. It also includes an investigation on a novel mass sensing design utilising the synchronisation conditions of dissipative coupling. Next is a section about the fabrication process and one about the measurement of the signal and the noise.
- Chapter 4 is focused on the design of the genetic algorithm. Genetic algorithms are designed to find a sufficiently good solution to an optimisation problem often using incomplete or imperfect information or limited computation capacity. Generally, this is made more difficult by that the set of solutions is too large to be adequately sampled. Genetic algorithms are inspired by natural selection and rely on bio-inspired operators such as mutation, crossover and selection.
- Chapter 5 focuses on Brillouin scattering and how light propagates along waveguides and interacts with the light. It starts with a short description of what makes Brillouin scattering different from the resonator case and the metrics that are used to qualify it. Then follows an analysis of the results of the genetic algorithm, both individual waveguides and the more overarching trends.
- The last chapter contains a conclusion of the work as well as a few suggested future projects.

1.8 Publications

1.8.1 Publications in international journals

1. Jesper Håkansson, and Dries Van Thourhout. "Generating novel waveguides for stimulated Brillouin scattering with genetic algorithms." *APL Photonics* 4.1 (2019): 010803.
2. Jesper Håkansson, Bart Kuyken, and Dries Van Thourhout. "Strong forces in optomechanically actuated resonant mass sensor." *Optics express* 25.25 (2017): 30939-30945.

1.8.2 Publications in international conferences

1. Jesper Håkansson, and Dries Van Thourhout, Generating novel waveguides for stimulated Brillouin scattering with genetic algorithms, Conference on Lasers and Electro-Optics (CLEO), Munich, Germany, (2019).
2. Jesper Håkansson, and Dries Van Thourhout, Strong quadratic coupling in slotted photonic crystal pair, Proceedings Symposium IEEE Photonics Society Benelux, 2016, Ghent, Belgium, (2016).
3. Jesper Håkansson, and Dries Van Thourhout, New integrated platforms for optomechanics, ITN-cQOM workshop, (2015).
4. Jesper Håkansson, and Dries Van Thourhout, Optomechanically actuated slot cantilever for mass sensing., Proceedings of the 2013 Annual Symposium of the IEEE Photonics Society Benelux Chapter, Netherlands, (2013).

References

- [1] Gerd Binnig, Calvin F Quate, and Ch Gerber. *Atomic force microscope*. *Physical review letters*, 56(9):930, 1986.
- [2] Thomas Thundat, R Js Warmack, GY Chen, and DP Allison. *Thermal and ambient-induced deflections of scanning force microscope cantilevers*. *Applied Physics Letters*, 64(21):2894–2896, 1994.
- [3] JR Barnes, RJ Stephenson, CN Woodburn, SJ Oshea, ME Welland, T Rayment, JK Gimzewski, and Ch Gerber. *A femtojoule calorimeter using micromechanical sensors*. *Review of Scientific Instruments*, 65(12):3793–3798, 1994.
- [4] T Thundat, EA Wachter, SL Sharp, and RJ Warmack. *Detection of mercury vapor using resonating microcantilevers*. *Applied Physics Letters*, 66(13):1695–1697, 1995.
- [5] Thomas Braun, Murali Krishna Ghatkesar, Natalija Backmann, Wilfried Grange, Pascale Boulanger, Lucienne Letellier, Hans-Peter Lang, Alex Bitsch, Christoph Gerber, and Martin Hegner. *Quantitative time-resolved measurement of membrane protein–ligand interactions using microcantilever array sensors*. *Nature nanotechnology*, 4(3):179, 2009.
- [6] Karin Y Gfeller, Natalia Nugaeva, and Martin Hegner. *Micromechanical oscillators as rapid biosensor for the detection of active growth of Escherichia coli*. *Biosensors and Bioelectronics*, 21(3):528–533, 2005.
- [7] Taechung Yi and Chang-Jin Kim. *Measurement of mechanical properties for MEMS materials*. *Measurement Science and Technology*, 10(8):706, 1999.
- [8] Adam R Krause, Charles Van Neste, Larry Senesac, Thomas Thundat, and Eric Finot. *Trace explosive detection using photothermal deflection spectroscopy*. *Journal of Applied Physics*, 103(9):094906, 2008.
- [9] Anja Boisen, Søren Dohn, Stephan Sylvest Keller, Silvan Schmid, and Maria Tenje. *Cantilever-like micromechanical sensors*. *Reports on Progress in Physics*, 74(3):036101, 2011.
- [10] Marcio G von Muhlen, Norman D Brault, Scott M Knudsen, Shaoyi Jiang, and Scott R Manalis. *Label-free biomarker sensing in undiluted serum with suspended microchannel resonators*. *Analytical chemistry*, 82(5):1905–1910, 2010.

-
- [11] Julien Chaste, A Eichler, J Moser, G Ceballos, R Rurali, and A Bachtold. *A nanomechanical mass sensor with yoctogram resolution*. *Nature nanotechnology*, 7(5):301, 2012.
- [12] Wenyan Yu, Wei C Jiang, Qiang Lin, and Tao Lu. *Cavity optomechanical spring sensing of single molecules*. *Nature communications*, 7:12311, 2016.
- [13] KL Ekinici, XMH Huang, and ML Roukes. *Ultrasensitive nanoelectromechanical mass detection*. *Applied Physics Letters*, 84(22):4469–4471, 2004.
- [14] Kirill Zinoviev, Carlos Dominguez, Jose Antonio Plaza, Víctor Javier Cadarso Busto, and Laura M Lechuga. *A novel optical waveguide microcantilever sensor for the detection of nanomechanical forces*. *Journal of Lightwave Technology*, 24(5):2132, 2006.
- [15] Christopher R Doerr and Roel Baets. *Special Issue of Silicon Photonics [Scanning the Issue]*. *Proceedings of the IEEE*, 106(12):2098–2100, 2018.
- [16] Hao Xu, Xianyao Li, Xi Xiao, Peiji Zhou, Zhiyong Li, Jinzhong Yu, and Yude Yu. *High-speed silicon modulator with band equalization*. *Optics letters*, 39(16):4839–4842, 2014.
- [17] Milan M Milosevic, Stevan Stanković, Scott Reynolds, Thalía Domínguez Bucio, Ke Li, David J Thomson, Frederic Gardes, Graham T Reed, et al. *The emergence of silicon photonics as a flexible technology platform*. *Proceedings of the IEEE*, (99):1–16, 2018.
- [18] Dries Van Thourhout and Joris Roels. *Optomechanical device actuation through the optical gradient force*. *Nature Photonics*, 4(4):211, 2010.
- [19] Mo Li, WHP Pernice, and HX Tang. *Broadband all-photonics transduction of nanocantilevers*. *Nature nanotechnology*, 4(6):377, 2009.
- [20] Dmitry Yu Fedyanin and Yury V Stebunov. *All-nanophotonic NEMS biosensor on a chip*. *Scientific reports*, 5:10968, 2015.
- [21] Heedeuk Shin, Wenjun Qiu, Robert Jarecki, Jonathan A Cox, Roy H Olsson III, Andrew Starbuck, Zheng Wang, and Peter T Rakich. *Tailorable stimulated Brillouin scattering in nanoscale silicon waveguides*. *Nature communications*, 4:1944, 2013.
- [22] Léon Brillouin. *Diffusion de la lumière et des rayons X par un corps transparent homogène-Influence de l'agitation thermique*. In *Annales de physique*, volume 9, pages 88–122. EDP Sciences, 1922.
- [23] LI Mandelstam. *Light scattering by inhomogeneous media*. *Zh. Russ. Fiz-Khim. Ova*, 58:381, 1926.

- [24] RY Chiao, CH Townes, and BP Stoicheff. *Stimulated Brillouin scattering and coherent generation of intense hypersonic waves*. *Physical Review Letters*, 12(21):592, 1964.
- [25] D Culverhouse, F Farahi, CN Pannell, and DA Jackson. *Potential of stimulated Brillouin scattering as sensing mechanism for distributed temperature sensors*. *Electronics Letters*, 25(14):913–915, 1989.
- [26] NA Olsson and JP Van der Ziel. *Cancellation of fiber loss by semiconductor laser pumped Brillouin amplification at 1.5 μm* . *Applied physics letters*, 48(20):1329–1330, 1986.
- [27] Nils T Otterstrom, Ryan O Behunin, Eric A Kittlaus, Zheng Wang, and Peter T Rakich. *A silicon Brillouin laser*. *Science*, 360(6393):1113–1116, 2018.
- [28] Irina V Kabakova, Ravi Pant, Duk-Yong Choi, Sukhanta Debbarma, Barry Luther-Davies, Stephen J Madden, and Benjamin J Eggleton. *Narrow linewidth Brillouin laser based on chalcogenide photonic chip*. *Optics letters*, 38(17):3208–3211, 2013.
- [29] Ravi Pant, Enbang Li, Christopher G Poulton, Duk-Yong Choi, Steve Madden, Barry Luther-Davies, and Benjamin J Eggleton. *Observation of Brillouin dynamic grating in a photonic chip*. *Optics letters*, 38(3):305–307, 2013.
- [30] Moritz Merklein, Alvaro Casas-Bedoya, David Marpaung, Thomas FS Büttner, Mattia Pagani, Blair Morrison, Irina V Kabakova, and Benjamin J Eggleton. *Stimulated Brillouin scattering in photonic integrated circuits: novel applications and devices*. *IEEE J. Sel. Top. Quant*, 22:336–346, 2016.
- [31] Jyun-Hong Lu, Dong-Po Cai, Ya-Lun Tsai, Chii-Chang Chen, Chu-En Lin, and Ta-Jen Yen. *Genetic algorithms optimization of photonic crystal fibers for half diffraction angle reduction of output beam*. *Optics express*, 22(19):22590–22597, 2014.
- [32] Joel Goh, Ilya Fushman, Dirk Englund, and Jelena Vučković. *Genetic optimization of photonic bandgap structures*. *Optics express*, 15(13):8218–8230, 2007.
- [33] Stefan Preble, Michal Lipson, and Hod Lipson. *Two-dimensional photonic crystals designed by evolutionary algorithms*. *Applied Physics Letters*, 86(6):061111, 2005.

-
- [34] Juan C Quiroz, Sushil J Louis, Anil Shankar, and Sergiu M Dascalu. *Interactive genetic algorithms for user interface design*. In Evolutionary Computation, 2007. CEC 2007. IEEE Congress on, pages 1366–1373. IEEE, 2007.
- [35] Liang Xu, Mu Tao, and Huang Ming. *A hybrid algorithm based on genetic algorithm and plant growth simulation algorithm*. In Measurement, Information and Control (MIC), 2012 International Conference on, volume 1, pages 445–448. IEEE, 2012.
- [36] Jean-Marc Alliot and Nicolas Durand. *A genetic algorithm to improve an othello program*. In European Conference on Artificial Evolution, pages 305–319. Springer, 1995.

2

Optomechanical Resonators

2.1 Introduction

This chapter is focused on optomechanical interactions in optical waveguides. It aims at introducing the relevant analytic tools to model mechanical resonators and optomechanical forces. It also includes a brief presentation of the alternative to optomechanical designs in order to place the work in a relevant context. Finally, it includes an introduction to coupled resonator systems, nonlinear resonators and frequency noise.

2.2 Mechanical resonators

Being able to model and understand the mechanical properties of a MEMS structure is, of course, essential to their design. Mechanics is an old discipline originating in ancient Greece and then via Newton, Euler, Lagrange and many others, it has continued to develop to this day. Mathematically mechanics has two principal branches: Lagrangian mechanics and Hamiltonian mechanics. Neither of them is fundamentally different from Newtonian mechanics, but their mathematical approach makes many problems easier to work with. The vectors that represent forces and speeds in Newtonian mechanics are reformulated as scalars. Lagrangian mechanics instead approach the problem from the difference between the kinetic and potential energy and the flux between those two forms of energy. This way the forces that can be derived are placed in a generalised coordinate system. The

energy terms can often be written so that redundant terms disappear and so it simplifies the constraints of the system. Hamiltonian mechanics instead works with the sum of the energies of the system, making it well suited for accounting for where the energy is that it is conserved. It often offers an easier way to deal with mechanical energy and momentum. Before that becomes relevant the mechanical problem must be broken down into parameters that can be worked with.

2.2.1 Resonance frequency

The most essential of the parameters of mechanical resonators is perhaps the resonance frequency. It can be calculated in several ways depending on the assumptions we start with. One way is to write down the different forces acting locally upon the structure as it is deformed and equating them to the inertia force from Newton's third law. For a simple resonator, the differential equation of a segment can look something like this,

$$K(\Phi(r, t)) - \rho(r)\ddot{\Phi}(r, t) = 0 \quad (2.1)$$

where K is a function calculating the force restoring the structure to a relaxed state from a displacement and $\rho(r)$ the density. $\Phi(r, t)$ and $\ddot{\Phi}(r, t)$ represent the displacement and acceleration of that structure at the point, r , and time, t .

Using the Fourier method the velocity of the structure can be separated into a spatial mode shape and a time-dependent oscillation and can be written down as $\Phi(r, t) = \tilde{\phi}(r)e^{i\omega t}$. The mode shape can be calculated by finding shapes which satisfy the spatial part of the differential equations and the boundary conditions implied from how the boundary interacts with the surrounding.

The second time derivative of the displacement gives the acceleration, $\ddot{\Phi}(r, t) = -\tilde{\phi}(r)\omega^2 e^{i\omega t}$. By introducing the now calculated mode shape into equation (2.1) and using the time independent frequency term in the acceleration it is then possible to solve for the resonance frequency.

Rayleigh's quotient offers another way for calculating resonance frequencies under the added assumption that the system is lossless and that the mode shape is known. The total mechanical energy of the system is the sum of the kinetic energy and the potential energy. The system transfers the energy between the extremes of an only kinetic energy state to an only potential energy state and then back again. From that, it can be assumed that the maximum kinetic energy is the same as the maximum potential energy,

$$W_{kin}(t_{max,kin}) = W_{pot}(t_{max,pot}) \quad (2.2)$$

In a linear system, the potential energy is proportional to the square of the displacement and the kinetic energy is proportional to the square of the veloc-

ity. The kinetic energy of an object can be written as $W_{kin} = \dot{\Phi}^2 m/2$. Using the same separation of spatial and temporal displacement dependencies as before, $\dot{\Phi}(r, t) = i\omega\tilde{\phi}(r)e^{i\omega t}$, it is possible to break out the frequency from the velocity term. The kinetic energy can then be rewritten as,

$$W_{kin,max} = \frac{\omega^2}{2} \int_V \tilde{\phi}^2(r)\rho(r) dr \quad (2.3)$$

where V is the whole structure. Since the potential energy is independent of the speed, it is possible to solve equation (2.2) for the resonance frequency,

$$\omega^2 = \frac{W_{pot}(\Phi(t_{max,pot}))}{\frac{1}{2} \int_V \tilde{\phi}^2(r)\rho(r) dr} \quad (2.4)$$

2.2.2 Lumped parameters models

The easiest way to describe a mechanical resonator is often as a harmonic oscillator, a point mass on a spring where the restoring force is linear to the displacement. In this model the resonance frequency is $\omega^2 = k/m$, where k is the stiffness of the spring and m is the mass. This model is great to work with but looking at the earlier expression, eq. 2.4, not all of the mass of the resonator contribute equally to the resonance frequency. This is because not all of the resonator move at the same speed. It is therefore common to reduce the mode shape to effective parameters, $\omega^2 = k_{eff}/m_{eff}$. The effective mass, m_{eff} , can be calculated from the expression,

$$m_{eff} = \int_V \phi^2(r)\rho(r)dr \quad (2.5)$$

where ϕ is the normalized mode shape. It relates to the previous expression of the mode shape as $\tilde{\phi}(r) = a\phi(r)$. It is important to note that the effective mass varies with the normalization point. In this work the effective mass has been normalised to the maximum displacement of the mode, $\max(\phi) \equiv 1$, as it is convenient for the displacement sensing method we are using. A similar treatment can be given to the stiffness. A single amplitude value, a , can then be used to represent the amplitude of the whole mode.

The amplitude of a vibration can be calculated using the effective parameters if we also introduce the forces related to friction losses. The actual sources of these losses we get to in a section a bit later in the thesis. A term c_n is introduced to represent the coefficient for the viscous force working on a mode, n . The forces can then be written as,

$$m_{eff,n}\ddot{a}_n + c_n\dot{a}_n + k_{eff,n}a_n = F_{eff,n} \quad (2.6)$$

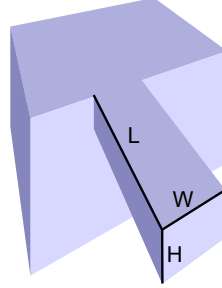


Figure 2.1: Drawing of a cantilever.

The quality factor is another parameter often used to quantify the losses. It relates to the viscous coefficient as $Q = m_{eff}\Omega/c$. For a linear resonator the stiffness can be eliminated from the equation using the resonance frequency $\Omega = \sqrt{k_{eff}/m_{eff}}$. The equation (2.6) for an oscillating force can be rewritten to solve for the complex amplitude,

$$a_n(\omega) = \frac{F_{eff,n}}{m_{eff,n}((\Omega_n^2 - \omega^2) + i\Omega_n\omega/Q_{mech,n})} \quad (2.7)$$

$$= \chi_n(\omega)F_{eff,n} \quad (2.8)$$

where ω is the frequency of the oscillating force and χ is the mechanical susceptibility function. Both the amplitude and the phase response can be calculated from the complex amplitude, ($a_n = Ae^{iB}$).

$$A_n = |a_n| = \frac{F_{eff,n}}{m_{eff,n}\sqrt{(\Omega_n^2 - \omega^2)^2 + (\Omega_n\omega/Q_{mech,n})^2}} \quad (2.9)$$

$$B_n = \text{angle}(a_n) = \arctan\left(\frac{\Omega_n\omega/Q_{mech,n}}{\Omega_n^2 - \omega^2}\right) \quad (2.10)$$

2.2.3 Analytical solutions to cantilevers

A straightforward but somewhat simplistic model for cantilevers is Euler-Bernoulli beam theory which is a special case of Timoshenko beam theory. Euler-Bernoulli beam theory ignores rotational inertia and shear deformation so it is valid only for small deflections and lateral forces. It will suffice until we get to the discussion of nonlinear properties. It is a well-documented theory which has been further expanded upon in several sources, e.g. [1]. Rather than deriving 200-year-old equations in detail I have chosen to provide just the relevant equations and assumptions to guide further discussion.

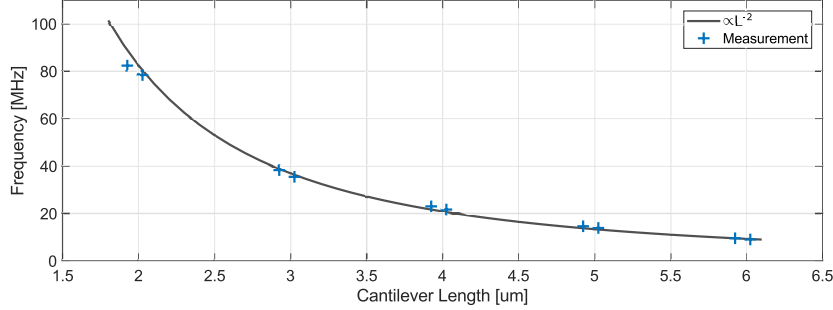


Figure 2.2: Resonance frequency measurements of a series of cantilevers of different length compared to the inverse square dependency on length expected from classic beam theory.

The forces working on the beam can be described as bending rigidity, inertia forces and external forces. Written as an equation it comes to,

$$EI \frac{\partial^4 \Phi(x, t)}{\partial x^4} + \rho A \frac{\partial^2 \Phi(x, t)}{\partial t^2} = F_{ext}(x, t) \quad (2.11)$$

where E and ρ are the material constants: Young's modulus and density. I and A are the geometric moment of inertia and the area of the cross-section.

We make the ansatz of separating the time and spatial variables, $\Phi(x, t) = \tilde{\phi}(x)\tilde{\tau}(t)$. By assuming that the cantilever is fixed at the anchoring point, $\tilde{\phi}(0)$, and free at the tip, $\tilde{\phi}(L)$, we can write down the boundary conditions,

$$\tilde{\phi}(0) = \frac{d\tilde{\phi}(0)}{dx} = \frac{d^2\tilde{\phi}(L)}{dx^2} = \frac{d^3\tilde{\phi}(L)}{dx^3} = 0 \quad (2.12)$$

If we assume the restoring force is linear to displacement we can use the harmonic oscillator model for the temporal component, $\tilde{\tau}(t) = e^{i\Omega t}$.

- The resonance frequency can be calculated from,

$$\Omega_{mech, n} = \frac{\lambda_n^2}{L^2} \sqrt{\frac{EI}{\rho A}} = \lambda_n^2 \frac{W}{L^2} \sqrt{\frac{E}{12\rho}} \quad (2.13)$$

L , W and H are the length, width and thickness of the beam, as drawn in figure 2.1. λ_n is a constant that satisfies the boundary conditions and relates to the wavenumber β_n via,

$$\lambda_n = \beta_n L = [1.8751, 4.6941, 7.8548, (2n - 1)\pi/2] \quad (2.14)$$

The calculated frequency is often a bit higher than the fabricated result because the model assumes the base of the cantilever does not move. Measure-

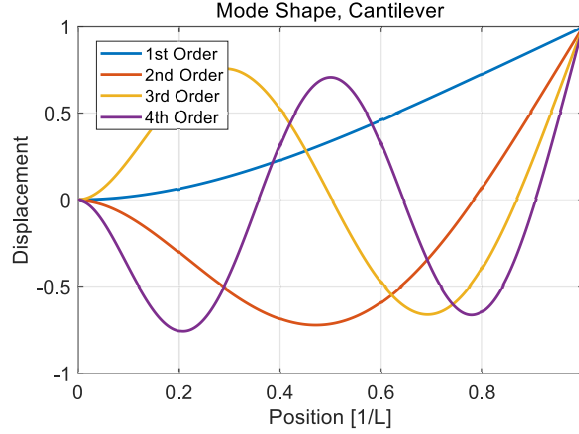


Figure 2.3: The mode shapes of the first few orders of resonances of a cantilever. The equations are given in equation 2.15.

ments of the mechanical frequency of fabricated cantilevers can be found in figure 2.2.

- The mode shape can be written as,

$$\phi_n(x) = \frac{1}{2} \left(\cos(\beta_n x) - \cosh(\beta_n x) - \frac{\cos(\beta_n x) + \cosh(\beta_n x)}{\sin(\beta_n x) + \sinh(\beta_n x)} (\sin(\beta_n x) - \sinh(\beta_n x)) \right) \quad (2.15)$$

It is worth reiterating the mode is normalized to the peak, $\phi_n(L) \equiv 1$, as is the effective mass and force, see figure 2.3b.

- From the mode shape it is then possible to calculate an effective mass fraction which relates the resting mass of the cantilever to the effective mass of its respective modes. The value is for cantilevers almost independent of mode order.

$$m_{frac,n} = m_{eff,n}/m_{rest} \approx .25 \quad (2.16)$$

The force that is participating in the drive of the cantilever is however still mode dependent. It can be calculated in the same manner as the effective mass.

$$f_{frac,n} = \int \phi_n(r) F dr = [.39, .22, .13, \dots] FL \quad (2.17)$$

where F is the driving force per length.

2.2.4 Perturbing the mechanical resonator

Small changes to the shape of a resonator are reflected in the resonance frequency. As oxide builds upon the silicon surface, as fabrication inevitably leaves some surface roughness or (important for mass sensors) as samples get deposited on the resonator the stiffness and mass of the resonator changes.

The kinetic energy and effective mass were addressed earlier and are trivial if the mode shape stays the same and the added mass and its position are known. The potential energy however has not been discussed yet. It comes from the force that restores the resonator to a relaxed state. Starting from the simplest case, the restoring force of a small cube that is squeezed along one axis is written as $F_{spr} = -kx$, where k is the spring constant and x is the displacement. An integral of the work performed to deform it gives a potential energy of $U_{pot} = -\frac{1}{2}kx^2$. This is for the one-dimensional case, expanded to three dimensions and using anisotropic material constants it becomes,

$$U_{pot,mat} = \sum_{ijkl} \int_V \frac{1}{2} C_{ijkl} \epsilon_{ij} \epsilon_{kl} dr \quad (2.18)$$

where C_{ijkl} is the elasticity tensor, ϵ_{ij} and ϵ_{kl} are the strains along their respective dimensions. Strain and elasticity are expanded upon in the materials section. If other forces contribute to the stiffness of the resonator, e.g. if the driving force depends on the shape of the resonator, it will need to be included as well. The influence on slot-waveguide resonators is addressed in the section with the same name.

If a test mass is deposited or an oxide is grown on the surface, strain at that surface it will carry over into the deposited material. As long as the change is small enough not to disturb the mode shape the new frequency will be,

$$\begin{aligned} \Omega_{new}^2 &= \frac{U_{pot} + \delta U_{pot}}{\frac{1}{2}(m_{eff} + \delta m_{eff})} = \frac{2U_{pot}}{m_{eff}} \left(1 + \frac{\delta U_{pot}}{U_{pot}}\right) \left(1 - \frac{\delta m_{eff}}{m_{eff}}\right) \\ &\approx \Omega_{old}^2 \left(1 + \frac{\delta U_{pot}}{\frac{1}{2}m_{eff}\Omega_{old}^2} - \frac{\delta m_{eff}}{m_{eff}}\right) \\ \Omega_{new} &\approx \Omega_{old} + \frac{\delta U_{pot}}{m_{eff}\Omega_{old}} - \frac{\Omega_{old}}{2} \frac{\delta m_{eff}}{m_{eff}} \end{aligned} \quad (2.19)$$

where δU_{pot} is the changes in potential. It is important to stress that the potential energy calculation uses the same normalisation as the effective mass.

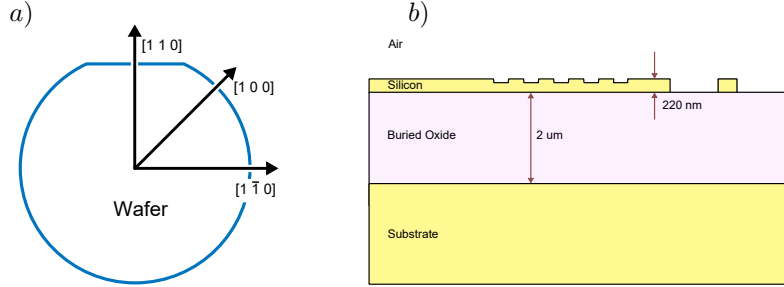


Figure 2.4: a) In-plane drawing of a $(1,0,0)$ wafer with arrows in the $[1,0,0]$ and $[1,1,0]$ direction. b) SOI material stack provided by the IMEC standard passives MPW. The top silicon layer is intended to guide the light and the buried oxide keeps that guiding layer far enough from the silicon substrate underneath.

2.3 Material properties

This section discusses the material parameters of the materials used, it also discusses the material properties and what they represent. Starting with optical, then mechanical and lastly optomechanical properties.

All the fabrication and measurements in this thesis have been carried out on devices in the silicon-on-insulator (SOI) platform. This is done in part because of the large experience the research group has in working with SOI as well as because both the mechanical and optical properties of silicon are competitive. Silicon-based materials are the dominant choice for cantilever sensors; they are well characterised and stable over time [2]. A competing material choice for cantilever sensors is polymers such as SU8. It is cheap and often easier to work with but very soft which makes it unsuitable for our application. The force in slot waveguides works only over a very short distance so to maximize the mechanical energy it is preferable to use a stiffer material. It is also unstable over more extended time periods and the mechanical losses are much higher.

The work with Brillouin scattering is theoretical and as such can easily be expanded to other material platforms such as chalcogenide which show impressive optomechanical interaction. The material properties of several of the more popular material platforms are therefore included.

2.3.1 Optical

The first thing to consider when choosing an optical material is transparency. Losing light to unwanted absorption is inevitably going to be a detriment and might even make it impossible to do anything at all. The SOI-platform is transparent from about $1.1\ \mu\text{m}$ to $3.7\ \mu\text{m}$. Physically the shorter wavelength limit is due to the lower band edge of silicon and the longer limit due to the onset of absorption

in silica. The transparency at 1550 nm is especially important to us as it enables us to use the cheap amplifiers, detectors and sources that are available in what is called the C-band, 1530 to 1565 nm. Since much of the work in the well-funded telecom industry is done in the C-band, development and the economics of scale has followed.

Waveguide losses are somewhat tricky to model since they often are a result of stochastic processes in fabrication. There is a material part, related not only to the inherent properties of the material but also its purity. Amorphous or polycrystalline silicon for example has much worse transmission than the monocrystalline configuration. Surface roughness dominates the propagation losses in silicon wire waveguides [3]. It is where small changes in the surface of a waveguide scatter the light. This roughness can come from the fabrication process but also the surface oxide forming when the silicon comes into contact with oxygen. It scales with the size of the roughness and the inverse of the wavevector [3]. Designwise wider waveguides with less confinement and less overlap between the optical power and surface roughness often have lower losses.

SOI allows for wire waveguide losses around $< .6$ dB/cm and rib waveguide losses below < 0.2 dB/cm [4]. These losses are in large part due to scattering from sidewall roughness and the rib waveguide design has a less confined waveguide mode, meaning a lower optical field strength at the sidewall, as well as less actual sidewalls to perform the scattering. This is also a major part of the reason slot waveguides show even higher losses (about 3.6 dB/cm [4]) than the conventional wire waveguide.

The SOI-platform also offers a high refractive index contrast between the waveguide material ($n_{Si} = 3.47$) and the insulator ($n_{SiO_2} = 1.48$). The high contrast allows for small waveguides, short bends and an overall reduction in the size of both the circuitry routing light to and from the mass sensor and a reduction of the size of the sensor itself. A smaller circuit is a cost-benefit as much of the associated processing costs scale with the footprint of the whole device. A smaller sensor is interesting because of the corresponding reduction of the effective mass and increase in mass sensitivity.

The high index contrast also means the light can be focused into a smaller waveguide. The field intensity increases when the same amount of optical power goes through a smaller cross-section. Both optomechanical forces and other effects that deformation has on an optical mode increases with that intensity.

2.3.2 Crystal Orientations

Since silicon is an anisotropic material with regards to its mechanical properties it is important to be able to keep track of and talk about the directions in the crystal lattice. This direction is often given in three value Miller index notation, $[h,k,l]$. It is a vector using the base vectors of the reciprocal lattice. The plane

orthogonal to that vector is written as (h,k,l). For convenience, since there are often many directions and planes with identical properties, the notation $\langle h,k,l \rangle$ denote all directions [h,k,l] that are identical and h,k,l denote all planes (h,k,l) that are identical. In silicon for example [1,0,0], [-1,0,0] and [0,1,0] can all be expressed as $\langle 1,0,0 \rangle$. The convention is that negative values are expressed with a bar, as an example $[\bar{1},0,0]$ instead of [-1,0,0]. The indexes should also be reduced so that their greatest common divisor is 1.

2.3.3 Mechanical

The material choice also has a significant effect on the properties of a mechanical resonator. Starting by explaining the two material properties in the cantilever resonance frequency equation: density and Young's modulus.

Density is the mass per volume of a material and of course mass as a property comes back in almost every dynamic model in mechanics. Relevant specifically for mass sensors is the mass responsivity which is maximised when the mass is low. However, the mass simultaneously appears in so many other properties that the advantage is not clear just from that. Table 2.1 gives the density for some of the relevant materials.

The Young's modulus is a scalar property describing the stiffness of the material. The stiffness gives how large pressure onto a surface is needed to deform a material by a given fraction of its length. Imagine a cube with the length L in all dimensions with the force F acting on one surface. The Young's modulus can be written as,

$$E = \frac{\sigma}{\epsilon} = \frac{F/A}{\delta L_{par}/L} \quad (2.20)$$

where $\sigma = F/A$, called the stress, is the pressure upon the surface and $\epsilon = \delta L_{par}/L$, called the strain, is the change in length of the cube divided by the original length of the cube (both lengths measured in the direction of the force). In the special case of cantilevers the strains are dominantly along the length of the cantilever and therefore it is possible to stay with this 1-dimensional model and treat silicon as an isotropic material, with a Young's modulus $E_{Si,\langle 1,1,0 \rangle} = 169$ GPa. The $\langle 1, 1, 0 \rangle$ orientation is mentioned because cantilevers and other long structures such as waveguides are throughout the thesis designed to extend along the $\langle 1, 1, 0 \rangle$ crystal orientation as it is praxis in silicon photonics. Silicon however is not isotropic and if the cantilevers were rotated to extend along the $\langle 1, 0, 0 \rangle$ direction the Young's modulus would be $E_{Si,\langle 1,0,0 \rangle} = 130$ GPa.

Paired with the Young's modulus is the Poisson's ratio, ν , which tells how much the material will expand or contract in the other directions as a response to the strain in the direction of the force.

Material	C_{11}	C_{12}	C_{44}	ρ	Ref.
c-Si	166	63.9	79.6	2329	[5]
SiO _x	78.6	16.1	31.2	2203	[6]
Ge	129	47.9	67.0	5323	[5]
GaAs	119	53.7	59.4	5340	[7–9]
InP	102	57.6	46.0	4787	[7, 9]
As ₂ S ₃	18.7	6.1	6.4	2595	[10]

Table 2.1: The values of are assuming the crystal orientation $(1, 0, 0)$.

$$\nu = -\frac{\delta L_{ort}}{\delta L_{par}} \quad (2.21)$$

For a 3-dimensional treatment of the stress and strain both Young's modulus and Poisson's ration are combined into an elastic compliance tensor, S_{ijkl} . It describes the constitutive relation between stress, σ_{ij} , and strain, ϵ_{ij} , and is written as,

$$\begin{bmatrix} \epsilon_{11} \\ \epsilon_{22} \\ \epsilon_{33} \\ \epsilon_{23} \\ \epsilon_{13} \\ \epsilon_{12} \end{bmatrix} = \begin{bmatrix} S_{11} & S_{12} & S_{13} & S_{14} & S_{15} & S_{16} \\ S_{21} & S_{22} & S_{23} & S_{24} & S_{25} & S_{26} \\ S_{31} & S_{32} & S_{33} & S_{34} & S_{35} & S_{36} \\ S_{41} & S_{42} & S_{43} & S_{44} & S_{45} & S_{46} \\ S_{51} & S_{52} & S_{53} & S_{54} & S_{55} & S_{56} \\ S_{61} & S_{62} & S_{63} & S_{64} & S_{65} & S_{66} \end{bmatrix} \begin{bmatrix} \sigma_{11} \\ \sigma_{22} \\ \sigma_{33} \\ \tau_{23} \\ \tau_{13} \\ \tau_{12} \end{bmatrix}$$

and conversely the elasticity tensor, C_{ijkl} , which instead gives the stress as a function of the strain,

$$C_{ijkl} = S_{ijkl}^{-1} \quad (2.22)$$

The strain tensor is defined as $\epsilon_{ij} = \frac{1}{2}(\frac{\partial u_j}{\partial x_i} + \frac{\partial u_i}{\partial x_j})$ where $\frac{\partial u_j}{\partial x_i}$ is the spatial displacement gradient in the dimensions i and j .

Crystalline silicon has a diamond cubic crystal structure, a structure it shares with germanium and of course carbon (diamond). This means it will have a cubic symmetry also in the compliance matrix and the photoelasticity matrix. A compliance tensor with cubic symmetry can be reduced to,

$$C_{3Sym} = \begin{bmatrix} C_{11} & C_{12} & C_{12} & 0 & 0 & 0 \\ C_{12} & C_{11} & C_{12} & 0 & 0 & 0 \\ C_{12} & C_{12} & C_{11} & 0 & 0 & 0 \\ 0 & 0 & 0 & C_{44} & 0 & 0 \\ 0 & 0 & 0 & 0 & C_{44} & 0 \\ 0 & 0 & 0 & 0 & 0 & C_{44} \end{bmatrix}$$

The corresponding values for silicon and more are given in table 2.1.

Unlike silicon, silica is an isotropic material. This means the material properties are independent of direction and that the compliance matrix can be simplified even further.

$$C_{Iso} = \frac{1}{E} \begin{bmatrix} 1 & -\nu & -\nu & 0 & 0 & 0 \\ -\nu & 1 & -\nu & 0 & 0 & 0 \\ -\nu & -\nu & 1 & 0 & 0 & 0 \\ 0 & 0 & 0 & 2(1+\nu) & 0 & 0 \\ 0 & 0 & 0 & 0 & 2(1+\nu) & 0 \\ 0 & 0 & 0 & 0 & 0 & 2(1+\nu) \end{bmatrix}$$

The parameters are given in the $\langle 1, 0, 0 \rangle$ crystal orientation but we mostly work in the $\langle 1, 1, 0 \rangle$ orientation so the compliance matrix needs to be rotated. This can be done by multiplying the matrix with a transformation matrix [11],

$$C_{mnop} = T(\theta)C_{ijkl}T^T(\theta) \quad (2.23)$$

The transformation matrix, T , is compounded of several rotation matrices, R , that has been cyclic column or row shifted and then element-wise multiplied. The rotation matrix is given by,

$$R(\theta) = \begin{bmatrix} \cos(\theta) & -\sin(\theta) & 0 \\ \sin(\theta) & \cos(\theta) & 0 \\ 0 & 0 & 1 \end{bmatrix} \quad (2.24)$$

The example given rotates the matrix around an axis in the third dimension but it can be reordered to rotate around any of the other two. The transformation matrix is in this case written as,

$$\begin{aligned} T(\theta) &= \begin{bmatrix} R_{(0,0)} \circ R_{(0,0)} & & R_{(1,0)} \circ R_{(-1,0)} \\ R_{(0,1)} \circ R_{(0,-1)} & R_{(1,1)} \circ R_{(-1,-1)} + R_{(-1,1)} \circ R_{(1,-1)} & \\ & & \end{bmatrix} \\ &= \begin{bmatrix} c^2 & s^2 & 0 & 0 & 0 & 2cs \\ s^2 & c^2 & 0 & 0 & 0 & -2cs \\ 0 & 0 & 1 & 0 & 0 & 0 \\ 0 & 0 & 0 & c & s & 0 \\ 0 & 0 & 0 & -s & c & 0 \\ -cs & cs & 0 & 0 & 0 & c^2 - s^2 \end{bmatrix} \end{aligned} \quad (2.25)$$

where $c = \cos(\theta)$ and $s = \sin(\theta)$.

Beyond mass and stiffness there are other material properties like thermal expansion, thermal conductivity, heat capacity and the Grüneisen parameter¹ all of which affect the quality factor. These will be further expanded upon in the mechanical losses section as they mediate the thermal losses.

¹The Grüneisen parameter is not only relevant to the quality factor but it also describes how the vibrational frequency of the material changes with strain. It appears in discussions on how the strain fields of different mechanical modes couple to each other or the thermal vibrations.

Material	λ [um]	p_{11}	p_{12}	p_{44}	n	Ref.
c-Si	1.15	-0.101	0.0094		3.47	
	3.39	-0.094	0.017	-0.051	3.47	[5]
SiO _x	0.63	0.121	0.270		1.48	[6]
Ge		-0.151	-0.128	-0.072	4.02	[5]
GaAs	1.55	-0.165	-0.14	-0.072	3.37	[8–10]
InP		-0.13	-0.11	-0.06	3.17	[7, 9]
As ₂ S ₃	1.55	0.25	0.24	0.005	2.37	[10]

Table 2.2: The values are assuming the crystal orientation $\langle 1, 0, 0 \rangle$ and are not necessarily at $1.55\mu\text{m}$ optical wavelength.

2.3.4 Photoelastic properties

The photoelastic effect is a material property that couples the mechanical strain to the optical refractive index. Because of this, it is often used to determine the stress in a material, particularly before the wide adoption of finite element method simulations. The effect is also utilised by acousto-optic modulators which with an acoustic wave creates a grating to scatter light. The effect is traditionally described by the equation [12],

$$\Delta\eta_{ij} = \Delta\left(\frac{1}{n^2}\right)_{ij} = p_{ijkl}S_{kl} \quad (2.26)$$

where η is the change in the optical impermeability tensor. p_{ijkl} and S_{kl} are the strain-optic tensor and the strain tensor. Since both η_{ij} and S_{kl} are typically symmetric the notation can often be reduced to, $\Delta\eta_i = p_{ij}S_j$, and the index ellipsoid is conveniently written as,

$$\begin{aligned} x^2\left(\frac{1}{n_x^2} + \sum_j p_{1j}S_j\right) + y^2\left(\frac{1}{n_y^2} + \sum_j p_{2j}S_j\right) + z^2\left(\frac{1}{n_z^2} + \sum_j p_{3j}S_j\right) \\ + 2yz \sum_j p_{4j}S_j + 2zx \sum_j p_{5j}S_j + 2xy \sum_j p_{6j}S_j = 1 \end{aligned} \quad (2.27)$$

where n_x , n_y and n_z are the principal indices of refraction and x , y and z are the components of a unitary propagation direction vector. The resulting forces are described in the electrostriction section.

2.4 Mechanical losses

The quality factor of the resonator is often one of the most important parameters to consider when dealing with sensing applications. It decides how selective the resonator is to incoming frequencies, how well a signal can build up, how quickly

it decays, how strongly it is affected by noise and with all that it comes back either directly or indirectly to influence almost every relevant parameter. Mathematically it is defined as,

$$Q = 2\pi \frac{\text{Energy Stored}}{\text{Energy Dissipated Per Cycle}} \quad (2.28)$$

The amplitude of the vibration scales with the quality factor and as such it decides to which extent the measurement signal drowns out the noise. On the other hand at high amplitudes the resonator becomes more susceptible to nonlinear effects. Alternating through the work the losses will be expressed as either a quality factor or as a loss rate ($\Gamma = \Omega/Q$) depending on which is the most convenient. Loss rates are often preferable to work with mathematically as it is a frequency and because of that the equations often become simpler.

$$\frac{\Omega}{Q_{total}} = \Gamma_{total} = \Gamma_{gas} + \Gamma_{clamp} + \Gamma_{ox} + \Gamma_{te} + \Gamma_{alk} + \dots \quad (2.29)$$

The different loss rates will be expanded upon in the following subsections. For the work with the mass sensor only air damping, oxide, clamping and thermoelastic losses are significant. This has to do with their relevance in the megahertz range and for silicon resonators. When working at higher frequencies Akhiezer losses start to be relevant.

2.4.1 Air damping

If nothing is done about it the dominant mechanical loss channel in most MEMS cantilevers is air damping. For a nanomechanical system such as ours the surface to volume ratio is exceptionally large which exacerbates the problem further than it would be for larger structures. Pragmatically it would be preferable to be able to work in air. With the need for vacuum comes the need for a vacuum chamber which adds a step to the measurement and interferes with biological samples and most deposition processes. It does however also reduce the quality factor of our mass sensor by two orders of magnitude so the motivation for working in vacuum is clear.

Gas damping can be classified in two pressure regions: the fluidic ($K_n \ll 1$) and the ballistic range ($K_n \gg 1$) [1]. They are divided by the Knudsen number, K_n , which compares the mean free path length of the gas, λ_{mfp} , with the dimension, D , of the structure.

$$K_n = \lambda_{mfp}/D \quad (2.30)$$

In atmospheric pressure $\lambda_{mfp} \approx 70$ nm, meaning nanometer structures straddle the divide already under normal circumstances.

Analytically there are three loss channels associated with air damping in the fluidic regime: particle collisions (\tilde{Q}_{PC}), viscous losses (\tilde{Q}_{Visc}) and squeezed film losses (\tilde{Q}_{SQ}) [13]. The particle collision losses are just that, the losses associated with the collisions between the resonator and individual gas molecules. The viscous losses are related to the friction in the gas and squeezed film losses relate to losses induced by the trapping of air in a slot between two layers.

$$\tilde{Q}_{PC} = \frac{3\pi\rho v_T W \Omega}{16p} \quad (2.31)$$

p and v_T is gas pressure and the average thermal velocity of gas molecules.

$$\begin{aligned} \tilde{Q}_{Visc} &= \rho W H^2 \Omega / c_{visc} \\ c_{visc} &= 3\pi\mu H + \frac{3\pi}{4} H^2 \sqrt{2\mu\rho_{gas}\Omega} \end{aligned} \quad (2.32)$$

ρ_{gas} and μ are the density and dynamic viscosity of the gas. c_{visc} is the viscous damping constant.

$$\tilde{Q}_{SQ} = \frac{\rho\Omega W h_{gap}^3}{\mu H^2} \quad (2.33)$$

H_{gap} is the width of the gap where the gas is squeezed.

For higher frequencies air damping is less of an issue [14] because the air is no longer able to respond to the mechanical motion when the resonance frequency approaches $1/\tau_{rlx}$. The relaxation time for air at ambient pressure is $\tau_{rlx} \approx 2.3ns$.

By putting the device in a vacuum chamber we can reduce the pressure and the system moves from the fluidic regime to the ballistic regime. There are analytical tools [1] for working at low pressures but using an accessible vacuum chamber we can show that air damping no longer is a dominant loss channel at the pressures we can reach. Figure 2.5 shows a measurement of the quality factor of the mass sensor described in the mass sensor section as a function of the pressure. The quality factors lack of response to pressure at low pressures suggests that we are limited by something else.

For reference, applied to our 10 MHz slot cantilever device we get $\tilde{Q}_{PC,6um} = 110$, $\tilde{Q}_{Visc,6um} = 89$ which in total gives a calculated air damping of $\tilde{Q}_{Air,6um} = 49$ which can be compared to the measured air damping of $Q_{Air,6um} = 50$.

2.4.2 Clamping losses

Clamping loss is a loss channel where the mechanical energy leaks out through the anchor of the resonator and into the substrate. Most applications require there to be some point where the resonator is connecting to the surrounding to suspend it

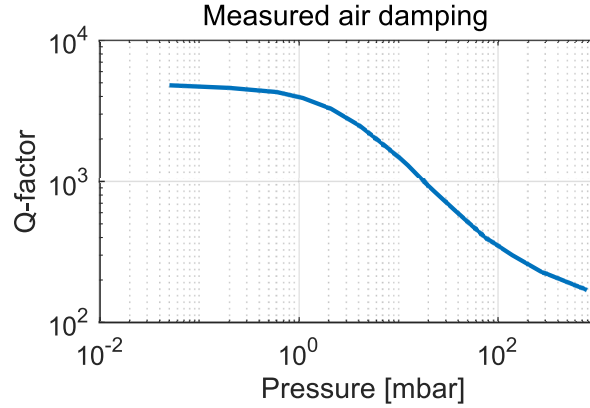


Figure 2.5: The measured mechanical quality factor of the mass sensing cantilever pair plotted against air pressure.

and as such clamping losses are often relevant. Luckily a lot can be done about it in the design process both by choosing the right materials and resonator types.

Our mass sensor cantilevers are anchored in a slab of silicon. The long and thin cantilevers have a much lower resonance frequency than the stiff bulk silicon so it can maintain a reasonably high-quality factor. The clamping losses for cantilevers have been solved analytically for when the substrate it is anchored in is extending in the direction normal to the vibrations [15]. That solution does however not directly translate to our situation where the vibrations are in the plane of the substrate.

Clamping losses are instead simulated using a finite element solver (FEM), COMSOL Multiphysics. By including a part of the substrate into the simulation of the resonator it is possible to simulate the perturbations of the anchoring as well as the vibrations radiating from the resonator and from that calculate the quality factor. By surrounding the added substrate with a perfectly matched layer (PML) the energy radiating into the substrate is absorbed, see figure 2.6. The losses give an imaginary component to the simulated resonance frequency. From that complex resonance frequency, Ω_{sim} , it is possible to calculate the clamping losses,

$$Q_{clamp} = \frac{\text{Re}(\Omega_{sim})}{2 \text{Im}(\Omega_{sim})} \quad (2.34)$$

where Ω_{sim} is the simulated resonance frequency. The 6 μm mass sensor is simulated to have Q-factor due to clamping losses of $Q_{clamp} = 2 \times 10^4$.

There are several design strategies to keep the energy from leaking out of the resonator [16]: Destructive interference, total internal reflection, geometric softening and phononic bandgaps.

The losses that do radiate out in the substrate can be canceled out by having an identical resonator radiating at opposite phase from a close by anchoring point i.e. a tuning fork. The phase difference is enforced by designing for a coupling strong enough to synchronise the two resonators. It is a relevant side note because particularly strong optomechanical forces are generated in slot waveguides which consists of two parallel waveguides forming a small slot in between them. The waveguide then conveniently already forms a pair of cantilevers anchored closely together. This will be expanded upon in the synchronisation subsection later in the chapter.

Analogous to how it works in optics the mechanical version of total internal reflection happens when the waves leave a material with a low speed of sound and enter a material with a higher speed of sound. If the angle of incidence is steep enough that the wave is scattered back into the slow medium then the reflectivity is total. So by surrounding an optical waveguide made from a material with a slow speed of sound with a cladding made from a material with a high speed of sound it is possible to confine a mechanical resonance in the waveguide.

The speed of sound ($v = \sqrt{E/\rho}$) in a material depends on the density, ρ , and stiffness, E . Silicon ($v_{Si,t} = 5843m/s$ for the transverse wave) has a faster speed of sound than oxide ($v_{SiO_2,t} = 5500m/s$ for the transverse wave) because it is stiffer and total internal reflection is therefore not a suitable method for confining a mechanical resonance. There are however other material platforms where such a method is possible such as chalcogenide [17].

If total internal reflection is not possible either because of the difference in the speed of sound or the incidence angle of the phonon it is sometimes possible to confine the vibration with a phononic crystal. Phononic crystals are periodic structures that have a band gap that forbids propagation of a specific frequency range of vibrations. Mechanical vibrations in the GHz range have a wavelength that is comparable to the 1550 nm optical wavelength we are working with which means it is possible to confine both sound and light with the same crystal. These kinds of structures called optomechanical crystals have managed to simultaneously achieve a strong optomechanical coupling as well as very high optical ($> 10^6$) and mechanical ($> 10^5$) quality factors [18].

Lastly, it is sometimes possible to clamp the structure only in parts of the structure that is not moving. Then there are no vibrations to leak through the structure. The simplest example is perhaps a tuning fork mentioned earlier.

2.4.3 Surface oxide

When silicon is exposed to air it quickly binds with the oxygen in the air forming a thin (about five atom layers) disordered oxide layer at the surface. The disorder of the oxide results in a disordered stress field forming at the surface which impacts optical and mechanical properties. It has been shown to influence optical

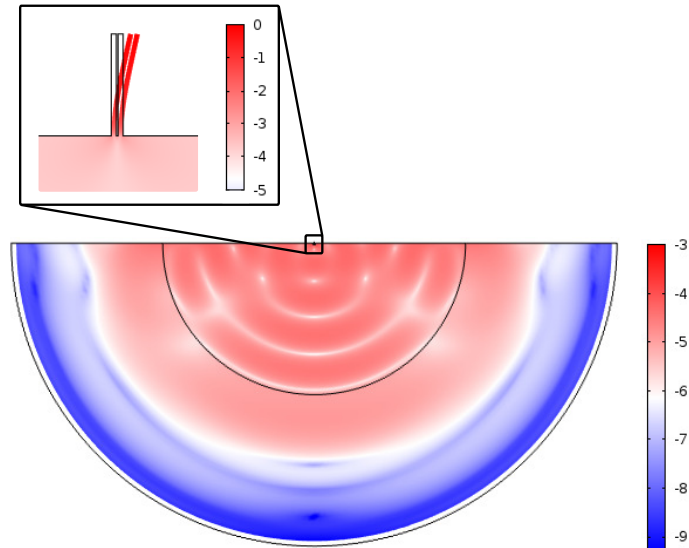


Figure 2.6: Mechanical mode leaking from the resonator into the substrate and then being absorbed in the outer circle to simulate clamping losses. Shown with \log_{10} scale and normalized to the maximum displacement.

surface scattering [19], two-photon absorption and free carrier lifetimes. On the mechanical side it has a definite effect on the quality factor [20].

Experiments, however, show that by removing the surface oxide of our cantilever the quality factors increases which when compared to literature suggests that clamping losses are not the dominant loss channel. The results of the experiment shown in figure 2.7 consists of a vacuum measurement of a driven resonator compared with another measurement after the surface oxide has been removed with a quick dip in HF, transported in a nitrogen filled container and the with an estimated total of 20 min of air exposure reintroduced in the vacuum chamber for another measurement. This increased the quality factor from 4000 to 6300. As a second reference air was then released in the vacuum chamber for an hour to rebuild the oxide after which it was again evacuated and another measurement was done. The quality factor was now reduced to 5100. The shift in frequency is due to the cantilever being thinned down as the oxide is removed and then in the second step due to the surface silicon turning into oxide which is softer.

Surface oxide dependent losses such as these are a known loss channel and can be managed by either avoiding air exposure, which can be impractical for many reasons, by coating the cantilever in a material with less friction such a nitride or even rebuilding the oxide in a more intentional fashion [20].

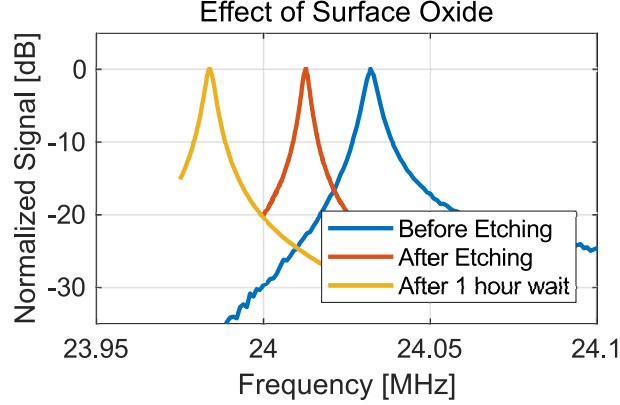


Figure 2.7: Measurements before removing the oxide give a Q -factor of 4000 which increases to 6300 after it is removed. The Q -factor then decreases to 5100 after an hour of air exposure.

2.4.4 Thermomechanical losses

There are also a few loss channels that are inherent to the resonator material itself like thermomechanical losses and Akhiezer losses.

Thermal expansion as a material property connects temperature with a change strain. So as the material is compressed or decompressed it heats up or cools down. If it is given time that temperature shift diffuses away relaxing some of that strain taking some of the potential energy with it. Thermoelastic damping is where thermal stress relaxes faster than the vibration. The thermal stress relaxation time, τ_{td} , depends on the thermal conductivity, κ , the specific heat capacity, C_V , and the width of the temperature/strain gradient, W_{tg} . It can be written as $\tau_{td} = W_{tg}^2 C_V / \pi^2 \kappa$. The magnitude of the thermoelastic damping can be calculated analytically [21].

$$\Gamma_{te} = \frac{\alpha^2 E T}{C_V} \frac{\omega \tau_{td}}{1 + (\omega \tau_{td})^2} \quad (2.35)$$

T , α are the mean temperature and thermal expansion coefficient. ω and E are the resonance frequency and the Young's modulus of the resonator. Often, however, it is preferable to simulate the damping in an FEM tool such as COMSOL. The low frequency cut-off of the damping is because thermal stress is a smaller portion of the potential energy of heavier and softer resonators.

Thermoelastic damping is often easiest managed by choosing a resonator material with good thermal properties but can otherwise be reduced in design. The losses are maximised when thermal diffusion time and the mechanical oscillation time are the same, $\tau_{td} = \omega^{-1}$. So designing the resonator for a uniform stress field

would eliminate the temperature gradient and thereby limit this kind of losses.

In regards to silicon cantilevers such as ours the thermoelastic losses typically peak around a few MHz making them relevant to consider. Simulations, however, show the quality factor to be 4×10^5 , almost two orders larger than the best quality factor we measured.

2.4.5 Akhiezer losses

Akhiezer damping is similarly to thermoelastic damping a thermomechanical loss channel. In this case, the losses are due to the heat flow between different mechanical modes. Non-linearities in the elasticity means the thermal vibration frequencies are modulated by the strain of the mechanical mode. The oscillating strain disturbs the thermal equilibrium and when the thermal vibrations relax the associated potential energy is lost with it. Akhiezer damping is different from thermoelastic damping in that it is present even in a homogenous stress field. The coupling between the stress field and the thermal resonances is modelled by the Grüneisen parameter [22]

2.5 Displacement Sensing

When using a cantilever as a mass sensor it is desirable to have as low an effective mass as possible as it makes the sample mass comparatively heavier and has a more significant impact on the resonance frequency. This typically leads to a smaller resonator and a higher resonance frequency. Movement in a smaller resonator is often more difficult to detect. It becomes difficult to integrate the sensor and the resonator has less of an impact on most properties that can be measured. The higher resonance frequency often means the resonator is stiffer, at least relative to the forces that can be generated to drive the resonator. The result is that the amplitude of the vibration is lower so the sensor must be more sensitive. Because of this there are several solutions for displacement sensing for MEMS and NEMS structures.

2.5.1 Capacitive detection

Capacitive detection is one of the cornerstones in the MEMS world. An electrode close to the resonator senses the displacement by detecting the capacitance change when the resonator moves. The electric charge, Q , stored in a capacitor is given by $Q = C(a)U$, where $C(a)$ and U are the capacitance as a function of displacement and the potential. If the potential is kept static then when the capacitor vibrates it periodically releases an electric charge. This current can be detected, and from it the motion can be calculated.

$$\frac{\partial Q}{\partial t} = \frac{\partial C(a)}{\partial a} \frac{\partial a}{\partial t} U \quad (2.36)$$

The signal increases with increasing potential, but the voltage also generates an attractive force,

$$F_C = \frac{1}{2} U^2 \frac{\partial C(a)}{\partial a} \quad (2.37)$$

Therefore a too high voltage risks collapsing the resonator. As a result, capacitive detection is limited by the sensitivity of the capacitance and the potential. The smaller the resonator, the less of an effect it will have on the capacitance and the higher the frequency, the smaller displacements will be that have to be measured. Therefore the capacitive system is often integrated with both filters and amplifiers to yield a signal that can be measured.

2.5.2 Piezoresistive Detection

Piezoresistive detection is based around the idea that strain induces a change in the resistivity of a material. By patterning the base of the cantilever with a small wire of, e.g. a gold-palladium alloy and integrating it in a circuit sensitive to the change the displacement can be detected. The wire, called a strain gauge, can be assumed to have a linear piezoresistive effect at small strains.

2.5.3 External interferometric detection

Interferometric detection is one of the most accurate methods but it is also difficult to integrate. A Michelson interferometer is a device that splits laser light into two separate paths. These beams are reflected and then superimposed. The resulting interference pattern can then be used to measure changes in the path difference between the two beams. The measurement is difficult to set-up because first there needs to be a mirror attached to the mechanical resonator, large enough to be a good reflector and in a place that is sensitive to the motion and second the laser light needs to be reflected off the mirror in a direction where it can be recollected which put a very high demand on the alignment.

2.5.4 Integrated optical phase detection

If the mechanical resonator also is an optical waveguide, it is possible to use the light passing through the waveguide to measure the vibrations. The speed of light in vacuum might be constant, but as soon as it is coupled into a material it gets slowed down by the light-matter interaction. In a sub-wavelength waveguide this interaction is complicated by the geometric constraints. Together the material properties and the waveguide shapes the optical mode and the resulting speed is

given by the effective refractive index. When the waveguide vibrates strain and deformation then affect the refractive index resulting in phase modulation. This is directly tied to the optomechanical forces so it will be significantly expanded upon in that section.

2.5.5 Integrated optical intensity detection

Lastly, the method used for the mass sensors in this thesis. It relies on the alignment between end-coupled cantilevers that are simultaneously optical waveguides. This type of transduction was first presented in 2006 by Zinoviev et al. [23]. When vibrations displace the sensing waveguide the alignment to the receiving waveguide changes. The oscillating alignment is then imprinted on the probe light as a modulated transmission. This will be expanded upon in the mass sensing chapter.

2.6 Actuation

The other component of transduction is the actuation. Choosing an actuator is a trade-off between force, speed and actuation length. Ultimately the fabrication limitations play a role as well. As an example, many of the options that generate a strong force have a short actuation length and therefore limiting the vibrational amplitudes that can be reached. It is also essential that the physical process is fast enough that it can operate at the resonance frequency.

2.6.1 Electrostatic

As mentioned earlier the capacitive detection scheme generates a force and by modulating the voltage over the capacitors it is possible to drive the mechanical motion. It is called the electrostatic force and arises from the Coulomb's force between the charges in the capacitors. Combined with a capacitive detection the force (eq. 2.37) can be written as,

$$\begin{aligned} F_C &= \frac{1}{2}(U_{DC} + U_{AC} \cos(\omega t))^2 \frac{\partial C(a)}{\partial a} \\ &= \frac{1}{4}(2U_{DC}^2 + U_{AC}^2 + 4U_{DC}U_{AC} \cos(\omega t) + U_{AC}^2 \cos(2\omega t)) \frac{\partial C(a)}{\partial a} \quad (2.38) \end{aligned}$$

How large the force is is dependent on the capacitor and therefore it is constrained by the same scaling laws as the capacitive detection scheme.

2.6.2 Thermoelastic

It is also possible to drive the resonance using the thermoelastic properties. Using a pulsed heating scheme the thermal expansion can excite the resonance. This

is easiest designed for by using a bi-layered resonator where the materials have two different thermal expansion coefficients. The stress gradient that forms as the temperature changes actuates the motion. It is a strong drive even if it rarely has a long range of motion. Therefore it often relies heavily on leverage.

2.6.3 Piezoelectric

Piezoelectricity is the electric charge that is generated when a material is under stress and vice versa. If such a material is integrated with the mechanical resonator then a modulated electric potential can be used to drive the resonance.

$$\varepsilon_i = C_{ij}\sigma_j + d_{ij}E_j \quad (2.39)$$

$$D_i = \epsilon_{ij}E_j + d_{ij}^T\sigma_j \quad (2.40)$$

where d_{ij} is the 3x6 piezoelectric matrix. There are several materials used in the CMOS industry like AlN, ZnO, PZT, GaN and GaAs that show piezoelectric effects. The transduction efficiency is limited by the strength of the piezoelectric tensor. Similar to the thermoelastic actuation method it is often a strong drive but the range of motion is limited.

2.6.4 Optical forces

As can be seen in Nobel prize-winning work such as last years (2018) winner optical tweezers or the optical cooling and trapping experiments that won two decades ago: light inflicts a small but very precise amount of pressure. Through clever measurement schemes and applications it is possible to do both very fundamental work in quantum mechanics and to provide the tools to capture and manipulate living cells without harming them.

A direct way to analytically approach these forces would be to through Maxwell's stress tensor. When ignoring the magnetic component that typically can be considered small in our work we can limit ourself to working with the electrostatic stress tensor. It can be written as,

$$\sigma_{ij} = \varepsilon_0 E_i E_j - \frac{1}{2} \varepsilon_0 E_i^2 \delta_{ij} \quad (2.41)$$

where ε_0 is the vacuum permittivity, E_i is the electric field in the dimension i and δ_{ij} is the Kronecker delta. In the steady state a waveguide then responds to these forces induced by the light with a deformation that is to reestablish the mechanical deformation equilibrium,

$$\nabla \cdot (\sigma_{elast} + \sigma_{elec}) = 0 \quad (2.42)$$

where the total stress in the medium, σ , is the sum of the elastic stress contribution, σ_{elast} , and the electrostatic stress tensor, σ_{elec} . The total optical force is the time-averaged integral of the divergence of Maxwell's stress tensor taken over the whole volume, V .

$$F_{opt} = \int_V \nabla \cdot \sum_{i,j} \sigma_{ij} \quad (2.43)$$

It is accurate and reliable but it offers little in the way of intuition and can often get complicated for dynamic or multispectral systems. Strictly speaking it also only covers rigid bodies. There are also many other material dependent factors that via strain induce a force such as electrostriction and thermo-optomechanics. Electrostriction, in particular, is a very relevant contributor to our work in Brillouin scattering.

A more intuitive approach to the optical forces can be found by describing the optical mode using coupled mode theory. For a lossless system the optical forces along the waveguide can then be calculated from [24],

$$F_{opt} = \frac{P_{opt}}{c} \frac{\delta n_{eff}}{\delta \tilde{u}} \quad (2.44)$$

where P_{opt} is the optical power in the waveguide, c the speed of light and $\delta n_{eff}/\delta \tilde{u}$ is the change in effective refractive index for a mechanical deformation, \tilde{u} .

A way to understand the force is to imagine a optical waveguide with light passing through it. At some point in time the waveguide is deformed causing the effective refractive index of the optical mode to increase and the speed of the light in the waveguide decreases. The delay results in a phase delay for the light leaving the waveguide, in other words a reduction of the frequency of the light and therefore the energy of the photons. That energy is lost due to mechanical work performed by the light on the waveguide during the waveguide deformation.

In many ways this is the same as that light reflected off a mirror moving away from the light source performs mechanical work on that mirror. If there is a mirror at the end of the optical waveguide the increase in effective refractive index increases the optical path length to the mirror.

2.6.4.1 Electrostriction

Since the optomechanical force depends on a mechanically induced change in the effective refractive index, many things that change the refractive index of a material can drive a vibration. The most direct one is the strain. The electrostrictive force is the force induced when the electric field interacts with elasto-optic properties of the material. A motion induces a strain which in turn changes the refractive index of the waveguide, performing mechanical work on the light.

Before calculating the magnitude of the coupling between an optical and a mechanical mode one first need to consider that the magnitude of a simulated mode is relative. As such the values need to be normalised. In the case of the mechanical amplitude this achieved by using the same normalisation we have used for the effective mass, $|u|_{\max} \equiv 1$. In the case of the optical amplitude it is achieved by normalizing to the guided optical power, $P_{opt} = \frac{1}{v_g} \langle E | \epsilon E \rangle$, where v_g is the optical group velocity and ϵ is the permittivity.

The overlap integral between the optomechanical force and motion is then,

$$\langle f_{ES}, u \rangle = \iint_A \sum_{ijkl} \frac{1}{2} n^4 E_i E_j p_{ijkl} S_{kl} dA \quad (2.45)$$

where n is the refractive index, E is the electric field in the polarization i or j , p_{ijkl} is the electrostrictive constant, S_{kl} is the strain.

The electrostrictive constants can be both positive and negative. As a result, the coupling can be low even if the strain and optical power spatially overlap. The radiation pressure, however, depends on the refractive index which for the structure to guide light must be positive.

2.6.4.2 Radiation pressure

Radiation pressure is a force acting on the refractive index interface between two materials. It is perhaps most often described as a comparison to the Doppler effect. Light bouncing off a mirror that is moving away from the light source is red shifted much the same way as if the source itself was moving away. This shift in wavelength and therefore energy is because the light performs work on that mirror. It is possible to calculate the radiation pressure, F_{rad} , from the reflected power,

$$F_{rad} = \frac{2I}{c} \cos(\theta_{ins})^2 \quad (2.46)$$

where I is the incident irradiance, θ_{ins} is the incidence angle and c the speed of light.

Many waveguides such as slot and wire waveguides guide light with total internal reflection. When light with an incidence angle steeper than the critical angle, $\theta_{crit} = \arcsin(n_{wg}/n_{clad})$, goes from a material with high refractive index, n_{wg} , to a material with lower refractive index, n_{clad} , the angle of refraction exceeds the material interface and all the light is reflected as if it hits a mirror. So light in a waveguide bounces back and forth exerting a pressure on the refractive index boundaries.

For complex geometries, such as with sub-wavelength waveguides, the pressure can be calculated from Maxwell's stress tensor. Conveniently it is possible to reduce Maxwell's stress tensor into a line integral by using Green's theorem along all the material interfaces. An overlap integral between these optical forces and

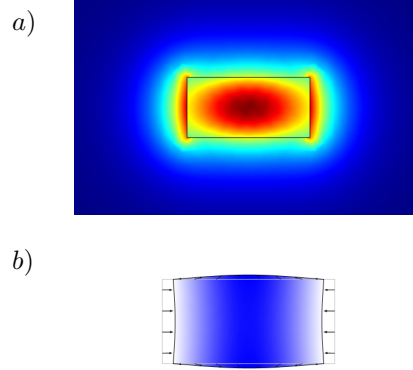


Figure 2.8: a) Optical and (b) mechanical mode of a wire waveguide. The blue color signify the volumetric strain.

the displacement (which is proportional to the velocity) of the mechanical mode gives the mechanical power, the radiation pressure coupling between the optical and mechanical mode. The calculation is complicated somewhat by the discontinuity in the electric field crossing a refractive index boundary. It has however been shown that it is preferable to use the electric displacement field instead as it is continuous [25]. The optically and mechanically normalised radiation pressure is,

$$\langle f_{RP}, u \rangle = \oint_S \frac{1}{2} \left((\epsilon_1 - \epsilon_2) E_{\parallel}^2 - (\epsilon_1^{-1} - \epsilon_2^{-1}) D_{\perp}^2 \right) (\hat{n} \cdot u) dS \quad (2.47)$$

where S is the interface between the different materials of the waveguide. \mathbf{E} and \mathbf{D} are the electric and electric displacement field. The permittivity ϵ is given on the two sides of the material interface. The subscripts \parallel and \perp denote the field parallel and orthogonal to the interface. \hat{n} is normal to the material interface pointing into material 2.

2.7 Mechanical non-linearities

This thesis has until here been a look at mechanical resonators operating at low amplitudes and therefore in the linear regime. With higher forces and quality factors the amplitude grows and results start to diverge from the linear assumptions we started with. The high amplitude solutions are important as they provide the limit to how high over the noise floor we can raise the signal.

Resonator	Mode Order	Critical Amplitude
Cantilever	1st order mode	$A_C \approx 6.3L/\sqrt{Q}$
Cantilever	2nd order mode	$A_C \approx 0.345L/\sqrt{Q}$
Fixed Beam	1st order mode	$A_C \approx 1.46W/\sqrt{Q}$
Fixed Beam	2nd order mode	$A_C \approx 1.024W/\sqrt{Q}$

Table 2.3: Critical amplitude of cantilevers and beams clamped on both sides. L is the length and W the width of the resonator.

There are many types of nonlinearities. In MEMS they can arise from material properties, from sensing or driving methods or directly from the geometric shape of the resonator. For example, beams are fixed at both ends and must extend to be able to deflect. The extension is not linear to the displacement which leads to a Duffing nonlinearity. A Duffing oscillator model includes a third order term for the stiffness and as a result the resonance frequency becomes amplitude dependent. In the fixed beam example the extra stiffness means the frequency increases. A cantilever, as much of this work has focused on, has one end free so it does not need to extend in the same way. It is, therefore, able to operate linearly at much higher amplitudes than the beam. Eventually, however, the fundamental cantilever mode experiences an increasing frequency as a geometric hardening exceeds an inertia softening nonlinearity.

As the amplitude increases and the frequency shifts even more, at a point, the shift will be so large that it forms a bistability, as illustrated in figure 2.9. At that point, the same drive forces and frequencies will converge at a different steady state amplitude depending on if the resonator started rest or at an amplitude higher than the critical amplitude, A_C . The critical amplitude due to geometric nonlinearity for a few different resonators is given in table 2.3. As can be seen from these functions the critical amplitude is limited by a high-quality factor. It has been shown that it is often preferable to increase the vibrational amplitude with a strong driving force instead of with a high quality factor if possible [26].

2.7.1 Solving the critical amplitude for a nonlinear drive and resonator

The light in the waveguide also induces a mechanical nonlinearity that modifies the critical amplitude. Analytically it can be approached in two parts, the first part is due to the continuous optical power in the waveguide and the second part is due to the modulated optical power. The force in slot waveguides has an inverse square dependence with respect to the slot width, so the continuous optical power induced nonlinearities can be treated similarly to how they have been treated in capacitively detected MEMS devices [27]. Luckily the mechanical and optical third-order nonlinearities have opposite signs, and while it does not make sense

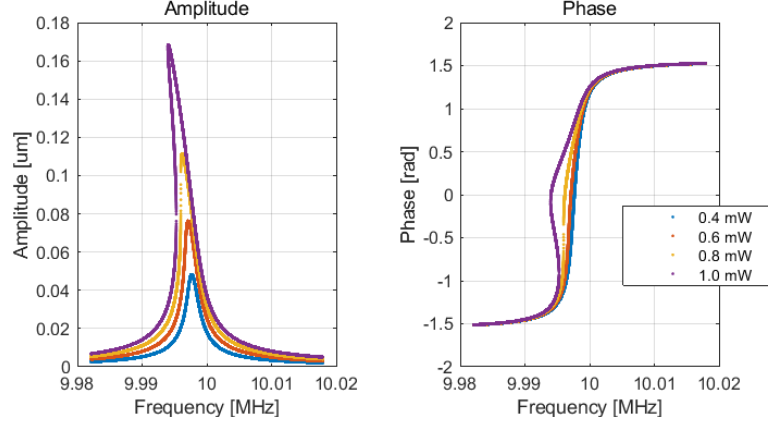


Figure 2.9: (a) is the amplitude response and (b) is the phase response of the susceptibility function of a nonlinear resonator for several different drive forces. The legend is valid for both figures. The orange line reaches the critical amplitude. The nonlinear parameters are taken from simulations of the mass sensor.

to restrict the driving force to the point where they cancel out completely it does improve the high amplitude performance. The nonlinearity due to the modulated optical power can be included in the critical amplitude by in the final step solving for the optical power needed to reach the critical amplitude instead of the amplitude. For a nonlinearity with these terms it means a small underestimation of the critical amplitude.

When including the mechanical and optical nonlinearity (up to the 3rd order) in the mechanical Langevin equations they can be written down as,

$$\begin{aligned} \ddot{a} = & -\omega_0^2 a - \Gamma \dot{a} + \frac{k_3}{m_{eff}} a^3 + P_{DC}(g_0 + g_1 a + g_2 a^2 + g_3 a^3) \\ & - P_{AC}(g_0 + g_1 a + g_2 a^2 + g_3 a^3) \cos(\omega t) \end{aligned} \quad (2.48)$$

Where P_{AC} and P_{DC} is the modulated and constant optical power in the waveguide. $g_n = \Psi_n p_n \frac{1}{m_{eff}}$ is the transduction of the higher order components of the nonlinear force onto the resonator. $\Psi_n = \frac{1}{L} \int_0^L \phi(s)^{n+1} ds$ is a lumped parameter for the mechanical mode and p_n is the n -th order Taylor expansion coefficient of the force. k_3 is the third order nonlinearity of the stiffness inherent to the cantilever shape [27]. Since the resonator is no longer linear the harmonic oscillator approximations are no longer enough. It is instead possible to derive a steady state expression for the amplitude dependent on both force and phase lag and a complimentary expression for the phase lag dependent on force and amplitude. The derivation is starting by replacing the displacement and velocity with an

in-phase, u , and an out-of-phase component, v , relative to the phase of the driving force,

$$\begin{aligned} a &= u \cos(\omega t) - v \sin(\omega t) \\ \dot{a} &= -\omega(u \sin(\omega t) + v \cos(\omega t)) \end{aligned}$$

If the function is then averaged over an oscillation and rewritten in radial components, $u = r \cos(\theta)$ & $v = r \sin(\theta)$, it gives,

$$\begin{aligned} \ddot{a}_{avr} &= -\frac{1}{8}r \left(-\Gamma\omega \cos(\theta) + (P_{DC}(4g_1 + 3g_3r^2) + 3\frac{k_3}{m_{eff}}r^2 \right. \\ &\quad \left. - 4(\omega_0^2 - \omega^2) - 2P_{AC}g_2r \cos(\theta)) \sin(\theta) \right) \end{aligned} \quad (2.49)$$

The steady state solution is found when the net acceleration over an oscillation is zero, $\ddot{a}_{avr} = 0$. In order to do so the net acceleration is expanded into r and θ terms and derived,

$$\frac{dr}{dt} = \frac{1}{8\omega} (4r\Gamma\omega - P_{AC}(4g_0 + g_2r^2) \sin(\theta)) \quad (2.50)$$

$$\begin{aligned} \frac{d\theta}{dt} &= \frac{1}{8\omega} \left((4P_{DC}g_1 + 3(P_{DC}g_3 + \frac{k_3}{m_{eff}})r^2 - 4(\omega_0^2 - \omega^2)) \right. \\ &\quad \left. - \frac{P_{AC}}{r}(4g_0 + 3g_2r^2) \cos(\theta) \right) \end{aligned} \quad (2.51)$$

Analytically the critical amplitude can be described as the lowest amplitude when $d\omega/dr = 0$ or $d\omega/d\theta = 0$ has a solution. In words it is when the phase or amplitude response no longer is unique to a drive frequency.

The steady state solution requires the time derivatives to be zero. The drive frequency can be solved for with equation 2.51 and the linear version of equation 2.50 (remove the g_2 term). Then the phase derivative is,

$$\begin{aligned} d\omega/d\theta &= \frac{1}{4\Gamma^2\omega^2} \left(-3P_{AC}^2g_0g_2\Gamma\omega \cos(2\theta) + 4\Gamma^3\omega^3 \csc(\theta)^2 \right. \\ &\quad \left. + 3P_{AC}^2g_0^2(P_{DC}g_3 + m_3) \sin(2\theta) \right) \end{aligned} \quad (2.52)$$

Using the linear equation for the amplitude introduces a small error but the signs on the nonlinear terms mean we underestimate the critical amplitude somewhat and it will just make it a conservative estimate. Equation 2.52 is possible to solve for the optical power needed to achieve critical amplitude which can be used to calculate the amplitude.

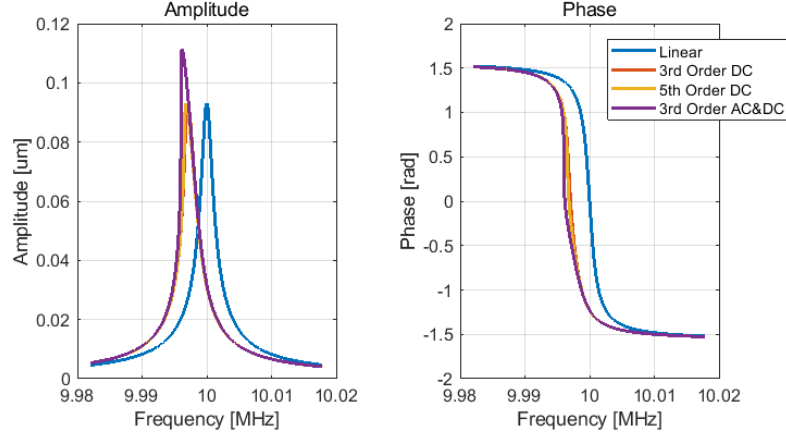


Figure 2.10: The (a) amplitude and (b) phase of the susceptibility function for resonators modeled with different orders of nonlinear constants. The P_{DC} terms includes the nonlinearities associated with continuous optical power in the waveguide. The P_{AC} terms includes the nonlinearities associated with the modulated drive force. The legend is valid for both figures.

$$r_{crit} = \frac{4\sqrt{2}}{3\sqrt{-\sqrt{3}(P_{DC}g_3 + k_3)/\omega_0\Gamma m_{eff} - g_2/g_0}} \quad (2.53)$$

P_{DC} , ω_0 , m_{eff} and Γ are the average optical power in the slot waveguide, the mechanical resonance frequency, the effective mass and the loss rate. The critical amplitude is reached with a modulated optical power of, $P_{AC,crit} = 4r_{crit}\omega_0\Gamma/(4g_0 + g_2r_{crit}^2)$, assuming it does not exceed the slot width, see Fig. 2.11.

We can also solve equation 2.50 and 2.51 to get the amplitude and phase. The derivatives of their respective steady state solution must be zero and using the Pythagorean identity, $1 = \cos(\theta)^2 + \sin(\theta)^2$, the amplitude can be rewritten as a transcendental equation,

$$P_{AC}^2 = \left(\frac{\delta\omega r}{g_0 + \frac{1}{4}g_2r^2} \right)^2 + \left(\frac{\frac{3}{4}(P_{DC}g_3 + m_3)r^3 + (P_{DC}g_1 + \omega^2 - \omega_0^2)r}{g_0 + \frac{3}{4}g_2r^2} \right)^2 \quad (2.54)$$

which can be numerically solved. By using the amplitude and equation 2.51 we can calculate the phase,

$$\theta = \arccos\left(\frac{4(P_{DC}g_1 + \omega^2 - \omega_0^2)r + 3(P_{DC}g_3 + m_3)r^3}{P_{AC}(4g_0 + 3g_2r^2)}\right) \quad (2.55)$$

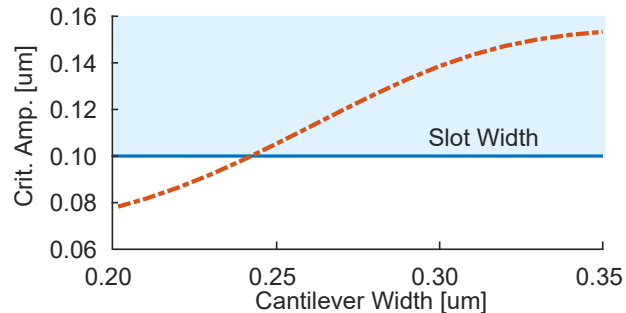


Figure 2.11: The dashed orange line shows the critical amplitude and force acting on the slot waveguide as a function of cantilever width. The critical amplitude is calculated assuming a 1 mW CW optical power in the waveguide and a 100 nm slot width. For most cantilever widths the slot is the fundamental limit to the amplitude.

The resulting amplitude and phase response can be seen in figure 2.9 and 2.10. How noise accumulate at and near the steady state solution can be solved from equation 2.50 and 2.51.

By coupling the drive force to the resonator signal it is possible to use the non-linearities to suppress the resonator noise [28]. Sadly for our mass sensor it also warps the phase response of the sensor beyond its usefulness as an indicator for mass.

2.7.2 Other optical non-linearities

Aside from the non-linearities associated with the optomechanical forces there are material related optical non-linearities. When using high optical powers they start to affect the refractive index or transmission of waveguides. Since noise is often managed by overwhelming it with a much stronger signal it is important to be able to use as much optical power as possible to drive the vibrations. Optical non-linearities are therefore one of the limits to the performance of the mechanical sensor. This problem is complicated further by that both the light driving the vibration and the light that senses the vibration share a waveguide. The drive will therefore via the non-linearity imprint on the probe. Since the signal is weak this becomes a problem at much lower powers than in most applications.

A dominant non-linear absorption channel is two-photon absorption (TPA). It is a third order process where the energy of two photons combines to excite a molecule to a higher electron state. Silicon is transparent at 1550 nm wavelength because a single photon does not have enough energy for an electron to cross the band gap. At higher powers the light-matter interaction is strong enough for two or more photons to be absorbed at virtually the same time and together they provide enough energy for the electron to make the crossing.

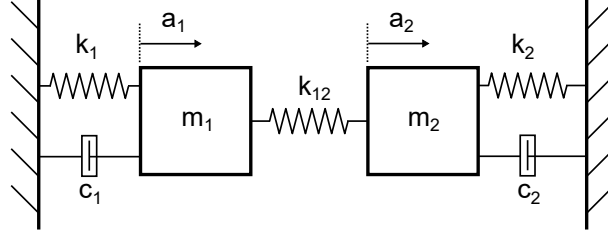


Figure 2.12: Diagram of coupled resonators. The variables signify: g and k are springs, c viscous damping and m the mass. a denotes displacement of the mass along the direction of the arrow.

The absorption is described by Beer-Lamberts law for TPA which is written,

$$I(z) = \frac{I_0}{1 + \beta z I_0} \quad (2.56)$$

where I is the intensity remaining after propagating a distance z and β is the two-photon absorption coefficient.

Kerr nonlinearity is the second order polarisation dependency of the refractive index on the optical power. Light is slowed down in a material because when it passes through it causes an oscillation to the charges of the atoms, mostly the electrons. Since moving these charges generate electromagnetic radiation, the phase delay between original optical force and the generated light interfere, leading to a slowing down of the light. The forces that confine the charges are not necessarily linear and therefore neither is the refractive index. The phenomenological mathematical description can be written,

$$n = n_0 + n_2 I \quad (2.57)$$

where n_0 and n_2 are the coefficients of a linear regression.

If the mechanical motion is detected with how it affects the transmission then the TPA will interfere with that measurement. The TPA will be in phase with the drive while the phase of the mechanical motion will depend on the difference between the drive frequency and the resonance frequency. So instead of the Gaussian peak a resonance normally looks like to a spectral measurement it will appear as a Fano resonance. Such a measurement can be seen in figure 3.23 towards the end of the next chapter. The same spectrum will occur for a phase measurement if the Kerr non-linearity is strong enough.

2.8 Coupled resonators

If two cantilevers are anchored close to each other (as they are in the mass sensor design) there is a chance that they couple mechanically this kind of coupling influences almost every single parameter of the resonator. An efficient and illustrative way to approach this is to calculate the supermodes of the coupled resonators. They can be calculated from the forces acting upon the resonators. Writing down the forces of the coupled system using the variables as drawn in figure 2.12a and rewriting $\Gamma_n = c_n/m_n$ and $\Omega_n^2 = k_n/m_n$, where n and m denotes the index of the test mass and the test mass it is connected to.

$$\begin{aligned}\ddot{a}_1 &= \Gamma_1 \dot{a}_1 - \Omega_1^2 a_1 + \frac{k_{12}}{m_1} (a_2 - a_1) \\ \ddot{a}_2 &= \Gamma_2 \dot{a}_2 - \Omega_2^2 a_2 + \frac{k_{12}}{m_2} (a_1 - a_2)\end{aligned}\quad (2.58)$$

Where a_i, \dot{a}_i and \ddot{a}_i are displacement of resonator i and its first and second time derivative. Assuming the resonators are operating at steady state amplitude means the resonator does not accelerate under the rotating frame approximation. Assuming the amplitudes are small means the harmonic oscillator assumptions are still valid and the equations can be rewritten in matrix form as,

$$\begin{bmatrix} \Omega_1^2 - \omega^2 + i\Gamma_1\omega & -\frac{k_{12}}{m_1} \\ -\frac{k_{12}}{m_2} & \Omega_2^2 - \omega^2 + i\omega\Gamma_2 \end{bmatrix} \begin{bmatrix} a_1 \\ a_2 \end{bmatrix} = \begin{bmatrix} 0 \\ 0 \end{bmatrix}$$

For a non-trivial solution to exist the determinant of the system must be zero. By finding that set of frequencies for which the determinant of the system is zero calculate the eigenfrequencies of the supermodes. To simplify the calculation we assume we are working at frequencies near the resonance, $(\Omega - \omega)^2 \ll 2\Omega\omega$, so that the system can be linearized.

$$\det \begin{vmatrix} 2\Omega_1^2 - 2\Omega_1\omega + i\Gamma_1\omega & -\frac{k_{12}}{m_1} \\ -\frac{k_{12}}{m_2} & 2\Omega_2^2 - 2\Omega_2\omega + i\omega\Gamma_2 \end{vmatrix} = 0$$

Which under the assumption that the loss rate is small compared to the frequency can be solved,

$$\omega_{\pm} = \frac{\Omega_1 + \Omega_2}{2} + i\frac{\Gamma_1 + \Gamma_2}{4} \pm \sqrt{\left(\frac{\Omega_1 - \Omega_2}{2} + i\frac{\Gamma_1 - \Gamma_2}{4}\right)^2 + \frac{K_{12}^2}{4\Omega_1\Omega_2}} \quad (2.59)$$

where ω_{\pm} are the complex frequencies of the supermodes, $\omega_{1,2}$ and $\Gamma_{1,2}$ are the resonance frequencies and loss rates of the individual cantilevers and g is the coupling coefficient. We have replaced $\frac{k_{12}^2}{m_1 m_2} = K_{12}^2$ for convenience.

From this equation it can be seen that if the coupling $K_{12}^2/4\Omega_1\Omega_2$ is small in comparison to the individual frequency splitting of the two cantilevers the coupling can be ignored in terms of its effect on the resonance frequency.

Another effect of the formation of the supermodes is that they dictate the phase relationship between the resonators. If the resonators are detuned they will transition out of the super mode and into a regular single resonator vibration. During this transition the vibration of the other resonator is gradually damped. The amplitude can be found by solving for the eigenvectors corresponding to the eigenvalues of the system.

2.8.1 Individual resonators in a coupled system

Coupled mode theory does not capture the whole dynamics of the coupled system, however. The steady state solution does very little to explain how the system responds as noise push the resonator away from the steady-state solution. First however we need to find the synchronization conditions.

We continue with the mass sensor cantilever pair as the example to work from. Depending on the the design of the anchoring it is possible to get both an elastic- and a dissipative coupling. So we can use the same variables as earlier, in equation 2.58, and need to introduce viscous coupling constant, c_{12} , acting between the same test masses as k_{12} . From those equations we can write down the forces on test mass 1,

$$F_1 = -k_1x_1 - c_1\dot{x}_1 - k_{12}(x_1 - x_2) - c_{12}(\dot{x}_1 - \dot{x}_2) \quad (2.60)$$

Make the ansatz that the oscillators can be written as $x_n = a_n e^{i\omega t}$ then the equation can be rewritten to,

$$F_1 = -k_1x_1 - i\omega_1c_1x_1 - k_{12}(x_1 - x_2) - c_{12}(i\omega_1\dot{x}_1 - i\omega_2\dot{x}_2) \quad (2.61)$$

If we want to use the Kuramoto model [29, 30] for the coupled system then the resonators and their influence on each other should be written as Hopf resonators,

$$\dot{\varphi}_n = -\Omega_n + \frac{F_n(t)}{m_n\Omega_n A_n} \cos(\varphi_n) \quad (2.62)$$

$$\dot{A}_n = -\gamma(A_n - \bar{A}_n) + \frac{F_n(t)}{m_n\Omega_n} \sin(\varphi_n) \quad (2.63)$$

φ_n and A_n are the phase and amplitude of resonator n . γ is the fractional rate with which the resonator returns to its steady state amplitude. \bar{A}_n is the steady state amplitude which often is zero. It become relevant if the resonator is driven via a feedback system, optomechanically amplified or otherwise driven into a limit cycle

operation. Include the force term from equation 2.61 and the oscillation frequency of resonator 1 becomes,

$$\dot{\varphi}_1 = -\Omega_1 + \frac{\cos(\varphi_1)}{\Omega_1 A_1 m_1} (A_2 k_{12} \cos(\varphi_2) + A_2 \Omega_2 c_{12} \sin(\varphi_2)) \quad (2.64)$$

By expanding the trigonometric products and only keeping the slow terms, i.e. $\varphi_1 - \varphi_2 = \delta\varphi_{12}$, and assuming the resonator masses are similar ($m_1 \approx m_2$) we are left with the terms the resonator is more likely to be able to follow.

$$\dot{\varphi}_1 \approx -\Omega_1 + \frac{A_2}{2\Omega_1 A_1} (K_{12} \cos(\delta\varphi_{12}) + \Omega_2 \Gamma_{12} \sin(\delta\varphi_{12})) \quad (2.65)$$

where Γ_{12} is the dissipative coupling rate, $\Gamma_{12} = c_{12}/m$.

The influence the coupling has on the phase velocity means that the resonators work as frequency modulators on each other. We can find the coupling requirements for supermodes once again when we consider the strength of the sidebands of a frequency modulated signal. The signal strength is $\propto J(\frac{K_{12}}{2\Omega\delta\varphi_{12}})$ where J is the Bessel function of the first kind, which is close to zero when $\frac{K_{12}}{2\Omega} \ll \delta\varphi_{12}$.

We then instead look at the difference in phase between the two resonators and use $\sin(\delta\varphi_{12}) = -\sin(\delta\varphi_{21})$ while $\cos(\delta\varphi_{12}) = \cos(\delta\varphi_{21})$, then the change in relative phase can be written as,

$$\delta\dot{\varphi} = -\delta\omega + C \cos \delta\varphi + D \sin \delta\varphi \quad (2.66)$$

where C and D can be approximated as,

$$C = \frac{k_{12}}{2} \left(\frac{a_1}{m_2 \Omega_2 a_2} - \frac{a_2}{m_1 \Omega_1 a_1} \right) \approx \frac{K_{12}}{2} \frac{\delta\Omega}{\Omega^2}$$

$$D = \frac{c_{12}}{2} \left(\frac{a_1 \Omega_1}{m_2 \Omega_2 a_2} + \frac{a_2 \Omega_2}{m_1 \Omega_1 a_1} \right) \approx \frac{c_{12}}{m_1}$$

if amplitude and mass are identical ($A_1 = A_2 = A$ & $m_1 = m_2 = m$) and the resonance frequencies similar ($\Omega_1 + \delta\Omega = \Omega_2$) the change in relative phase is then,

$$\delta\dot{\varphi} = -\delta\Omega \left(1 + \frac{K_{12}}{2\Omega^2} \cos(\delta\varphi) \right) + \Gamma_{12} \sin(\delta\varphi) \quad (2.67)$$

The synchronization condition ($\delta\dot{\varphi} = 0$) is then satisfied if either,

$$K_{12} \cos(\delta\varphi) > 2\Omega^2 \quad (2.68)$$

or,

$$\Gamma_{12} \sin(\delta\varphi) > \delta\omega \quad (2.69)$$

The frequency dependency in the elastic coupling term means that a very strong elastic coupling is needed before the frequency is significantly influenced. It is however not difficult to get such a coupling for the mass sensor as will be demonstrated in the next chapter.

2.9 Understanding frequency noise

The accuracy with which the resonance frequency of the sensor can be measured gives the lower limit to how accurate it is. Understanding and measuring frequency noise is therefore necessary when discussing the performance of a mass sensor.

First, in order to define frequency, noise and the other peripheral terms we start from the analytic expression of a sample signal. The instantaneous output of an oscillator at a time t can be written as,

$$V(t) = (V_0 + \varepsilon_V(t)) \cos(\Omega t + \varepsilon_\theta(t)) \quad (2.70)$$

where V_0 and Ω are the amplitude and frequency of the oscillator. $\varepsilon_V(t)$ and $\varepsilon_\theta(t)$ are the deviation from that amplitude and phase. The IEEE Standard Definitions [31] for frequency is expressed in oscillation per second. To stay consistent with the rest of the equations in the thesis these expressions have been re-expressed as radians per second.

Then the amplitude (y_{ai}), frequency (y_{fi}) and phase (y_{pi}) instability are defined as,

$$y_{ai}(t) \equiv \frac{\varepsilon_V(t)}{V_0} \quad (2.71)$$

$$y_{fi}(t) \equiv \frac{\partial \varepsilon_\theta(t) / \partial t}{\Omega} \quad (2.72)$$

$$y_{pi}(t) \equiv \frac{\varepsilon_\theta(t)}{\Omega} \quad (2.73)$$

the measurement of the frequency noise is typically not able to get to these exact parameters, however.

- In the time domain the frequency instabilities are instead derived from the two sample deviation which in this context is called the Allan variance. It is how e.g. the stability of clocks is measured. Allan variance is a statistical measurement of the variation between the phase distance travelled in two consecutive time periods and can be calculated from [31],

$$\sigma_{Allan}^2(\tau) = \frac{1}{2\tau^2} \langle (\dot{\theta}(t + \tau) - \dot{\theta}(t))^2 \rangle \quad (2.74)$$

$$= \frac{1}{2\tau^2} \langle (\theta(t + 2\tau) - 2\theta(t + \tau) + \theta(t))^2 \rangle \quad (2.75)$$

$\sigma_{Allan}(\tau)$ is the Allan deviation. $\theta(t)$ and $\dot{\theta}(t)$ are the measured phase and phase velocity at the time t . τ is the time between the measurements. In other words, the time frame for which the stability is evaluated.

- In the frequency domain the parameter used is instead the root mean squared fractional frequency deviation as a function of Fourier frequency. The instability can indirectly be accessed via the spectral density of the fractional frequency fluctuations, $S_{fi}(\omega)$, by measuring the phase noise and then calculating from there.

$$S_{fi}(\omega) = \frac{\langle y_{fi}^2(\omega) \rangle}{BW} \quad (2.76)$$

where BW is the measurement bandwidth. $S_{fi}(\omega)$ is measured in $1/Hz$. The spectral density of the frequency fluctuations can be calculated from the phase fluctuations via,

$$S_{pi}(\omega) = \frac{\Omega^2}{\omega^2} S_{fi}(\omega) \quad (2.77)$$

Finally, the standard measurement for characterising frequency and phase instabilities in the frequency domain is the phase noise, $\mathcal{L}(\omega)$, which is defined as one half of the double-sideband spectral density of phase fluctuations,

$$\mathcal{L}(\omega) \equiv S_{pi}(\omega)/2 \quad (2.78)$$

In a similar way the spectral density of the fractional amplitude fluctuations can be accessed via,

$$S_{ai}(\omega) = \frac{\langle y_{ai}^2(\omega) \rangle}{BW} \quad (2.79)$$

2.9.1 Sources of the frequency noise

The practical limit to frequency noise in MEMS and NEMS resonators is not entirely understood [32] but there are several different noise forces that contribute.

Among the suggested ones are e.g. thermomechanical fluctuations, thermal fluctuations, adsorption-desorption noise and momentum exchange noise [33].

The temperature does not only cause noise via the thermal noise force. There is also a temperature dependence to many of the material parameters. Since the resonators are designed to have as small a mass as possible they have an equally small heat capacity. Because of that temperature fluctuations can locally be rather large so the temperature dependent properties of the resonator then fluctuate with the temperature acting as another source of noise.

Adsorption-desorption noise is related to the change in surface stress and mass as the resonator absorbs particles from the surrounding gas or desorbs these particles back into the surrounding. The momentum exchange noise instead relates to the collisions with the surrounding gas molecules.

Compared to the thermomechanical noise, the direct optomechanical noise force should not be a problem as the mechanical frequency noise caused by intensity noise of even a cheap laser is several orders lower than the thermomechanical frequency noise, at our optical powers [13].

Long integration times can help reduce the SNR of the measurement but those gains are ultimately constrained by frequency drifts. Experiments have shown some success with compensating for these drifts by continuously calibrating the measured frequency drift against the drift of another mechanical mode in the same resonator [32] but this is not easily done when measuring frequency for mass sensing purposes.

Before going deeper into the phase noise discussion it is worth presenting the mass sensor so that the discussion can be given context by noise measurements.

References

- [1] Silvan Schmid, Luis Guillermo Villanueva, and Michael Lee Roukes. *Fundamentals of nanomechanical resonators*. Springer, 2016.
- [2] Anja Boisen, Søren Dohn, Stephan Sylvest Keller, Silvan Schmid, and Maria Tenje. *Cantilever-like micromechanical sensors*. Reports on Progress in Physics, 74(3):036101, 2011.
- [3] Lorenzo Pavesi, David J Lockwood, et al. *Silicon photonics iii*. Topics in Applied Physics (Springer Berlin Heidelberg, 2016), 122, 2016.
- [4] Shankar Kumar Selvaraja and Purnima Sethi. *Review on Optical Waveguides*. In Emerging Waveguide Technology. IntechOpen, 2018.
- [5] C Wolff, R Soref, CG Poulton, and BJ Eggleton. *Germanium as a material for stimulated Brillouin scattering in the mid-infrared*. Optics express, 22(25):30735–30747, 2014.
- [6] David K Biegelsen. *Photoelastic tensor of silicon and the volume dependence of the average gap*. Physical Review Letters, 32(21):1196, 1974.
- [7] Gene Simmons. *Single crystal elastic constants and calculated aggregate properties*. Technical report, Southern Methodist Univ Dallas Tex, 1965.
- [8] Christopher Baker, William Hease, Dac-Trung Nguyen, Alessio Andronico, Sara Ducci, Giuseppe Leo, and Ivan Favero. *Photoelastic coupling in gallium arsenide optomechanical disk resonators*. Optics express, 22(12):14072–14086, 2014.
- [9] Nobuo Suzuki and Kunio Tada. *Elastooptic properties of InP*. Japanese Journal of Applied Physics, 22(3R):441, 1983.
- [10] MJA Smith, BT Kuhlmeij, C Martijn de Sterke, C Wolff, M Lapine, and CG Poulton. *Metamaterial control of stimulated Brillouin scattering*. Optics letters, 41(10):2338–2341, 2016.
- [11] Allan F Bower. *Applied mechanics of solids*. CRC press, 2009.
- [12] Amnon Yariv and Pochi Yeh. *Optical waves in crystals*, volume 5. Wiley New York, 1984.
- [13] Dmitry Yu Fedyanin and Yury V Stebunov. *All-nanophotonic NEMS biosensor on a chip*. Scientific reports, 5:10968, 2015.

- [14] DM Karabacak, V Yakhot, and KL Ekinci. *High-frequency nanofluidics: An experimental study using nanomechanical resonators*. Physical review letters, 98(25):254505, 2007.
- [15] Douglas M Photiadis and John A Judge. *Attachment losses of high Q oscillators*. Applied Physics Letters, 85(3):482–484, 2004.
- [16] Amir H Safavi-Naeini, Dries Van Thourhout, Roel Baets, and Raphaël Van Laer. *Controlling phonons and photons at the wavelength-scale: silicon photonics meets silicon phononics*. arXiv preprint arXiv:1810.03217, 2018.
- [17] Benjamin J Eggleton, Christopher G Poulton, and Ravi Pant. *Inducing and harnessing stimulated Brillouin scattering in photonic integrated circuits*. Advances in Optics and Photonics, 5(4):536–587, 2013.
- [18] Jasper Chan, Amir H Safavi-Naeini, Jeff T Hill, Seán Meenehan, and Oskar Painter. *Optimized optomechanical crystal cavity with acoustic radiation shield*. Applied Physics Letters, 101(8):081115, 2012.
- [19] M Morselli. *Measuring the role of surface chemistry in silicon microphotonics*. Appl. Phys. Lett., 88:13114, 2006.
- [20] Ye Tao, Paolo Navaretti, Roland Hauert, Urs Grob, Martino Poggio, and Christian L Degen. *Permanent reduction of dissipation in nanomechanical Si resonators by chemical surface protection*. Nanotechnology, 26(46):465501, 2015.
- [21] Clarence Zener. *Internal Friction in Solids II. General Theory of Thermoelastic Internal Friction*. Phys. Rev., 53:90–99, Jan 1938.
- [22] K Kunal and NR Aluru. *Akhiezer damping in nanostructures*. Physical Review B, 84(24):245450, 2011.
- [23] Kirill Zinoviev, Carlos Dominguez, Jose Antonio Plaza, Víctor Javier Cadarso Busto, and Laura M Lechuga. *A novel optical waveguide microcantilever sensor for the detection of nanomechanical forces*. Journal of Lightwave Technology, 24(5):2132, 2006.
- [24] Peter T Rakich, Miloš A Popović, and Zheng Wang. *General treatment of optical forces and potentials in mechanically variable photonic systems*. Optics express, 17(20):18116–18135, 2009.
- [25] Steven G Johnson, Mihai Ibanescu, MA Skorobogatiy, Ori Weisberg, JD Joannopoulos, and Yoel Fink. *Perturbation theory for Maxwell's equations with shifting material boundaries*. Physical review E, 65(6):066611, 2002.

- [26] Swapan K Roy, Vincent TK Sauer, Jocelyn N Westwood-Bachman, Anandram Venkatasubramanian, and Wayne K Hiebert. *Improving mechanical sensor performance through larger damping*. *Science*, 360(6394):eaar5220, 2018.
- [27] Najib Kacem, J Arcamone, F Perez-Murano, and Sebastien Hentz. *Dynamic range enhancement of nonlinear nanomechanical resonant cantilevers for highly sensitive NEMS gas/mass sensor applications*. *Journal of Micromechanics and Microengineering*, 20(4):045023, 2010.
- [28] LG Villanueva, E Kenig, RB Karabalin, MH Matheny, Ron Lifshitz, MC Cross, and ML Roukes. *Surpassing fundamental limits of oscillators using nonlinear resonators*. *Physical review letters*, 110(17):177208, 2013.
- [29] Yoshiki Kuramoto. *Chemical oscillations, waves, and turbulence*. Courier Corporation, 2003.
- [30] Juan A Acebrón, Luis L Bonilla, Conrad J Pérez Vicente, Félix Ritort, and Renato Spigler. *The Kuramoto model: A simple paradigm for synchronization phenomena*. *Reviews of modern physics*, 77(1):137, 2005.
- [31] John R Vig et al. *IEEE standard definitions of physical quantities for fundamental frequency and time metrology-random instabilities*. *IEEE Standard*, 1139:1999, 1999.
- [32] Marc Sansa, Eric Sage, Elizabeth C Bullard, Marc Gély, Thomas Alava, Eric Colinet, Akshay K Naik, Luis Guillermo Villanueva, Laurent Duraffourg, Michael L Roukes, et al. *Frequency fluctuations in silicon nanoresonators*. *Nature nanotechnology*, 11(6):552–558, 2016.
- [33] KL Ekinici, YT Yang, and ML Roukes. *Ultimate limits to inertial mass sensing based upon nanoelectromechanical systems*. *Journal of applied physics*, 95(5):2682–2689, 2004.

3

Strong optical forces in slot waveguide mass sensor

3.1 Introduction

This chapter is focused on the design, fabrication and measurement of the mass sensor. It starts with an introduction to the parameters that qualify a mass sensor: the mass responsivity and the mass sensitivity. Following that is an exposition on the mass sensor and the considerations taken around the slot waveguide design. It also includes an investigation on a novel mass sensing design utilising the synchronisation conditions of dissipative coupling. Next is a section about the fabrication process and one about the measurement of the signal and the noise.

3.2 Mass responsivity

One of the ways to measure small masses is by measuring the resonance frequency shift as a small mass is deposited on a mechanical resonator. If the measured sample has a low Young's modulus or is deposited away from the strain of the mechanical mode the stiffness component can be ignored leaving only the mass contribution.

The perturbation function calculated earlier (equation 2.19) gives the frequency shift when a such a mass is added,

$$\omega_{shift} \approx \frac{\Omega_{old}}{2m_{eff}} m_{smp,eff}$$

where $m_{smp,eff}$ is the effective sample mass and $\omega_{shift} = \Omega_{new} - \Omega_{old}$ the frequency shift. The frequency shift per added mass is called the mass responsivity and is often denoted R , ($= \frac{\Omega_{old}}{2m_{eff}}$). One of the keywords here is *effective* mass as the response depends on where along the resonator the mass is deposited. As a result, the frequency shift of a point mass on a cantilever is going to be,

$$\omega_{shift,n} \approx \frac{\Omega_n}{2m_{eff,n}} \phi_n^2(x) m_{smp} \quad (3.1)$$

and in reverse, calculating the mass from the frequency shift,

$$m_{sample} \approx \frac{2m_{eff,n}}{\phi_n^2(x)} \frac{\omega_{shift,n}}{\Omega_n} \quad (3.2)$$

In many cases, the deposited mass will instead be distributed as a thin layer coating the whole surface of the resonator. If the coating does not contribute to the stiffness then the frequency shift will be,

$$\omega_{shift,n} \approx \frac{\Omega_n m_{coat}}{2m_{eff,n}} \left(WH \phi_n^2(L) + 2(W + H) \int_0^L \phi_n^2(x) dx \right) \quad (3.3)$$

where m_{coat} is the added mass per surface area. L , H and W are the length, thickness and width of the cantilever.

For the first order mode the shift is,

$$\omega_{shift,1} \approx \frac{\Omega_n m_{coat}}{2m_{eff,1}} \left(WH + (W + H) \frac{L}{2} \right) \quad (3.4)$$

3.2.1 Sensitivity to sample distribution

When the deposition method does not accurately position the sample it becomes a factor of uncertainty to the mass measurement. However, the position dependency is mode dependent so by measuring the frequency shift of several modes it can also be used for a position determination. If the sample is placed close to the tip it is possible to use the measured resonance frequency shift and the simulated effective mass to calculate the positions of the sample mass,

$$\sqrt{\frac{\Omega_m \omega_{shift,n}}{\Omega_n \omega_{shift,m}}} = \frac{\phi_n(x)}{\phi_m(x)} \quad (3.5)$$

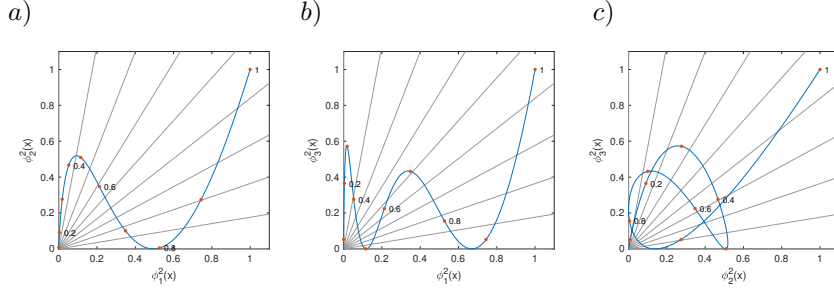


Figure 3.1: The figure is showing the effective mass contribution, $\phi_n^2(x)$, for different mode order, n , against each other. The orange dots mark 10% percentiles of the cantilever length. The radial grey lines act as a visual guide for the fractions $\phi_n^2(x)/\phi_m^2(x)$.

For positions further away from the cantilever tip fitting the results against more modes is needed for extracting the position. This is to avoid degenerate results, seen in figure 3.1 as the same grey line crossing the blue line twice.

Using the same line of thinking it is possible to measure several of the modes and use that information to make the measurement position independent [1]. The difference between the mode shapes makes it so that it is possible to find a linear combination of the modes that together give a position independent response, see figure 3.2.

The coefficients for the linear combination are found by fitting the mode shapes against a unitary response. The best results are seen if the possible sample positions are limited to only a part of the cantilever. The same limits can in practice be imposed on the mass sensor by coating this part of the cantilever with a selective coating.

3.2.2 Mass sensitivity

The mass responsivity is not the only important parameter of a mass sensor. There is also the mass resolution, the accuracy with which the sensor operates. A mass measurement is calculated from the frequency shift by using the mass responsivity. Thus noise in the mass measurement can be written as [2],

$$\delta m_{min} \approx R^{-1} \sigma_{\Omega} \quad (3.6)$$

where R is the mass responsivity and σ_{Ω} is the frequency noise.

The frequency noise is however also influenced by the measurement technique. A typical scheme for a frequency measurement is a phase-locked loop (PLL). It drives the resonator with a voltage-controlled oscillator (VCO). The phase of the response signal from the resonator depends on the difference between the drive frequency and the resonance frequency. A fraction of the drive signal is split off

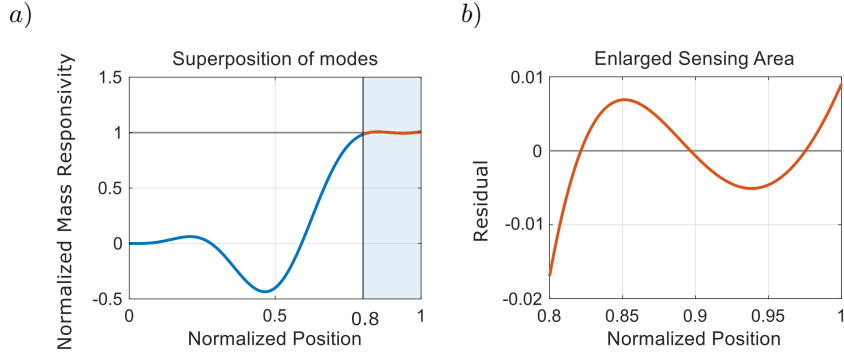


Figure 3.2: a) Normalized mass responsivity of a superposition of the first three orders of modes. The superposition is optimized for the top 20% of the cantilever (the blue region). b) Enlarged view of the optimized area.

and combined with the response signal in an RF mixer. The resulting DC component is proportional to the phase difference between the two signals. The DC component is fed back into the VCO to adjust the drive frequency. A controllable phase delay on the split-off drive signal makes it possible to tune the feedback so it is centred at the resonance.

In such a situation the smallest measurable effective mass can be written as,

$$\delta m_{min} \approx 2m_{eff}10^{-DR/20} \sqrt{\frac{\Delta f}{Q\Omega_0}} \quad (3.7)$$

where δm_{min} is the smallest measurable effective mass. Δf is the bandwidth of the PLL circuit. DR is the signal to noise ratio expressed in decibel.

For only thermomechanical noise the SNR is $DR = 10 \log_{10}(E_c/E_{th})$, where $E_{th} = \frac{1}{2}k_B T$ and $E_c = \frac{1}{2}m_{eff}\Omega_0^2 \langle a \rangle^2$ the thermal and kinetic energy of the resonator.

3.3 Designing the mass sensor

The initial motivation of this mass sensor design is to use the strong optomechanical force that is generated in slot waveguides to reduce the frequency noise and thereby improve the mass sensitivity of a cantilever mass sensor. The design of the slot waveguide itself is guided by fabrication tolerances, optimisation of forces and displacement sensitivity. This however leaves some freedom when it comes to the design of the anchoring of these slot waveguide cantilevers. By coupling to the waveguide using a multimode interferometer (MMI) it is possible to define the cantilever length in one fabrication step. The MMI forms a very rigid base for the cantilevers which helps reduce the clamping losses. A schematic of the sensor



Figure 3.3: Mechanical supermodes of the cantilever pair. The colors signify the volumetric strain.

design is shown in figure 3.8.

There is however an inevitable coupling between the two cantilevers that makes the slot, both through the anchoring but also optomechanically. As a result they will form a symmetric and asymmetric pair of supermodes, as shown in figure 3.3. Since both cantilevers move this will, in turn, modify the mass responsivity as described in equation 2.59.

3.3.1 Measuring the coupling between the cantilevers

Designing the mechanical coupling between the two cantilevers is possible. By either cutting the slot further into or stopping the slot before it cuts into the MMI it is possible to control the elastic and the dissipative coupling, see the figures 3.4 a and b. Increasing δ_{stem} enhances the coupling between the two cantilevers and the shared section improves the destructive interference of the clamping losses radiating into the substrate. Simulations show that as long as the two cantilevers are perfectly identical it is possible to effectively eliminate the clamping losses.

Notable is that in the figure 3.4b there is mode crossing at $\delta_{stem} = 220$ nm. Here the elastic coupling disappears and only the dissipative coupling remains.

This dynamic can be captured analytically by considering the two cantilevers anchored to a base resonator instead of a fixed substrate and that they are elastically coupled. That these two couplings have opposite signs.

As a platform for cantilevers it is possible to design for a strongly coupled tuning fork or independent cantilevers.

To minimise the added complications of the coupling one of the cantilevers has been shortened by 100 nm, δ_{as} , to detune its frequency. This corresponds to a measured change of the resonance frequency by 440 kHz for a 6 μm cantilever as compared to the measured 38 kHz coupling induced splitting measured in a pair designed to be identical in length. It is possible to detune the cantilevers further by either making one cantilever thinner or by shortening it further. The measured frequency splitting is compared with the simulated splitting in figure 3.5. A sample

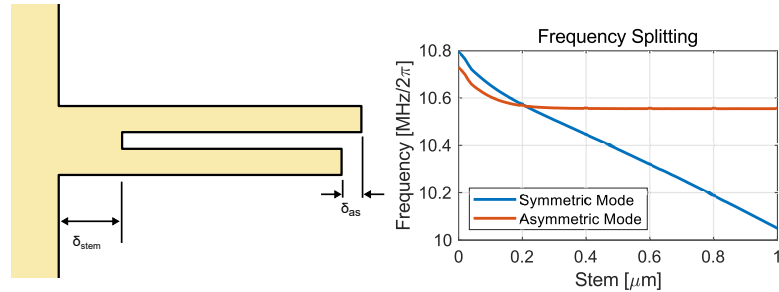


Figure 3.4: a) Schematic for designing the coupling between the cantilevers. b) The resulting frequency splitting from tuning δ_{stem} .

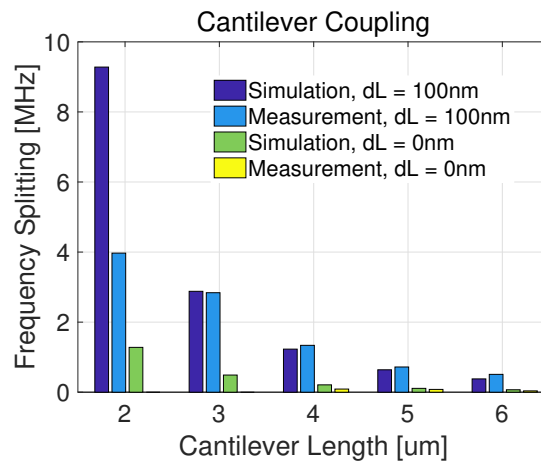


Figure 3.5: Mode splitting for the mass sensor cantilever pair described in the next chapter. The cantilevers are of equal and unequal length, unequal meaning one of them is 100 nm shorter than the other. The 2 and 3 μ m equal length measurements are not available since the signal is too low.

spectrum is provided in figure 3.6. The results match well except for the 2 μ m cantilever pair.

3.3.2 Dissipatively coupled resonators as mass sensors

There are suggested tuning fork mass sensor designs relying on measuring how an added mass spoils their high-quality factor [3]. By detuning one of the prongs they are driven out of phase and the tuning fork mode partially breaks down. The anchoring losses no longer destructively interfere and the clamping losses increase. However, the measurement strategy changes from a phase response measurement to an amplitude measurement and under normal operation amplitude noise does not

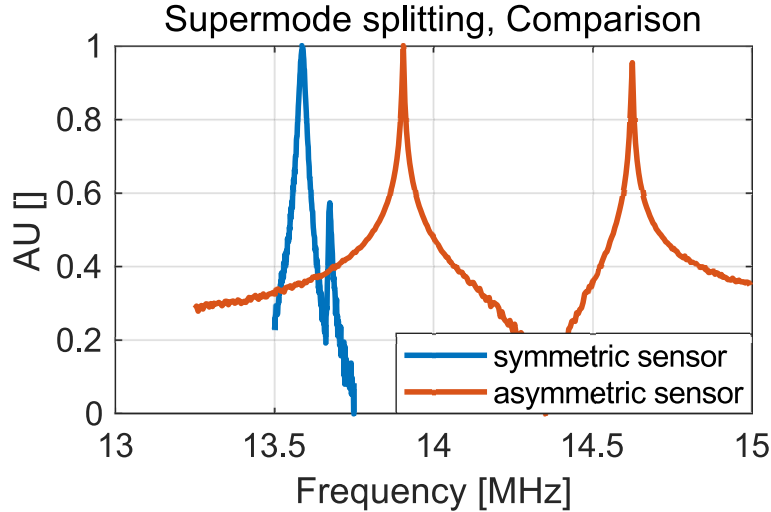


Figure 3.6: The RF spectrum of two mass sensors. In one of the cantilever pair one of the cantilevers has been shortened by 100 nm. The difference in signal is largely due to a difference in input optical power.

decrease with amplitude. It is therefore not clear that this method is advantageous.

It is possible to design a purely dissipative coupling and we have derived the dissipative synchronization requirements, equation (2.69). It shows a phase difference and loss rate [4] that is frequency difference dependent and it is worth discussing if this phase difference is a suitable mass sensing mechanism. The phase difference,

$$\sin(\delta\varphi_{synch}) = \frac{\delta\omega}{\Gamma_c} \quad (3.8)$$

$\delta\varphi_{synch}$ is a stable equilibrium state since the force that maintains the phase difference is weaker the smaller the phase difference is while the difference in resonance frequency drives the phase apart.

By simulating two dissipatively coupled resonators it is possible to estimate how the individual frequency noise impacts the relative phase difference. The phase velocity of the resonators can be described with a Hopf model for the resonators, as described in equation 2.63, driven by the thermomechanical noise force, $F_{th}(\omega) = \sqrt{4k_B T c}$. The derivation of the force can be found in the thermal calibration chapter. With that the evolution of amplitude and phase can be simulated, in our case by using python. The results are shown in figure 3.7.

As it turns out the mass sensitivity of the synchronised sensor is worse than that of an individual cantilever. The phase difference takes a while to stabilise at the equilibrium. Therefore the phase difference is not indicative of the equilibrium

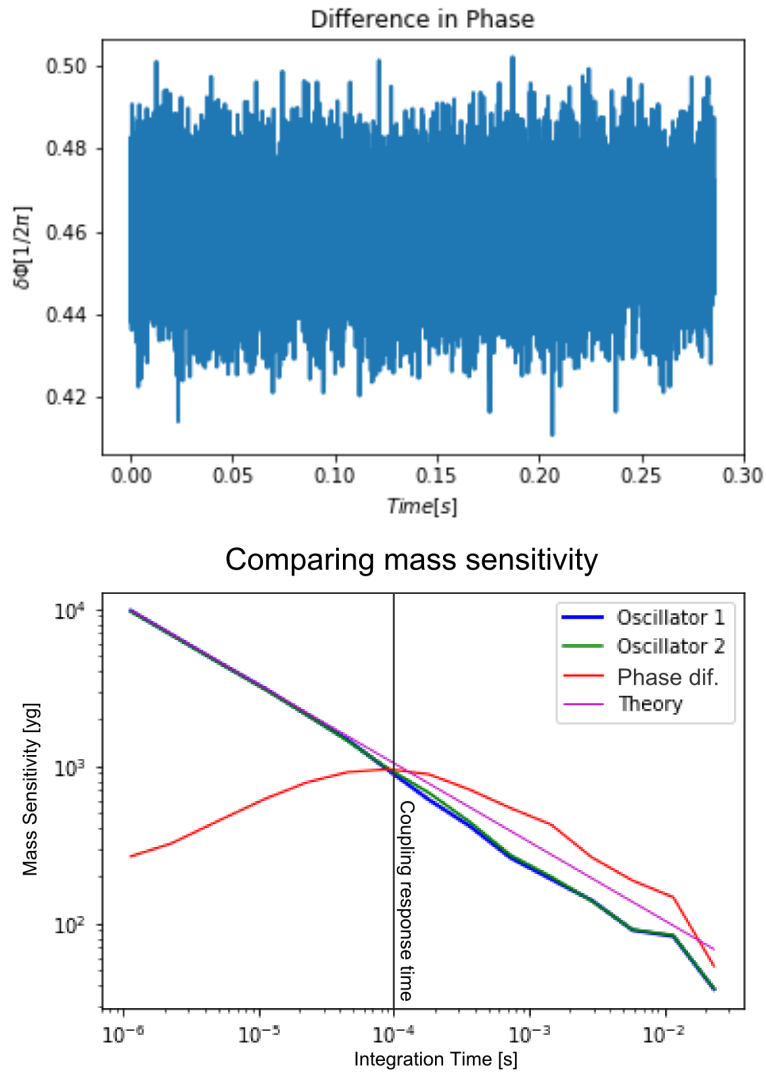


Figure 3.7: a) Simulations of the phase difference between the two prongs. b) Mass sensitivity as a function of integration time. The two prongs double in effective mass as the coupling mediates the synchronisation ($(\Gamma_{12})^{-1} = 10^{-4}$ s). The improvement in noise level is counteracted by the increase in mass.

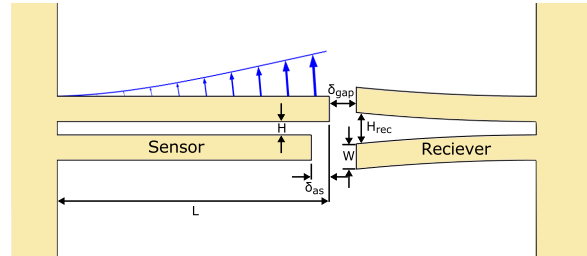


Figure 3.8: Drawing of the mass sensor cantilevers with the purpose of naming the dimensions of each component. The blue line and arrows shows the first order mechanical mode of the cantilever.

for time frames shorter than the stabilisation time. For time frames longer than the stabilisation time it is instead noisier than an individual cantilever. The individual prongs of the synchronised system do have less phase noise but since they are synchronised they act as if they combine their effective mass. By doubling the effective mass the mass responsivity is halved and the mass sensitivity reduced. The reduction in phase noise has been demonstrated before in optomechanically synchronised systems [5].

3.3.3 Slot waveguides for optomechanics

A slot waveguide is a waveguide that guides the light in the subwavelength low refractive index slot in between two high refractive index slabs. The high refractive index slabs constrain the optical mode in the slot. Maxwell's equations state that the electric displacement field must be continuous, so the difference in the electric field on the two sides of the interface is proportional to the difference in permittivity. The mode is shown in figure 3.9.

3.3.3.1 Optomechanical forces in slot waveguides

In the same way as to how a high refractive index particle is driven towards higher optical intensity in an optical tweezer, a waveguide is pushed towards the shape that maximises the effective refractive index of the mode. As such the light in a slot waveguide forces the high refractive index slabs together into their highest refractive index form, a waveguide with twice the slab width.

The effective refractive index of a slot waveguide goes from consisting of one alone of the silicon slabs to, as they get closer to each other and start to interact,

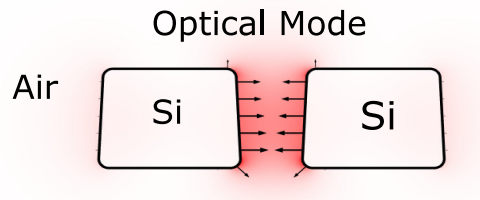


Figure 3.9: Optical mode in slot waveguide (the electric field is displayed in red). The black arrows radiating from the interface show the direction and relative magnitude of the local force contribution in accordance with the perturbation theory used to calculate the radiation pressure.

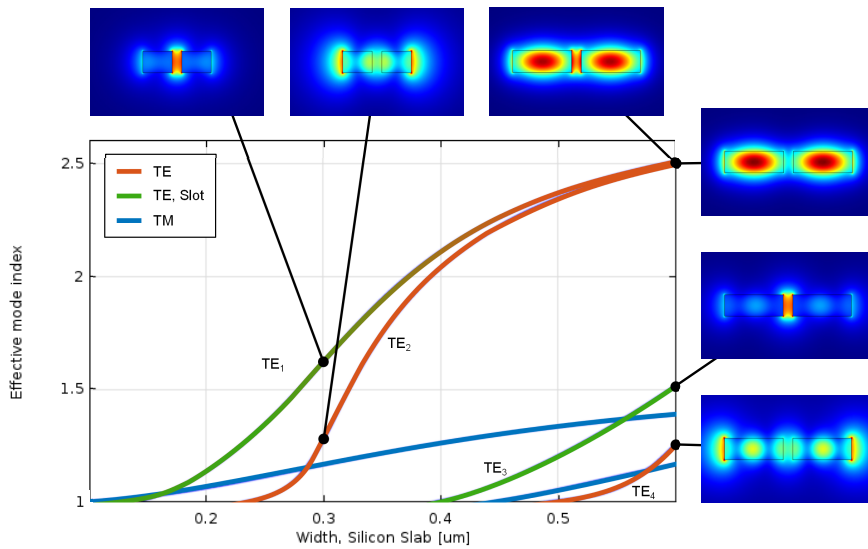


Figure 3.10: Effective refractive index as it depends on the width of the silicon slab. As the slot waveguide grows wider the slot mode (TE_1) transitions into a symmetric supermode like the one in a directional coupler. Around that point another slot mode (TE_3) can be guided.

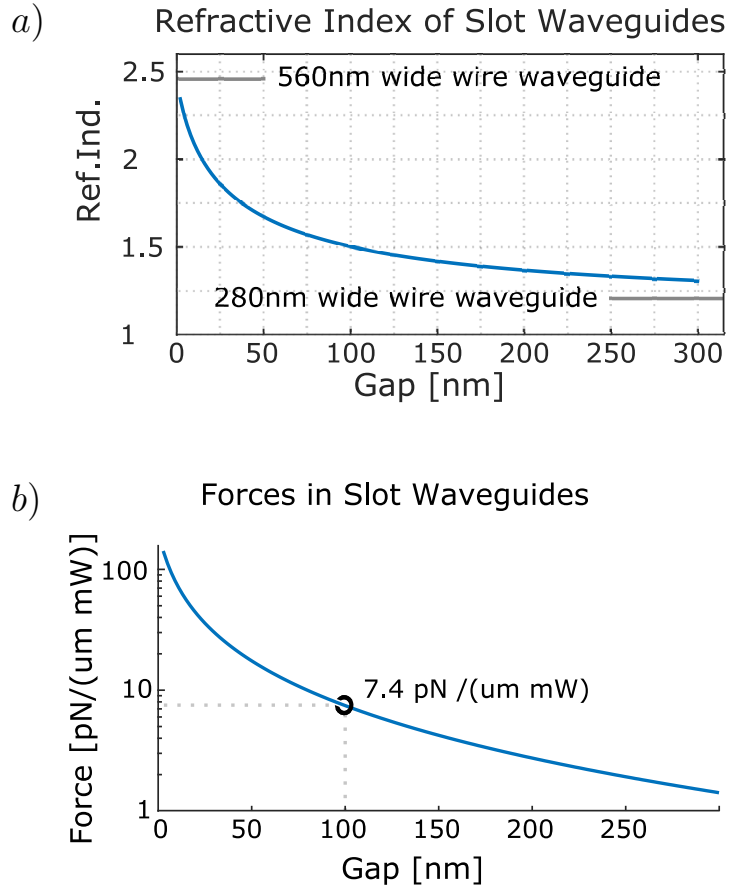


Figure 3.11: (a) The refractive index and (b) optical forces in a slot waveguide.

ultimately form a wire waveguide with the combined width of both slabs, see figure 3.11 (a). The transition becomes very sharp as the slot closes. Using equation (2.44) the forces can be calculated.

Simulations show that for a wider slot the refractive index is exponentially dependent on the slot width. When the slot is narrower, the second beam can no longer be treated as a perturbation of the field around the first beam. In that case, the force dependence on slot width, seen in figure 3.11, shows very good correspondence to the inverse of a second order polynomial. Fitted to the force simulated for the slot waveguide in the mass sensor it gives $p_{fit}(h) = P_{opt}L/(6.72 + 7.3710^8h + 5.2910^{15}h^2)$, where h is the slot width.

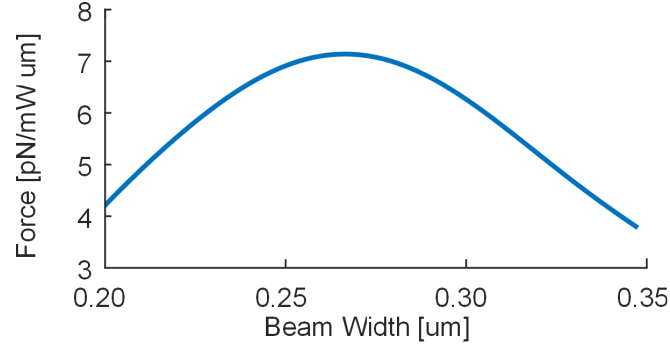


Figure 3.12: The force as a function of the width of the silicon slabs in the slot waveguide.

3.3.4 Designing the slot

The force in a slot waveguide is not only dependent on the width of the slot but also the width of the silicon slabs. A simulation of the force as a function of the silicon width can be seen in figure 3.12 starting from 200 nm, which is the cut-off for single mode operation, and expanding until 350 nm where the silicon is wide enough to guide the light in itself. The maximum force is found at 280 nm, near the maximum of the mode splitting found in figure 3.10. How far thinking about the force as a consequence of the mode splitting can be taken is uncertain; since the other mode (TE_2) is barely guided at this width.

The slot waveguide design puts some very strict demands on the cantilever cross-section. These constraints can be lessened somewhat by allowing for an asymmetric slot design. While the force is maximised for the symmetric case, as can be seen in figure 3.13, it is worth considering the mechanical benefits of using a narrower cantilever.

A narrower cantilever is lighter and softer with a lower resonance frequency. The mass responsivity is relative to the cantilever effective mass. Also, the mass sensitivity should improve if the other parameters such as quality factor stay the same. It was not fabricated however due to the waveguide parameters already being close to the lithographic limits. Simulations show that the displacement sensitivity is worse for a narrower cantilever.

3.3.5 Optical stiffness and damping

The mechanical resonance frequency depends on the effective mass and stiffness of the resonator ($\Omega = \sqrt{\frac{k_{eff}}{m_{eff}}}$). Since the optical force is dependent on the width of the slot, see figure 3.11, it acts as an optical spring and must often be included in the resonance frequency calculation,

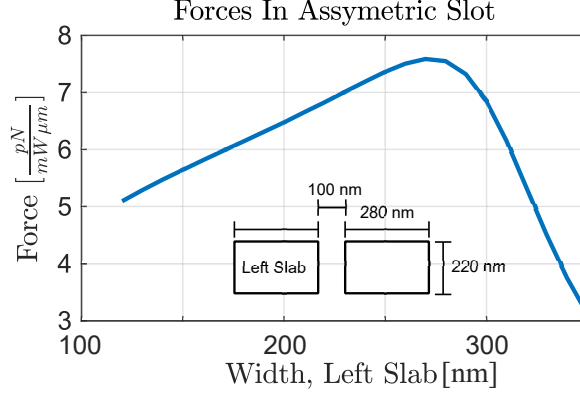


Figure 3.13: The forces in an asymmetric slot waveguide in silicon for the waveguide dimensions given in the plot.

$$\Omega'_n = \sqrt{\frac{k_{eff,n} + g_{1,n}P_{DC}}{m_{eff,n}}} \quad (3.9)$$

where $g_{1,n}$ is the transduction of the first order component of the nonlinear force as described in the nonlinearities section. P_{DC} is the continuous optical power in the waveguide. For softer resonators, it can be a quite substantial part of the stiffness but for MHz MEMS structures it can often be treated as a perturbation. Since the optical force from the mechanical perspective is lossless it is possible to dilute the strain associated losses in the resonator and increase the quality factor.

Another way the optical force influences the mechanical amplitude is via the second order derivative of the force. At resonance, the optical force driving the vibration is in phase with the force damping the vibration and will look as if it effectively modifies the damping. A word of warning here is that this term is due to what is effectively an increase in the driving force and does not replace the losses from the mechanical strain. It does therefore not shield the resonator from thermal noise which leads it to be called effective damping [6]. Whether the optical force is increasing or decreasing the damping depends on the sign of the second derivative. The new amplitude at resonance is,

$$a = \frac{P_{AC}(g_0 + \frac{1}{4}g_2a^2)}{\Gamma\omega} \quad (3.10)$$

3.3.6 Displacement sensitivity

We are detecting the vibrations in the sensor by how they affect the transmission between the sensor slot and the receiver slot. The displacement sensitivity for a

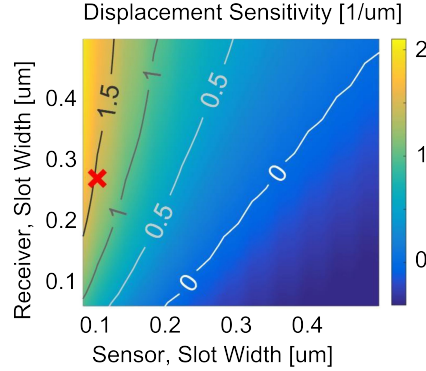


Figure 3.14: The displacement sensitivity of the transmitting slot mapped as a function of the two slot widths. The red cross marks the point we are operating at.

span of different sensing and receiving slot widths is simulated using FDTD and the results are shown in figure 3.14.

It shows that the sensitivity is better for a narrow sensor slot and a wider receiver slot. This is because vibrations are larger proportionally to a narrow sensor slot. We arrived at using a sensing slot width of 100 nm and a receiving slot width of 280 nm as a compromise between overall transmission and displacement sensitivity. The result is a simulated sensitivity of $1.2 \mu\text{m}^{-1}$ as relative to incoming light. The receiving slot is then quickly tapered down to 100 nm to minimise the reflection and losses. Since one of the prongs is shortened to break the tuning fork supermodes the displacement sensitivity is affected, it is reduced by -0.2 dB.

3.3.7 Thermal calibration

The displacement sensitivity is directly measured by exciting the resonator to a known amplitude and then measuring the resulting signal. The difficult part is often to know the amplitude of the vibration. It is therefore convenient that the sensor is sensitive enough to measure the thermal vibrations [7] as the energy of those vibrations is dependent only on temperature.

If the resonator is at thermal equilibrium then the thermal energy of anyone of the vibrational modes is $E_{th} = \frac{1}{2}k_B T$. k_B and T are Boltzmann's constant and the temperature of the resonator. The equipartition theorem then says that the energy of the mechanical vibrations is equal to the thermal energy of the mode so,

$$\frac{1}{2}k_B T = \frac{1}{2}k_{eff}\langle a^2 \rangle = \frac{1}{2}m_{eff}\langle \dot{a}^2 \rangle \quad (3.11)$$

Under these conditions, the fluctuation-dissipation theorem links the viscous damping force, c , to the thermomechanical noise force, f_{th} , resulting in noise

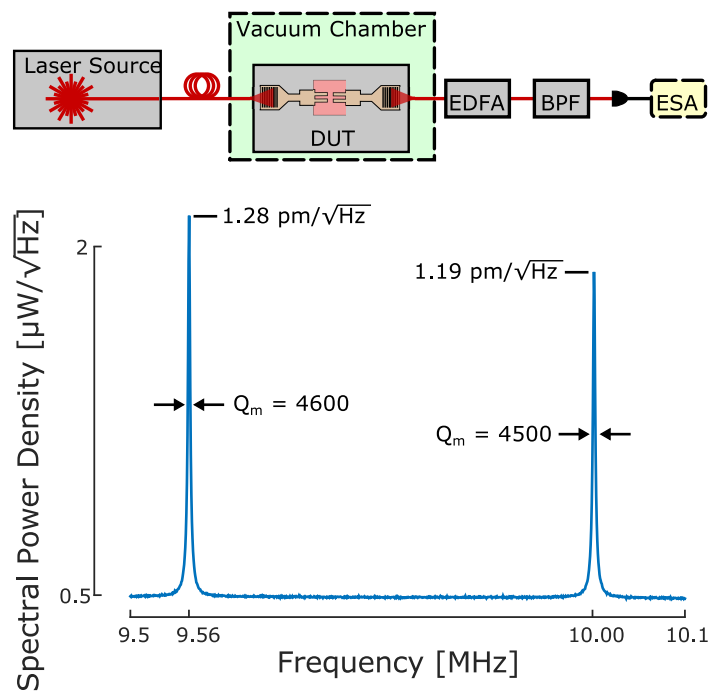


Figure 3.15: Setup and measurement of the thermal vibrations of the cantilever. By comparing with the expected thermal amplitude marked in the figure it is possible to verify the displacement sensitivity.

force power spectral density of,

$$F_{th}^2(\omega) = 4k_B T c \quad (3.12)$$

The thermal noise force is incoherent but with long integration time the expectation value of the amplitude can be measured. The resonance frequency and quality factor can be extracted from the same measurement and effective masses can be effectively simulated. With those parameters it is possible to calculate the amplitude of the thermomechanical noise at resonance,

$$S_{1/2} = \sqrt{\frac{4k_B T Q}{\Omega^3 m_{eff}}} \quad (3.13)$$

By doing an optical transmission measurement¹ on the mass sensor and then extracting the optical RF signal using a photodiode and an ESA, results shown in figure 3.15, we extract the displacement sensitivity of a sensor. In order to amplify the weak signal we do the measurement in vacuum to avoid air damping and then post-amplify the optical signal with an EDFA before it reaches the diode.

We couple in and out of the chip vertically using fibre and grating couplers [8], losing 5.5 dB at each instance. The insertion loss of the device accounts for the remaining 3 dB that is lost over the device. The device as well as the fibres used for coupling in and out of the chip are placed in a vacuum chamber evacuated below 10^{-2} mbar for each measurement. The thermomechanical noise is measured at 1563 nm with a transmission measurement using a high-speed photodiode connected to an electric spectrum analyser (ESA). Measurements of the two cantilevers, 6 and 5.9 μm long, show a resonance frequency of 9.56 and 10.0 MHz and a quality factor of 4500 and 4600. The results can be seen in Figure 3.15. The 9.56 MHz resonance is measured to be $2.13 \text{ mW}/\sqrt{\text{Hz}}$ which is calculated to have a thermal amplitude of $1.28 \text{ pm}/\sqrt{\text{Hz}}$. The measured values compare well with the simulated value of the displacement sensitivity. Figure 3.16 shows the displacement sensitivity measured over a wavelength span of 30 nm.

3.4 Optical Circuit

Aside from the mass sensor the design has been kept as simple as possible. Only two other components are present in the circuit: grating couplers to couple light to and from the chip and two MMIs to give a good base for the mass sensor.

There are a few ways to couple light into an optical circuit, e.g. tapers and grating couplers. We have been working with grating couplers because they allow

¹The measurements have been performed with a Syntune S7500 tunable laser, a Finisar 1000S Waveshaper, an HP Lightwave 70810B high-speed photodiode and a Keysight N9010A EXA Signal Analyzer. The EDFA used is of type Keopsys CEFA-C-HG.

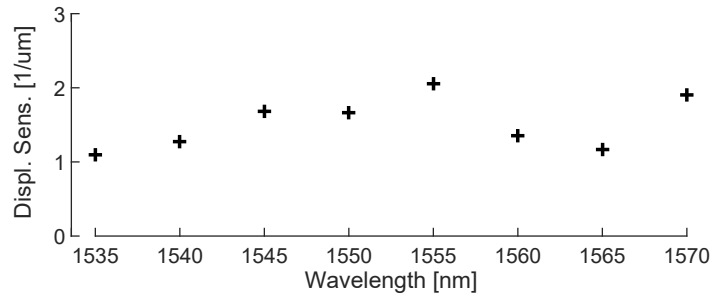


Figure 3.16: Shows the displacement sensitivity over a spectrum of wavelengths calculated from the amplitude of the thermal spectrum. The displacement sensitivity relative to the power leaving the sensor.

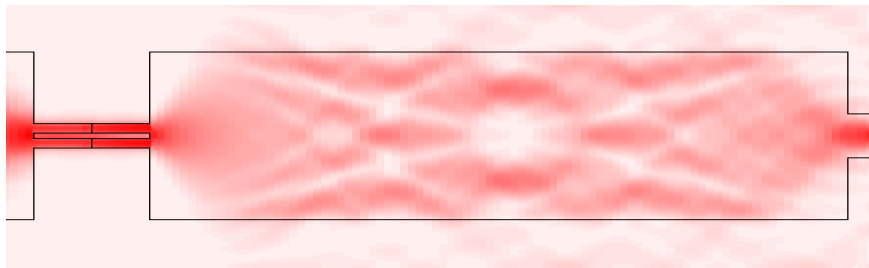


Figure 3.17: MMI coupling light from wire waveguide to slot mass sensor.

us to couple into the silicon from above which is very convenient when working with many devices on the same chip. It is a wavelength and polarisation dependent device that in its totality is beyond the scope of this PhD but there are plenty of sources to be found expanding on the subject [9]. A grating coupler is a periodic grating etched into the silicon that scatters the light to an angle which can be confined by total internal reflection. The light is then focused into a waveguide with which it is routed to the MMI.

An MMI is a kind of waveguide combiner, mixer or splitter. Light from an incoming waveguide excites a combination of the spatial modes in a much broader waveguide. The modes then propagate at different speeds in accordance with their respective effective refractive indexes. As they propagate they form an evolving combination of interference patterns which at points is dominated by higher order modes, see figure 3.17. By terminating the broad waveguide at one of these points it is possible to efficiently divide the light between different waveguides by butt-coupling waveguides to the positions of high field intensity.

After propagating in the MMI for a distance the modes reform the initial phase conditions and light is once again focused in the same pattern it entered the MMI. This makes it possible to design a 1 to 1 coupler such as the one we have used in

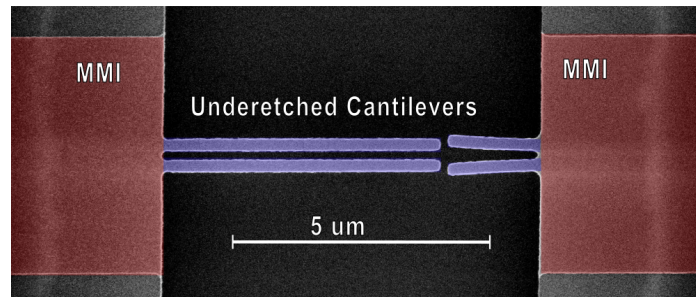


Figure 3.18: A SEM picture of the mass sensor. MMI has been shaded red and the cantilevers have been shaded purple.

the mass sensor.

Since the MMI can be designed as a splitter it is also possible to couple to more than one sensor at once. By multiplexing several mass sensors they form a sensor array with a very small footprint [10].

Typically the coupling efficiency depends on how well the original mode can be decomposed into the MMI modes but since we are terminating the MMI with a slot waveguide it is not obvious that the coupling will be good. Using an optical mode solver, FIMMWAVE, we simulate to coupling efficiency to be 90% for a slightly shortened 1 to 1 MMI. Simulating an MMI using a mode solver is preferable to using an FDTD solver as it is much faster for this kind of problems. The measured losses over the whole device once the grating coupler losses are accounted for is about 3 dB.

3.5 Fabrication

The fabrication of the mass sensor has been kept as simple as possible. It was patterned in a 220 nm thick silicon layer on top a 2 μm silicon oxide (SOI) using 193 nm UV lithography via the multi-project wafer (MPW) service provided by IMEC (www.ePIXfab.eu). The under-etching has been done in the cleanroom of the photonics research group in Ghent.

3.5.1 Optical proximity correction

Just as the Rayleigh criterion set a limit to what can be optically resolved it is also a limit to the smallest area of resist that can be exposed. The size and depth of the focus in the lithographic stepper set the limit to the smallest features that can be patterned called the critical dimension, CD .

When designing close to this limit there is a proximity effect to take into account. Photoresist degrades at a critical exposure level and the exposure power is

calibrated for that. Nearby features on the photomask diffract, however, scattering light into the border region between degraded and non-degraded resist, affecting the exposure level and moving that border. The results are that areas of the mask where there is much detail are more difficult to design. By being aware of the complications it is possible to compensate for them somewhat.

Simulations show that the anchoring losses decrease when the anchor corner is sharp. The rounding act like a taper for the mechanical impedance mismatch and by doing so reduces the reflection. Small changes in the anchor design also have a large impact on the coupling between the two cantilevers in the sensor. Designing a cut in the corner of the silicon layer, see figure 3.19, results in a sharper corner in the fabricated design. SEM images of the fabricated cantilevers: a reference without cut and a pair of cuts 30 nm and 60 nm show that the radius of the corner is reduced from 91 nm to 85 nm and 76 nm. The rounding of the corners at the inside of the slot fills up the slot for 80 nm, as can be seen in figure 3.19a. The largest cut manages to start at the MMI but it is beginning to dig into the width of the cantilever. Measurements show that the losses is not reliably decreased but that can be expected as the surface losses are even larger.

3.5.2 Under-etching

The SOI material stack puts the optical silicon layer on top of silicon oxide. So for a silicon resonator to be free to vibrate the oxide needs to be removed. One way of doing so is by etching away the oxide with hydrofluoric acid (HF).

HF is a dangerous liquid but it provides good selectivity for oxide relative to silicon. The etching speed for oxide varies with the type and quality of oxide but the silicon is virtually untouched short of the thin native oxide layer formed at the silicon-air interface.

To protect the oxide on the chip that is not supposed to be etched is protected by a layer of photoresist. The resist is deposited, patterned and developed to form an HF-resistant mask covering these areas while leaving the area that is supposed to be etched exposed to the etchant, see figure 3.20. It is important to keep in mind that the mask will also be under-etched, often at a higher etch rate than the oxide itself. The etch rate is also usually higher along waveguides and similar long structures. In our case the etching was done with a buffered etchant (HF:NH₄F = 12.5 : 87.5%) and the photoresist used was TI 35E from micro chemicals. Development of the resist is done with AZ-400 from the same company.

To minimise the manual errors and avoid over-etching it is often preferable to use a partial etch step to define the silicon devices in the initial design. The remaining silicon works as a good etch mask and should the structure still be under-etched it will support the structure. The shared fabrication that comes with using an MPW, however, makes it so you still can not get rid of using photoresist com-

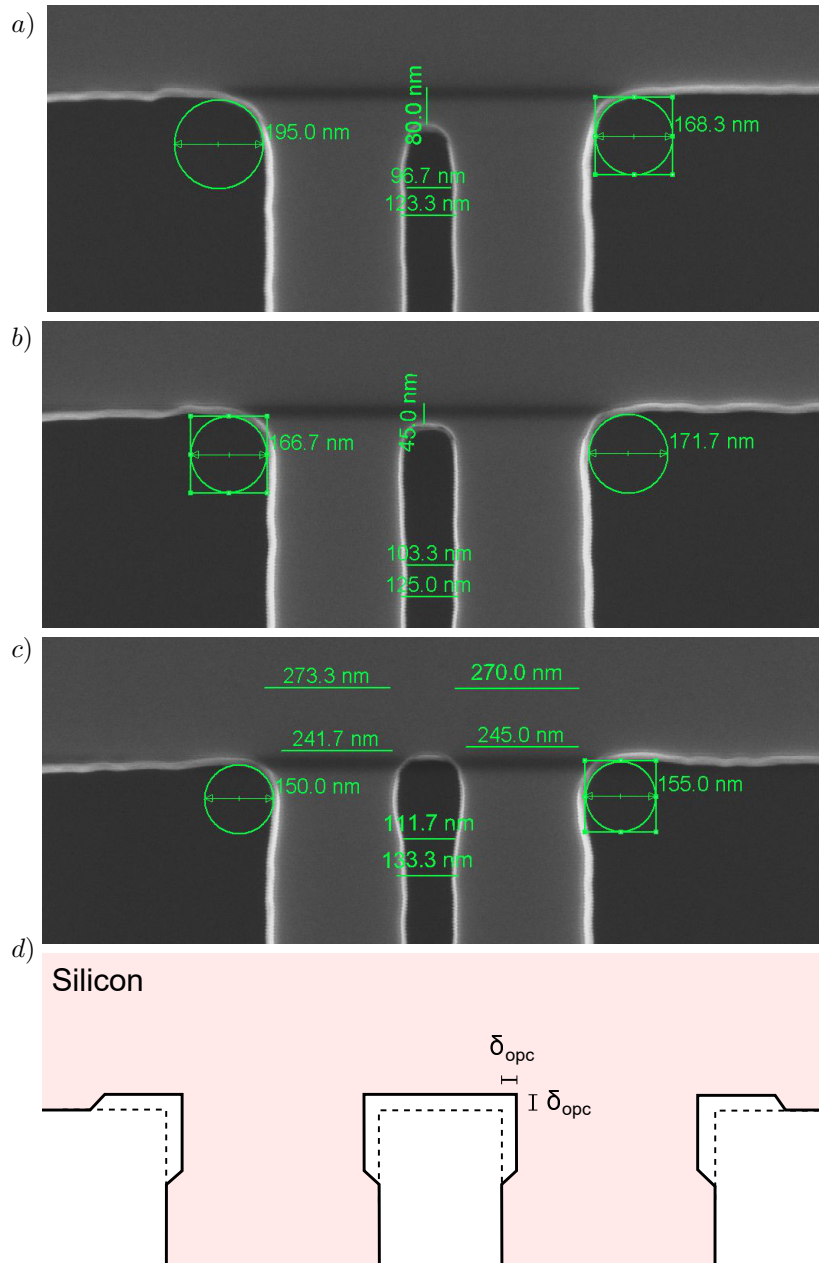


Figure 3.19: The result of (a) $\delta_{opc} = 0$ nm, (b) 30 nm, (c) 60 nm designed cut into the base of the cantilevers (d) drawing of the mask design. As a result the radius of the corner is reduced from 91 nm to 76 nm. The largest cut is beginning to dig into the width of the cantilever.

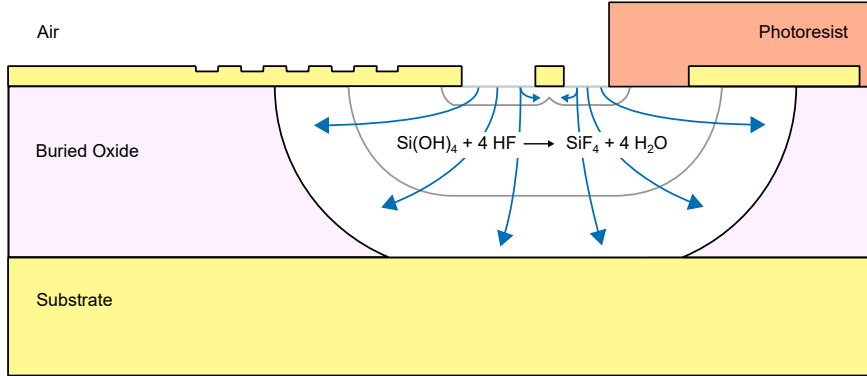


Figure 3.20: Diagram of underetching a waveguide. The grey contours show the air-oxide interface as the etching progresses. The structure on the right would be underetched without the photoresist delaying the etch.

Task	Time
Clean sample	
Spin coat TI35E, 4000 rpm	40 s
Soft bake, 100 C	180 s
Contact lithography	60 s
Wait	20 min
Soft bake, 125 C	120 s
Flood Exposure	185 s
Develop, AZ400K:H ₂ O (1:3)	105 s
Wet etching, BHF	80 nm/min
Careful Rinse, DI water	
Critical point drying	

Table 3.1: Receptie for under-etching mass sensor

pletely or waveguides and tiling from nearby structures will inevitably float over and land on critical structures after they have been etched free. It does, however, relax the demands on alignment, development and etch-time making the results more repeatable.

3.5.3 Stiction

As the features of MEMS structures are so small surface forces are much more important than for macroscopic devices. Thus when fabricating devices in the micro- and nanometer size category water tension is a significant obstacle. When drying the sample after it is under-etched, small droplets of water gets caught in between the device and the substrate and the capillary force starts pulling them

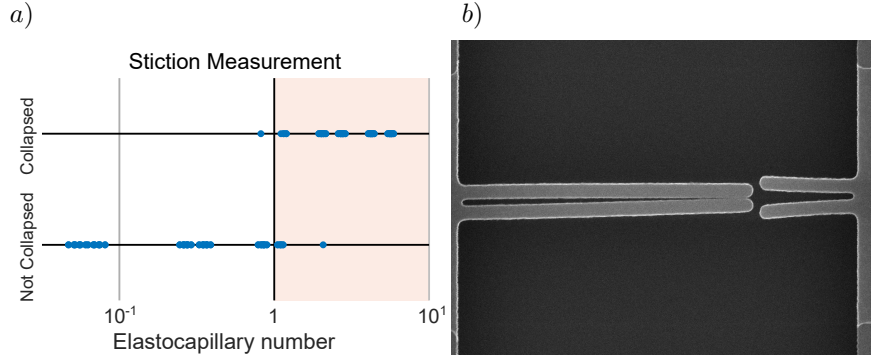


Figure 3.21: a) Outcome of stiction test on a group of mass sensors. Under-etched with HF, washed with water then dried. An elastocapillary number above 1 should result in collapse. Only one cantilever pair that should not have collapsed did. b) SEM image of collapsed mass sensor where the tips are stuck together.

together. Once they touch even stronger forces such as Van der Waals force take over and they are very difficult to separate again.

The magnitude of the forces can be calculated from the surface energy directed along the contact angle. The surface energy of water is 72 mJ/m^2 which results in a force, $\gamma_{L,water} = 72 \text{ mN/m}$. The contact angle is more difficult to ascertain as it depends on the surface affinity for the liquid. That affinity is affected by many of the chemicals used in the processing i.e. HF and by the geometry. It is about $\alpha_{c,si-water} = 65.2$ degrees at the water silicon interface after etching with HF [11].

The resulting deflection can be calculated analytically for simpler structures like cantilevers but it is often preferable to simulate them in a FEM solver like COMSOL as it can include non-ideal anchoring. The result of a stiction test on a dice full of mass sensors is shown in figure 3.21. The elastocapillary number is the deflection caused by the liquid divided by the distance to the surface. In the case of figure 3.21 the expected deflection is calculated from the Euler-Bernoulli equations for cantilevers under static loads.

$$N_e = \sin(\alpha_c) \frac{\gamma_L L^4}{2EIH}; \quad (3.14)$$

If the structure does collapse due to water tension it is sometimes possible to dry the device in another liquid such as isopropanol which has about a third of the surface energy, $\gamma_{L,IPA} = 23 \text{ mN/m}$. It is sometimes possible to avoid stiction by clever design either by designing a stiffer structure or by minimising the contact surface of the collapsed structure so that it can pull free by itself.

If clever design is still not enough a critical point dryer (CPD) can be used to avoid the problem. It slowly replaces acetone with liquid CO_2 under high pressure and brings the pressure and temperature up until the CO_2 is a supercritical fluid, it

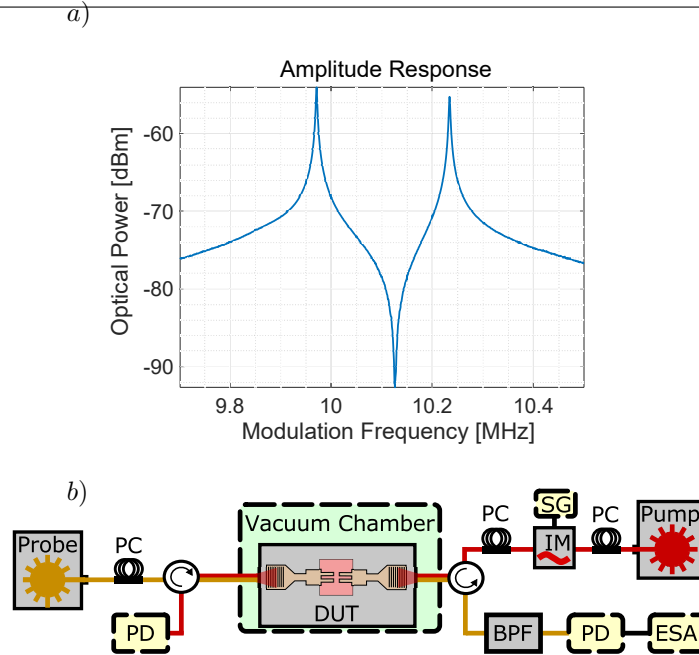


Figure 3.22: a) A measurement of the amplitude response of an optically driven cantilever. The cantilever is driven and the vibration detected at the same frequency. b) The setup of the optically driven measurement.

rounds the critical point and brings the pressure and temperature down until the CO_2 is a gas. By transitioning via the supercritical fluid it avoids crossing the solid-gas transition boundary and surface tension is no issue. This is how the cantilevers of the longest mass sensors were under-etched. It is also sometimes possible to avoid using liquids when under-etching, i.e. vapour-phase HF (VHF).

The etchant in the VHF process starts as a gas but quickly forms a thin layer covering the dice consisting almost entirely of strong aqueous fluosilicic acid. Despite being in gas phase it is still a very potent etchant. After a short startup time it is attacking oxide at about the same rate as BHF [12]. It is however very difficult to find a photoresist able to withstand it so it is therefore advisable to design structures with that in mind.

3.6 Optically driven measurements

By driving the sensor optically we amplify the vibration way above the thermal and electric noise floor. Figure 3.22 a) shows the result of such an experiment, combining a probe beam at 1555 nm with an intensity modulated pump, which excites the mechanical vibrations. The measurement setup is illustrated in figure 3.22 b). The pump laser passes through the intensity modulator (IM) that is driven

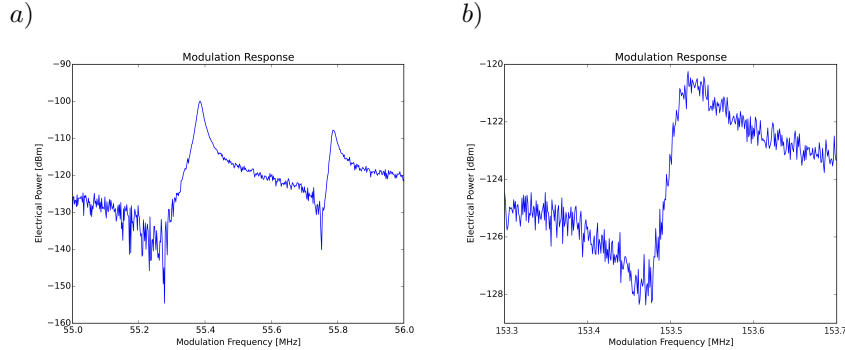


Figure 3.23: The amplitude response to an optical drive of the (a) second order and (b) third order mode. The third order mode only shows one peak because the low signal from symmetric mode disappears under to noise.

by the signal generator (SG). The probe passes through the device (DUT) in the opposite direction and is then redirected away from the pump path by a circulator. The reflection of the pump is filtered out in the bandpass filter (BPF) and detected by a photodiode. The signal from the diode is then processed by the electric spectrum analyser (ESA).

The pump power leaving the chip is $60 \mu W$, which corresponds to $120 \mu W$ of peak-to-peak modulated power in the cantilevers. After the light couples out of the chip the pump is filtered out and the probe power read by the photodiode. To balance the extinction of the pump after the filter with the power coupled through the grating coupler the pump wavelength is offset from the probe wavelength by 15 nm to 1570 nm .

The cantilever measured, a $6 \mu m$ long, 280 nm wide, 220 nm thick cantilever, has an effective mass is 215 fg and the mass responsivity 146 ZHz/kg .

The higher order modes are much stiffer and have a much worse coupling to the force. Thus the amplitude we can drive them to is much lower but we can still measure them by post amplifying the probe with an EDFA as was done with the thermally stimulated measurements. The results are shown in figure 3.23. The symmetric version of the third order mode still disappears under the noise floor, however.

Here the optical nonlinearities start to show. Two-photon absorption makes it so that the pump imprints on the probe. The interference between that imprint and the mechanical signal interfere and cause a Fano resonance.

3.7 Measured noise

An actual measurement of the frequency noise can be done using the same setup as used earlier for the driven measurement. The ESA can extract the phase and

amplitude noise from sidebands of the driven resonator.

Figure 3.24 shows a direct phase noise measurement of the cantilevers taken with the ESA. The corresponding frequency noise gives for a 100 Hz measurement bandwidth a mass sensitivity of 500 kDa, 3 times more than equation 3.7 would suggest. This is comparable to a protein such as the RNA polymerase of *E. coli* (450 kDa). We suspect that part of the extra noise at the lower frequency side of the noise spectrum is due to long term thermal drifts as there is no thermal stabilisation in the vacuum chamber. The two peaks at 20 Hz and 100 Hz are equipment related. Finally, even though the cantilevers are separated in resonance frequency there is still a coupling between them that is not taken in to account for the analytically model of the noise.

This mass sensitivity is in line with published sensors [13, 14] and the calculated thermomechanical noise of previously suggested all-photonically transduced mass sensors [10, 15], while using a significantly smaller pump power. The lower power makes it possible to limit crosstalk via material non-linearities from the pump onto the probe. The mass sensitivity should be possible to improve by increasing optical pump power or mechanical quality factor. The optical pump power is for the current setup limited by the tolerances of the modulator.

3.8 Conclusion

In this chapter we have discussed a demonstration of an all-photonically transduced, CMOS compatible resonant mass sensor in the SOI platform. Exploiting the strong gradient force in slot waveguides to actuate the results of the vibration in a strong signal to noise ratio with respect to the thermomechanical noise. Relying on in-plane vibrations makes it possible to optimize the displacement sensitivity and mechanical mode shape in the design phase. Using 120 μW of modulated optical power the sensors fabricated are measured to be able to resolve 500 kDa. The displacement sensitivity is measured over a 35 nm span to strengthen the argument that it is a broadband device simplifying the calibration of the sensor and relaxing the constraints imposed on the surrounding circuit. We have also discussed the performance of a dissipatively coupled mass sensor system, its merits and demerits.

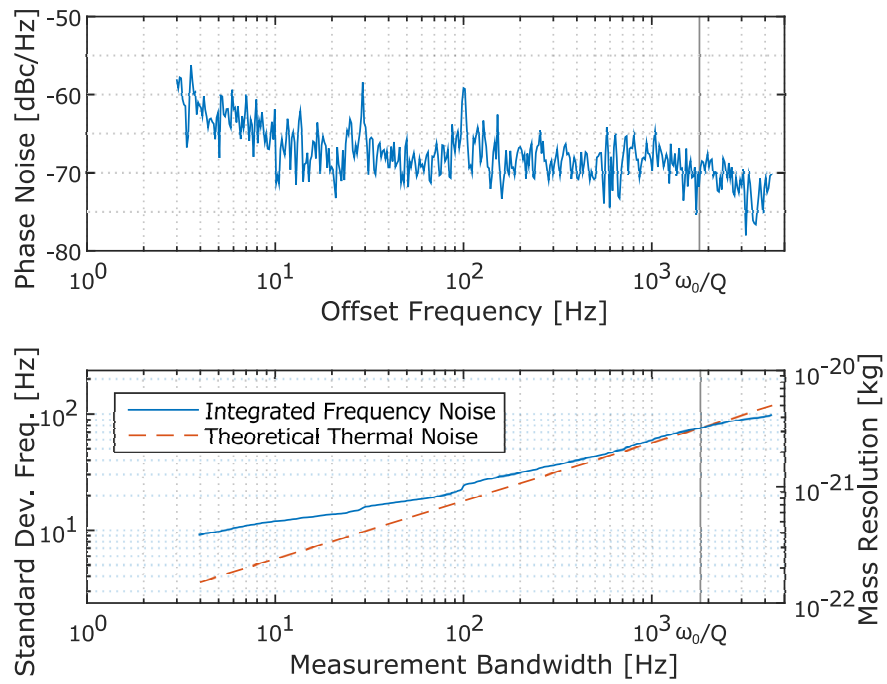


Figure 3.24: (a) Phase noise and (b) Frequency noise of a $6\mu\text{m}$ cantilever. The calculated thermomechanical noise is included in the figure as a reference. Also marked is the mechanical decay rate ω/Q_{mech} marking the rate with which noise decays.

References

- [1] M Selim Hanay, Scott I Kelber, Cathal D O'Connell, Paul Mulvaney, John E Sader, and Michael L Roukes. *Inertial imaging with nanomechanical systems*. Nature nanotechnology, 10(4):339, 2015.
- [2] KL Ekinci, YT Yang, and ML Roukes. *Ultimate limits to inertial mass sensing based upon nanoelectromechanical systems*. Journal of applied physics, 95(5):2682–2689, 2004.
- [3] Eduardo Gil-Santos, Daniel Ramos, Anirban Jana, Montserrat Calleja, Arvind Raman, and Javier Tamayo. *Mass sensing based on deterministic and stochastic responses of elastically coupled nanocantilevers*. Nano letters, 9(12):4122–4127, 2009.
- [4] Xiankai Sun, Jiangjun Zheng, Menno Poot, Chee Wei Wong, and Hong X Tang. *Femtogram doubly clamped nanomechanical resonators embedded in a high-Q two-dimensional photonic crystal nanocavity*. Nano letters, 12(5):2299–2305, 2012.
- [5] Mian Zhang, Shreyas Shah, Jaime Cardenas, and Michal Lipson. *Synchronization and phase noise reduction in micromechanical oscillator arrays coupled through light*. Physical review letters, 115(16):163902, 2015.
- [6] James M Lehto Miller, Azadeh Ansari, David B Heinz, Yunhan Chen, Ian B Flader, Dongsuk D Shin, L Guillermo Villanueva, and Thomas W Kenny. *Effective quality factor tuning mechanisms in micromechanical resonators*. Applied Physics Reviews, 5(4):041307, 2018.
- [7] BD Hauer, C Doolin, KSD Beach, and JP Davis. *A general procedure for thermomechanical calibration of nano/micro-mechanical resonators*. Annals of Physics, 339:181–207, 2013.
- [8] Dirk Taillaert, Wim Bogaerts, Peter Bienstman, Thomas F Krauss, Peter Van Daele, Ingrid Moerman, Steven Verstuyft, Kurt De Mesel, and Roel Baets. *An out-of-plane grating coupler for efficient butt-coupling between compact planar waveguides and single-mode fibers*. IEEE Journal of Quantum Electronics, 38(7):949–955, 2002.
- [9] Dirk Taillaert. *Grating Couplers as Interface between Optical Fibres and Nanophotonic Waveguides*. PhD thesis, Ghent University, 2004.
- [10] Mo Li, WHP Pernice, and HX Tang. *Broadband all-photonic transduction of nanocantilevers*. Nature nanotechnology, 4(6):377, 2009.

-
- [11] MG Kibria, F Zhang, TH Lee, MJ Kim, and MMR Howlader. *Comprehensive investigation of sequential plasma activated Si/Si bonded interfaces for nano-integration on the wafer scale*. *Nanotechnology*, 21(13):134011, 2010.
- [12] PJ Holmes and JE Snell. *A vapour etching technique for the photolithography of silicon dioxide*. *Microelectronics Reliability*, 5(4):337–341, 1966.
- [13] E Forsen, G Abadal, Sara Ghatnekar-Nilsson, J Teva, J Verd, R Sandberg, W Svendsen, Francesc Perez-Murano, J Esteve, E Figueras, et al. *Ultra-sensitive mass sensor fully integrated with complementary metal-oxide-semiconductor circuitry*. *Applied Physics Letters*, 87(4):043507, 2005.
- [14] Gabriel Vidal-Álvarez, Jordi Agustí, Francesc Torres, Gabriel Abadal, Núria Barniol, Jordi Llobet, Marc Sansa, Marta Fernández-Regúlez, Francesc Pérez-Murano, Álvaro San Paulo, et al. *Top-down silicon microcantilever with coupled bottom-up silicon nanowire for enhanced mass resolution*. *Nanotechnology*, 26(14):145502, 2015.
- [15] Dmitry Yu Fedyanin and Yury V Stebunov. *All-nanophotonic NEMS biosensor on a chip*. *Scientific reports*, 5:10968, 2015.

4

Designing waveguides for stimulated Brillouin scattering with genetic algorithms

4.1 Introduction

Genetic algorithms are designed to find a sufficiently good solution to an optimisation problem often using incomplete or imperfect information or limited computation capacity. Generally, this is made more difficult by that the set of solutions is too large to be fully sampled. Genetic algorithms are inspired by natural selection and rely on bio-inspired operators such as mutation, crossover and selection.

4.1.1 The history of genetic algorithms

The first ideas of genetic algorithms are as old as the invention of the computer itself. As early as 1950 Allan Turing [1] suggested a learning machine that could search for satisfactory solutions with a process analogous to evolution. Following that came several years when evolutionary biologists were modelling artificial selection. In the 1960s Hans-Joachim Bremermann executed computer experiments that included the elements of modern genetic algorithms such as a population of solutions to the optimisation problem, recombination, mutation, and selection. During this time, three different implementations of the basic idea were developed in different places. Calling the process 'evolutionary programming', 'genetic algo-

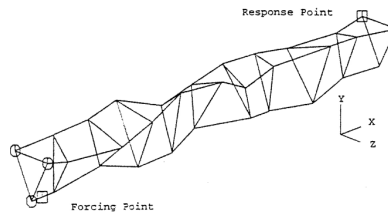


Figure 4.1: Optimized satellite boom [2].

rithm' or 'evolution strategies' the field developed separately for about 15 years. Then in 1985, the first international conference specialising in the subject was held in Pittsburgh and then repeated every second year for more than a decade. In 1993 the first scientific journal devoted to evolutionary algorithms, *Evolutionary Computation*, was launched. In the early 1990s, a fourth implementation following these general ideas called genetic programming emerged.

An example of a successful application of genetic algorithms is a satellite dish holder boom designed by Keane et al. [2]. The latticed boom connects the satellite with a communication dish so it is crucial that it is stable to maintain alignment. In space there is no air damping to limit vibrations, and if they are allowed to build up they could break the whole structure. Using genetic algorithms they managed to design a boom that is 200 times better at damping the vibrations than traditional structures. The final design looks more like a random drawing than something intentionally designed but by iterating through a number of generations they succeeded in generating a much more robust structure. Closer to home, genetic algorithms has also been used to design photonic crystals with great success.

4.1.2 The language of genetic algorithms

Genetic computation as an approach lends concepts from several different fields and ideas and as a result a lot of field specific jargon is used interchangeably outside of its regular context. The language is further complicated by the introduction of the Brillouin scattering context our work is situated in. To avoid confusion we define these expressions in the context of the thesis,

- *Genotype* refer to the whole gene string of an individual, e.g. the DNA molecule or the integer matrix I have used to represent the waveguide cross section. The collection of all the possible shapes is sometimes referred to as the genotype space.
- *Phenotype* refers to the observable characteristics of an individual, e.g. blue eyes or the effective refractive index of an optical mode. All the possible variations are referred to as a phenotype space. For this work, we specifically refer to the properties of a specific optomechanical mode pair and not

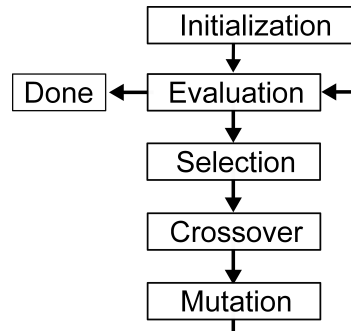


Figure 4.2: Flowchart of a standard genetic algorithm.

to the waveguide in general as it is often multimode and would therefore often have both high and low effective refractive index.

- Mapping genotype onto phenotype is often called *encoding*. The encoding, in this case, is the simulation of waveguide modes and calculation of mode parameters. Mapping phenotype on genotype is called *decoding*.
- A *gene* is the specific value in a representation of one of the individuals, i.e. parts of the DNA string or an element in the matrix. A possible version of a gene is called an *allele* which in our case refers to the material of a part of the waveguide, e.g. silicon.
- The *fitness landscape* is an illustration of the distribution of phenotypes. Since the genotype space is generally very high-dimensional it is difficult to actually show and instead a topographic map is used for educational purposes.

4.2 The algorithm

For a genetic algorithm (GA) there are typically five phases to consider: generating the initial population, evaluating sample fitness, selection of the samples from which to generate the next generation, crossover and mutation,

- The initial population refer to the genomes that the algorithm starts with. They must be chosen or generated by another method than the genetic algorithm.
- In the evaluation phase each sample is given a fitness score. It is from this value it is later ranked and survival is determined. It is also possible to constrain the values and limit the phenotype space.

- In the selection phase it is decided which waveguides will make the parents to the next generation. The selection phase is responsible for the incremental improvements to the population. Without the selection phase and with only a mutation phase the GA would be just a random search algorithm.
- The crossover phase dictates the selection process for which genes are passed on.
- The mutation phase takes a fraction of the population and randomly introduces changes to them to maintain diversity. Without it the only possible outputs of the algorithm are those present in the initial population.

The flow of the algorithm is illustrated in figure 4.2.

4.2.1 Parallel computing

One of the critical trade-offs when choosing an optimisation method is the available processing power. Genetic algorithms are very well suited to be run in parallel. For this work, the part taking the longest time is the waveguide simulations and the gain calculations. Since these tasks are independent of the other waveguides they can be distributed among several different computers. This give an almost linear increase to the computation speed.

4.2.2 Choosing the right genotype space

When designing a genetic algorithm the initial step is to find a way to represent the solution candidates in a way that a computer can work with. Getting the representation right is one of the most challenging parts in a successful implementation of the algorithm. This is something that comes with experience and knowledge of the phenotype space. There are several distinct methods of representing the system but often a combination of them give a better result than any of the individual approaches alone. The choice of representation also dictates which genetic operators are available.

4.2.2.1 Binary representation

One of the most straightforward representations is binary representation. It is one of the oldest representations and has found use in a wide variety of implementations. In this case, the genotype is a string of binary digits. The representation is then dependent on the interpretation of the individual bits and the length of the string itself. The mapping between the string and the phenotype space must be in such a way that all of the possible configurations of the bit string give valid solutions.

One of the freedoms of the binary representation is that it is possible to encode non-binary information by using several bits, an 8-bit string can represent any integer up to 256. A problem with this representation is that the different bits have a very different influence on the represented number. A 7 (0111) turning into an 8 (1000) requires three bits to flip while a 6 (0110) only needs a single one. By instead using Gray coding, which is a variation of the mapping of binary to integer, it is possible to reduce that to one bit-flip per number.

1	0	1	0	0	1	0	1	0	1
---	---	---	---	---	---	---	---	---	---

Figure 4.3: Example binary genome

The most common mutation operator for the binary representation is to give all genes a probability to bit-flip. How high that probability should be depends on the use case but it is often chosen so an average of one is flipped.

1	0	1	0	0	1	0	1	0	1
↓									
1	0	0	0	1	1	0	1	1	1

Figure 4.4: Example binary mutation

The typical crossover operator generates two children from two parents. Following one or several crossover points somewhere along the genome the genome is switched with the other sample, see figure 4.5. It has the inherent bias that genes that are close to each other are more likely to stay together. An odd number of crossover points has a very strong bias against keeping the start and end of the genome together. It is also an option to individually treat the genes and give them each a probability to cross over; this would eliminate the position bias if it is preferable. The trade-off is that it would introduce a distribution bias instead.

P1:	1	0	1	0	0	1	0	1	0	1
P2:	0	0	1	1	0	0	1	0	1	1
↓										
C1:	1	0	1	1	0	0	1	0	1	1
C2:	0	0	1	0	0	1	0	1	0	1

Figure 4.5: Example binary crossover

4.2.2.2 Integer representation

The binary representation is not always suitable for situations where genes can take several different values. In these cases, another common representation is the integer representation. The integers themselves can be unrestricted or be limited to a set, e.g. one of the twenty-four hours in a day or four different colours. In some of these cases, it can be essential to consider if there is a natural relationship between the numbers. Something happening at 4 o'clock is more likely to relate to what is happening at 5 o'clock than 13 o'clock. The same might not be possible to say about the choice of colour.

1	3	2	6	2	1	9	2	4	1
'South'	'West'	'South'	'North'	'East'	'East'				

Figure 4.6: Example integer genomes

The choice of mutation operator for an integer representation has other candidates than for the binary representation. Depending on the connection between the possible integer values it might make sense for the mutation to change the value by an increment, by a uniform probability where all values are possible or even by a Markov chain. The crossover is often treated in a similar way to the binary version.

4.2.2.3 Real-valued representation

Then there is the real-valued representation where the genes are represented by a floating-point value. It is suitable when representing a continuous quantity such as often is the case when representing physical quantities such as length and width. The precision of the floating-point values is often limited by the implementation of the algorithm.

1.543	2.12	2.935	6.45	2.478	1.384	9.11
-------	------	-------	------	-------	-------	------

Figure 4.7: Example real-valued genome

The mutation analogous to bit-flipping for the real-valued representation is to choose a value within the allowed range randomly. Another option is to add a value from a Gaussian distribution with an expectation value of zero. It is common to apply it to all the genes and instead control the rate of change with the standard deviation of the Gaussian.

There are new considerations when tuning the crossover operator, however, since it is no longer necessarily a choice between two alleles. There are three

common options for how to combine two real-valued strings. There is the bit string version mentioned earlier which has the problem that new numeric values are only introduced in the mutation step. The second method takes a random value between the two parent values. This method ends up having an averaging effect on the values, however. The third version chooses one of the parent values and adds a small value to it.

4.2.2.4 Permutation representation

Many problems instead depend on the sequence of events, in which case it is possible to use a permutation representation. It is a list of events that all occur precisely once. It is essential to keep in mind that there two kinds of problems that are represented by permutations: problems where the order of events is important and problems where the adjacency of the genes is important. A typical order problem is production scheduling where the goal is to optimise production time when producing several different widgets all competing for the same equipment. A typical adjacency problem is the travelling salesperson problem where the goal is to find a complete tour between a series of cities at the shortest possible time.

1	2	4	3	7	9	8	6	5	0
---	---	---	---	---	---	---	---	---	---

Figure 4.8: Example permutation genome

In this case it is no longer possible to consider the genes individually, instead, the whole genotype undergoes mutation. In its most simple version, the mutation switches the place of two or more genes. Another option is to bring a few randomly selected genes together. A third selects a chunk of genes and inverses the order.

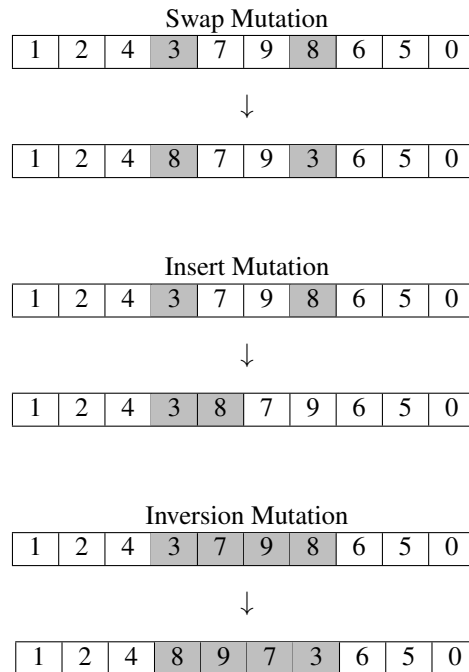


Figure 4.9: Three examples of permutation mutations

The permutation representation demands some more complicated crossover methods since the order of the genes is essential. There are however some methods in literature that aim to preserve the neighbours or the order in the parent samples like partially mapped crossover [3], edge crossover [4] and cycle crossover [5].

4.2.2.5 Tree representation

Tree diagrams are a way to represent hierarchical structures. A tree representation offers a general approach to express code using a formal syntax. It is, therefore, the basis for genetic programming. The syntax consists of a set of symbolic expressions that can be divided into two categories: a function set and a terminal set. The terminal set is allowed as leaves (e.g. the numbers in fig. 4.10) while the functional set is the nodes (e.g. the mathematical operators in fig. 4.10).

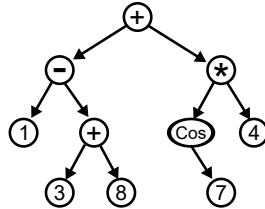


Figure 4.10: Example tree genome.

The mutation can be done by randomly replacing one of the elements with another operator and the crossover can be done by taking a branch from one parent and replacing it with a branch from another parent.

4.2.3 Parent selection

The improvements to the population originate from the parent and the survivor selection method. It is a balancing act between maintaining a diverse population so there are options for improvement and discarding bad solutions.

4.2.3.1 Fitness proportional selection

The parents are selected with a probability proportional to their fitness score. A fitter parent occupies a greater proportion of the probability space and therefore has a greater chance of being chosen. The probability of being selected as a parent is $P_i = F_i / \sum_{j=1}^n F_j$, where F_i is the fitness of individual i out of a population the size of n .

It is a great way to promote good solutions but it has two problems: exceptional individuals quickly dominate the whole population leading to premature convergence and populations of similar fitness parameters has almost no selection pressure.

4.2.3.2 Ranking selection

A response to the problems of fitness proportional selection is to instead bias the selection based on the ranking of the individual. Since the range of possible ranks are known it keeps the selection pressure within well-regulated margins. The question instead becomes how aggressively to promote better individuals. There are several ways to generate the probabilities but it is often a linear function dependent on how many samples it ranks better than.

4.2.3.3 Uniform parent selection

Lastly there is the option of selecting the parents by giving all the surviving samples the same probability of being selected. Using a uniform selection bias might

seem like it is a way of avoiding including a selection pressure but can be managed by introducing a strong survivor bias instead.

4.2.4 Survivor Selection

The most important function of the survivor selection method is that it keeps the amount of data down. Many implementations of genetic algorithms iterate through the generations quickly and can generate significant amounts of data so that even modern computers can have problems keeping up.

4.2.4.1 $(\mu + \lambda)$ selection

If there are λ offspring each generation and μ of the population survives to the next one, then one way of selecting the survivors is to rank all of the $\mu + \lambda$ individuals and then select the μ best-ranked individuals.

As a selection method it can quickly improve the mean fitness of the population but there is also a high risk for premature convergence. This is primarily because it keeps the best individuals indefinitely. If a good representative of a local maximum is generated then the algorithm is most likely going to be stuck there.

It can be managed somewhat by enforcing that there are no identical individuals in the current generation. The selective pressure is relative to the proportion of the offspring to parents ($\lambda : (\lambda + \mu)$).

4.2.4.2 (μ, λ) selection

Another option is to discard the older generation entirely and only select the survivors from the best ranking among the λ individuals generated for this generation. It does of course require $\lambda > \mu$. This way the influence of any single individual is limited but at the cost of losing them even if they are good candidates. The selective pressure is now ($\lambda : \mu$)

4.2.4.3 Generational selection

Lastly, one way of selecting the next generation is to remove individuals generated n generations ago. Since there is no ranking in between the samples for the selection it moves the selective pressure over to the choice of parent selection method.

4.2.5 Parameterizing a waveguide

For a computer to be able to handle the design and evaluation of a waveguide it needs a mathematical description. The choice of description can have a considerable impact on performance by disallowing certain types of shapes, changing the sensitivity to parameter changes, making functionally similar waveguides easier

to transition between or by influencing the speed and accuracy of the simulations. For the work with genetic algorithms we have chosen to rasterise the waveguide, as illustrated in figure 4.11.

Describing the waveguide as a grid where each pixel denotes the material of a small area has many benefits. Most importantly as long as the grid is large enough and the pixel size is small enough, it is capable of describing any possible shape. Second, it allows us to keep the same simulation grid across all simulations. Third, it is easy to both display and manually edit the waveguides. Lastly, it makes detecting features that are too small or angled too sharply for fabrication easy.

A detriment is that translations and reflections of shapes end up being mathematically distinct while physically functioning identically. To evaluate several of them is a waste of simulation time. To identify them as identical is however computationally expensive. Another detriment is that many of the geometric operations traditionally used in manual design methods such as scaling the waveguide width become impossible to do accurately for most values. Finally, and more directly relevant to how the simulations are implemented, the rasterisation causes some practical problem for simulations of waveguides where two elements diagonal to each other are connected only in one of their corners. Such a connection is non-physical so any waveguide where such a connection is generated is removed and a new waveguide is generated.

For the simulations we have chosen to work with a 50 nm by 50 nm pixel size. Ultimately the dimensions are decided upon because they are around the lower limits of what we can lithographically pattern and allows for an acceptable simulation time.

It is also worth approaching this kind of choice from if the pixel size is small enough to resolve changes to the waveguide properties, i.e. single mode operation or avoided mode crossings.

Wire and rib waveguides are not so sensitive to a small change in size but slot waveguides and other more complex waveguides are often less tolerant. It is however possible to design a single (TE) mode slot waveguide with a 50 by 50 nm grid as can be seen from figure 3.10 in the subsection about slot waveguides. Another aspect to take into account is not accidentally to promote certain forces over others. It is therefore convenient that a 50 nm wide slot waveguide slot generates radiation pressure of a similar magnitude to the radiation pressure in a wire waveguide and not overly values slot waveguides over wire waveguides.

We have chosen to work with three materials: silicon, silicon oxide and air because it is one of the most popular material platform for integrated SBS and we have the facilities to work with it. Here when using just three types of materials there is no meaning to the indexes chosen for the materials. If the index is cyclic (... , 3, 1, 2, 3, 1, ...) then the other two materials are naturally always one increment away.

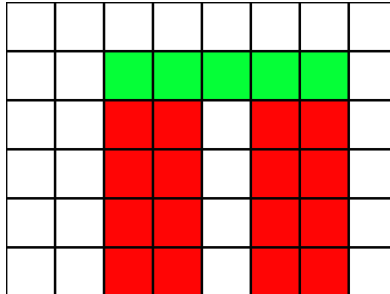


Figure 4.11: A sample rasterized waveguide. The different colors denote different materials.

4.2.6 Genetic operators for waveguides

We have chosen to work with two mutation operators. The first one simply randomly reassigns the values of a few of the elements in the waveguide matrix. It is there to increase diversity.

Since the dominant portion of the waveguides that have been designed are symmetric it makes sense to prioritise symmetric waveguides. By including an additional mutation that mirrors the waveguide along a symmetry line such waveguides will be generated. By simultaneously generating two symmetric waveguides, one from each side of the symmetry line, we limit the risk that the properties that make the waveguide good are lost.

The crossover operator is a more difficult choice. Physically it makes sense to try to preserve the waveguide shape locally. The 2-point crossover swaps the central section of the genome and thus big sections are kept together. Since we are using a matrix representation it is possible to use the crossover operator in both dimensions. Therefore the crossover operator used swaps a rectangular section between the two parent waveguides.

The waveguide simulations are slow and therefore we chose to use $(\mu + \lambda)$ survivor selection. It offers quick improvements of fitness across generations while the generations are simulated slow enough that the current results periodically can be manually inspected and evaluated. Since the survivor selection is quite harsh we have used a uniform parent selection to keep the algorithm as simple as possible.

4.2.7 Choosing an initial population

The initial population that forms the start of the algorithm is important and with a good start the algorithm has a much better chance of finding a good solution. Both the initial population size and its individual members have a significant influence on the performance. Some authors have suggested that having large initial diversity is of great help to avoid premature convergence. However, many parameters are

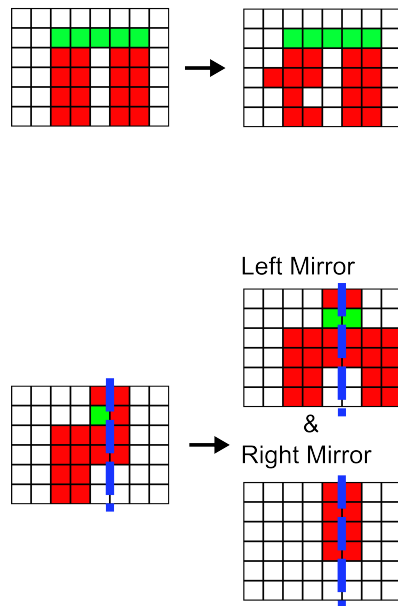


Figure 4.12: Our mutation operators.

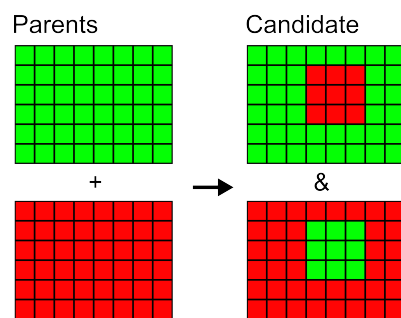


Figure 4.13: Our crossover operator.

at play here, e.g. the size of the search space, the selective pressure, and fitness function. One way of selecting the initial population is to include the information that is already available. In our case we can use waveguides that have previously shown good performance.

The majority of the measured SBS waveguides are either wire or rib waveguides. We also know that slot waveguides can generate strong optomechanical forces.

4.2.8 Selecting the parameters

The parameters of the algorithm were calibrated by replacing the computationally expensive Brillouin gain simulations with a series of simpler operations ranging from the simplest where the number of silicon pixels is maximised to much more advanced where it minimised the number of pixels with neighbouring pixels sharing the same material.

The population size was set to 100 and the parent selection to 50 % as it consistently managed to turn the whole waveguide into silicon. The mutation probability was later set to 30% to increase the level of diversity for later generations.

4.2.9 Functionalizing via context

Optical and mechanical modes are dependent on the full waveguide shape. The effect of a change of material in one pixel is dependent on the rest of the waveguide. If an important feature passes over from one waveguide to a waveguide where that feature does not make sense it is unlikely to yield good results. The likelihood that two waveguides produce a functional waveguide is therefore strongly dependent on how similar they are. Incremental changes are therefore more likely to survive the next selection phase. As generations pass by, specific locations in the waveguide matrix take on a function, e.g. slots will be found in certain rows and bulk silicon in certain regions.

If a radically new waveguide is introduced, it is less likely to generate more new waveguides that survive. The rasterised waveguides are unaffected by translation and mirroring but the crossover between a waveguide and its translation will see that difference. So when generating the initial population or when introducing a new waveguide into the database, it is important to be aware of how well the functions of the new waveguide overlap with the functions of the old waveguide. It will influence the speed with which these features are propagated among the new waveguides.

4.2.10 The importance of diversity

Maintaining a level of diversity among the samples that are passed on is key for the algorithm to progress. Only the genes that were selected in the previous iteration and the new genes that were introduced by the mutation are available. Too harsh selection parameters can remove the genes that are underperforming on their own but that in the right configuration of surrounding genes would perform well. This problem is in part alleviated by the mutation phase where new genes are randomly introduced. These new genes are however untested and a vast majority is detrimental to the waveguide so it is not an equivalent replacement.

We have approached the loss of diversity by enforcing that there are no identical waveguides among those passed on and by so imposing at least a minimum selection of genes. It can also be managed by increasing the chance of mutation.

4.3 Multiple objective optimization

The role of the evaluation function is to translate the quality of a phenotype into a value that can be ranked and compared. Since it forms the base for the properties that are selected for, it is essential that it values not only the best result but also the intermediate results.

Since we are selecting for a good SBS waveguide, we are evaluating the SBS gain. It is a parameter often used to showcase excellence in literature that we are also able to simulate. The gain simulations are expanded upon in the next chapter.

4.3.1 Multiple objective optimization

When the goal is more complicated than what can directly be captured by a single parameter and multiple solutions may come out as competitive, then the search is made more complicated. One way to approach the problem is to add the numbers together with a weighted sum. The parameters are multiplied with a weight, w , that re-scales them according to their importance.

$$F_{func} = \sum_{i=1}^n w_i p_i \quad (4.1)$$

It is a simplistic way of dealing with the problem that often experiences problems when taken outside its expected range.

Another way is to look for the Pareto optimal solutions. It is a term mostly used in economics that means that no solution is strictly better, that to improve one metric another one must be sacrificed. Illustrated in figure 4.14.

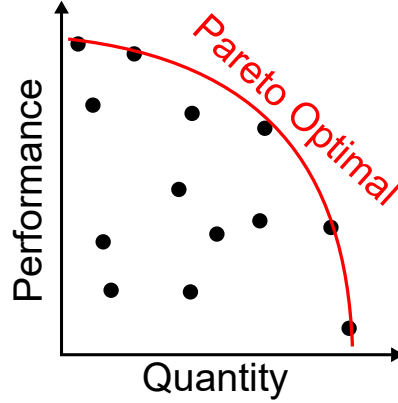


Figure 4.14: Example illustration of the pareto optimal solutions. The red line mark the options where you can not get more without performance.

4.3.2 Constraint handling

Another way to deal with multiple objectives is to guide the solution towards the part of the parameter space that is preferable. The preferences can be because the evaluation of samples outside that region is difficult or because the fitness provides very little guiding information in the region. One way to handle this is to remove the samples that end up there. It can, however, be challenging to know where to put such a limit on the search space. Another way is to include into the fitness function a function that is penalising undesired solutions.

$$F_{func} = F_{original}(x) * F_{penalty}(x) \quad (4.2)$$

The goal of our algorithm is to optimize the Brillouin gain over a wide range of mechanical frequencies. In order to focus on a specific frequency range we filter the gain function with a band-pass filter. The gain function itself will be further expanded upon in the next chapter explicit in the gain function is that it scales as $G \propto \Omega_{mech}^{-2}$. For a band-pass filter to be able to suppress that it needs to be of an even higher order ($i\omega^2$) but if we make the filter too selective it will be difficult to generate satisfying solutions. Another option is to compensate for how the gain is scaling by multiplying it with the frequency squared. An extra factor of $\omega_{mech}^{0.5}$ is introduced as well based on initial tests as we need to compensate for a fundamental frequency dependency of the electrostrictive force. The new fitness function is,

$$F_{func}(\omega) = F_{original}(\omega) \frac{\omega^{2.5}}{(\omega - \omega_{filt})^2 + (\omega/Q_{filt})^2} \quad (4.3)$$

where ω_{filt} is the central frequency of the filter and Q_{filt} dictates the width of the filter. A Q_{filt} of 3 was found to be good enough for this work.

When the GA has converged it is then possible to re-evaluate the data for a new filter frequency. A few generations later the algorithm converges at a new WG allowing for a fast generation of a competitive WG in a chosen frequency range. The re-evaluations are computationally much cheaper as it can be done from the parameters given by the old simulation. This means that each subsequent convergence can be sped up by an ever larger database of WGs to start from.

Ultimately however the algorithm must complement the underlying constraints of the problem, in our case Brillouin scattering.

References

- [1] A. M. Turing. *I.COMPUTING MACHINERY AND INTELLIGENCE*. *Mind*, LIX(236):433–460, 10 1950.
- [2] AJ Keane. *The design of a satellite beam with enhanced vibration performance using genetic algorithm techniques*. *Journal of the Acoustical Society of America*, 99(4):2599–2603, 1996.
- [3] David E Goldberg, Robert Lingle, et al. *Alleles, loci, and the traveling salesman problem*. In *Proceedings of an international conference on genetic algorithms and their applications*, volume 154, pages 154–159. Lawrence Erlbaum, Hillsdale, NJ, 1985.
- [4] J Watson, Charlie Ross, V Eisele, J Denton, José Bins, CDWAH Guerra, D Whitley, and A Howe. *The traveling salesrep problem, edge assembly crossover, and 2-opt*. In *International Conference on Parallel Problem Solving from Nature*, pages 823–832. Springer, 1998.
- [5] IM Oliver, DJd Smith, and John RC Holland. *Study of permutation crossover operators on the traveling salesman problem*. In *Genetic algorithms and their applications: proceedings of the second International Conference on Genetic Algorithms: July 28-31, 1987 at the Massachusetts Institute of Technology, Cambridge, MA*. Hillsdale, NJ: L. Erlbaum Associates, 1987., 1987.

5

Brillouin Scattering

5.1 Introduction

The second and third chapter focuses on mechanical resonators but an acoustic wave does not need to be confined in a resonator. This chapter focuses on how light interact with acoustic waves propagating in an optical waveguide. It starts with a short description of what makes Brillouin scattering different from the resonator case and the metrics that are used to qualify it. Then follows an analysis of the results of the genetic algorithm, both individual waveguides it found and the more overarching trends of the accumulated data.

5.2 Stimulated Brillouin scattering

The first significant difference between SBS and how we approached the driving of the slot waveguide cantilever resonator is that these waveguides are much longer than the ~ 10 μm cantilever length we have used. In the frequency space the intensity modulated drive that was used in the sensor consists of two frequencies separated by the modulation frequency. A simplified illustration placing this in the SBS context is shown in figure 5.1. The stronger optical wave is generally referred to as the pump. If the pump is modulated the resulting sidebands are called Stokes if it has a lower frequency and anti-Stokes, if it has a higher frequency. Because of the propagation speed along the waveguide change with frequency there is a spatial component to the phase of the optomechanical driving force. This component

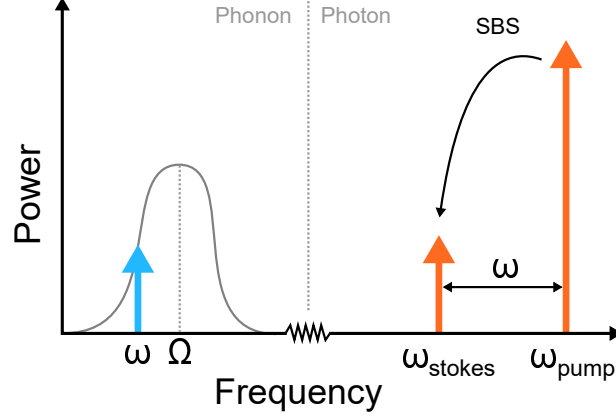


Figure 5.1: Illustrated spectrum of Brillouin scattering process. When the beat note between the two optical waves excite the mechanical resonance at Ω .

can be calculated by from the optical power in the waveguide,

$$\begin{aligned}
 P_{WG} &= (E_p \cos(\omega_p t - k_p z) + E_s \cos(\omega_s t - k_s z))^2 \\
 &= E_p^2 \frac{1 + \cos(2\omega_p t - 2k_p z)}{2} + E_s^2 \frac{1 + \cos(2\omega_s t - 2k_s z)}{2} \\
 &\quad + E_p E_s \left(\frac{\cos((\omega_p + \omega_s)t - (k_p + k_s)z) + \cos((\omega_p - \omega_s)t - (k_p - k_s)z)}{2} \right)
 \end{aligned} \tag{5.1}$$

where k_s and k_p are the optical wave vector of the stokes and the pump mode, in the same way ω_s and ω_p are the optical frequency of the stokes and the pump mode.

Since we are working in the infrared most of these frequency components are far out of reach for vibrational frequencies so typically only the $(\omega_p - \omega_s)$ term remains relevant as a drive force and included in that term there is a spatial component $(k_p - k_s)$. The mechanical mode must match that propagation component or the optical force will turn out of phase with the mechanical mode as it propagates along the waveguide. A more fundamental way of writing this is that both energy and momentum needs to be conserved in the scattering process. SBS is therefore reserved for combinations of mechanical and optical modes that satisfy these constraints, as illustrated in figure 5.2.

$$k_s - k_p = K \tag{5.2}$$

$$\omega_s - \omega_p = \Omega \tag{5.3}$$

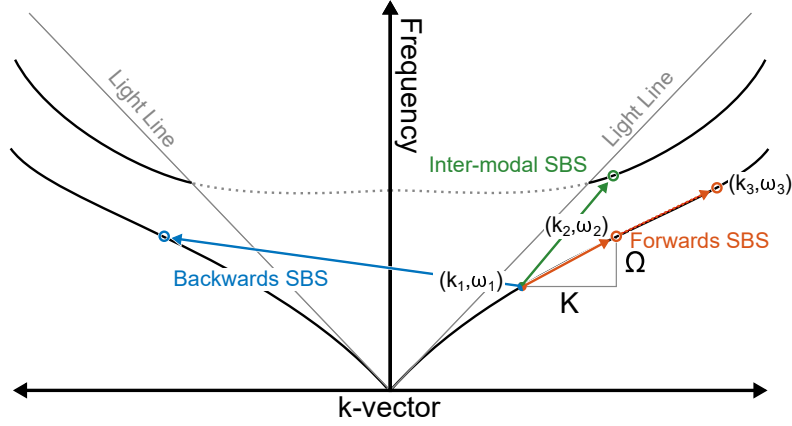


Figure 5.2: Example dispersion diagram of an optical waveguide with a scattering event marked by the orange arrow.

where K is the mechanical wave vector and Ω is the mechanical frequency.

These mode triplets are often talked about in terms of if they scatter the photon within the same optical mode (intra-modal SBS) or to another mode (inter-modal SBS) and if the pump and the Stokes waves propagate in the same direction (forwards SBS) or opposite directions (backwards SBS).

The backwards scattering process reflects the light and therefore act as a limit on how much power passes through the waveguide. Forwards scattering does not impose such a limit but it is instead often able to scatter the light several times in a row, spreading the optical energy between more frequencies.

The second significant difference between SBS and how we approached the driving of the slot waveguide cantilever resonator is that the transduction from mechanical wave to the scattering of the optical wave is now due to phase modulation. If the spatial and frequency components match then the Brillouin coupling efficiency is decided by how efficiently the light generates vibrations and how the vibrations modulate the effective refractive index of the optical mode. At the Brillouin frequency the gain coefficient can be reduced to [1],

$$G = \frac{2\omega_{opt}Q_{mech}}{\omega_{mech}^2} \frac{|\langle f, u \rangle|^2}{v_{gs}v_{gp}\langle u, \rho u \rangle} \quad (5.4)$$

where ω_{mech} and Q_{mech} denote the mechanical frequency and the quality factor. P_{opt} , ω_{opt} , v_{gs} and v_{gp} are the optical power, frequency and group velocity of the Stokes and the pump. $\langle u, \rho u \rangle$ is the effective mass of the waveguide cross section. The relevant material constants for silicon and silicon oxide can be found in the material properties section earlier in the thesis. The optomechanical force driving the vibration is $\langle f, u \rangle$ whereby,

$$\langle f, u \rangle = \langle f, u \rangle_{RP} + \langle f, u \rangle_{ES} \quad (5.5)$$

Now that we have the gain we can express the transduction between the optical modes in the waveguide. In the case of forwards inter-modal SBS the change in power of the stokes wave is,

$$\frac{dP_s}{dz}(z) = P_s(z)(-\alpha + GP_p(z) \frac{(\Gamma_{sbs}/2)^2}{(\Omega - \omega)^2 + (\Gamma_{sbs}/2)^2}) \quad (5.6)$$

$$\frac{dP_p}{dz}(z) = P_p(z)(-\alpha - GP_s(z) \frac{(\Gamma_{sbs}/2)^2}{(\Omega - \omega)^2 + (\Gamma_{sbs}/2)^2}) \quad (5.7)$$

P_p and P_s is the optical pump and Stokes power at a position z along the waveguide. α is the optical waveguide loss.

5.3 Simulating the coupling

Both optical and mechanical modes are simulated in COMSOL multiphysics. The simulated waveguide consists of a matrix (17 by 14 elements, 50 nm by 50 nm each) centred in a circular area of air with 3 μm radius. The simulation mesh is set to be identical for each matrix element. The outer boundary of the circle is made to be scattering by using Robin boundary conditions with a complex coefficient. The simulated modes are then imported via the Livelink module to MATLAB where the relevant field overlaps are calculated. With the simulation infrastructure available to us the full evaluation of a waveguide and its modes take about 2 min each.

In order to achieve this simulation time this work focuses on forward intra-modal SBS. Forward SBS requires far fewer simulation steps than backwards SBS where phase matching requires simulations at several mechanical propagation vectors. As a result of limiting the simulation to forward SBS, the mechanical waves do not propagate along the waveguide and, e.g. beam modes are not possible. For genetic algorithms the intra-modal gain is a simpler problem to optimise than inter-modal gain. The inter-modal coupling depends on three different mode shapes while the intra-modal essentially on only two.

While mode simulations, eigenfrequencies and dispersion are straight forward to simulate the losses in the waveguides are not, neither optical nor mechanical losses. The optical losses in silicon waveguides are generally surface roughness limited. That cannot be directly simulated since it is dependent less on the shape and more on the fabrication process. The mechanical losses are similarly challenging to capture and is covered in the mechanical losses sections. When comparing simulated quality factors with the literature of fabricated examples, it becomes evident that the ultimate limits for the achievable mechanical quality factor are

complicated, especially over a wide range of frequencies and shapes. To make the values comparable to literature the quality factor for the gain coefficient calculations has been set to 1000. This is roughly the same value as has been measured in suspended wire WGs and have been used for these kinds of simulations in the past [1, 2].

For lower frequencies far higher quality factors than 10^3 have been demonstrated [3]. It suggests the gain could be significantly higher for low frequencies than our simulated results imply. Quality factors in silicon resonators at this frequency are often limited not only by air damping, which is removed in vacuum, and surface oxide [4], which can be reduced through optimised fabrication but also by thermal material properties like Akhiezer and thermoelastic damping, which can be reduced by cooling. Ultimately it seems that the limit for the mechanical quality factor is inversely proportional to the mechanical frequency [3], further favouring the low-frequency structures.

5.4 The individual waveguides generated by the algorithm

5.4.1 Introduction

The shape space is large enough that it is unfeasible to explore it in its entirety (larger than 10^{113}) which is why we have to rely on an algorithm to guide the search. However, regardless of which shapes the algorithm has been initiated with it has converged towards a silicon slot waveguide with a low mechanical frequency. The initiation condition does however reflect itself in small changes such as the orientation of the resulting slot, horizontal or vertical. The convergence time is also heavily influenced by not just the best of the initial waveguides but also the diversity of the overall population.

The genetic algorithm generates a significant amount of waveguides, more than what can manually be investigated. It is easy to find the highest gain simulated. The highest gain is not necessarily the only interesting metric; so it is relevant to be able to find these waveguides.

Since we are working with a significant number of metrics the data can be expanded and displayed in many ways. Some of these are less significant for the performance but provide an insight into the data set. An example is the way a mode relates to the other modes guided by the waveguide. Without manual inspection it is difficult to differentiate the spatial mode shapes but sometimes it is enough to sort the modes according to the highest effective refractive index and lowest mechanical frequency. The results are displayed in figure 5.3.

As an example: for a large part of the lower mechanical frequency range the second optical mode (the slot mode) is the highest gain mode but as the mechanical

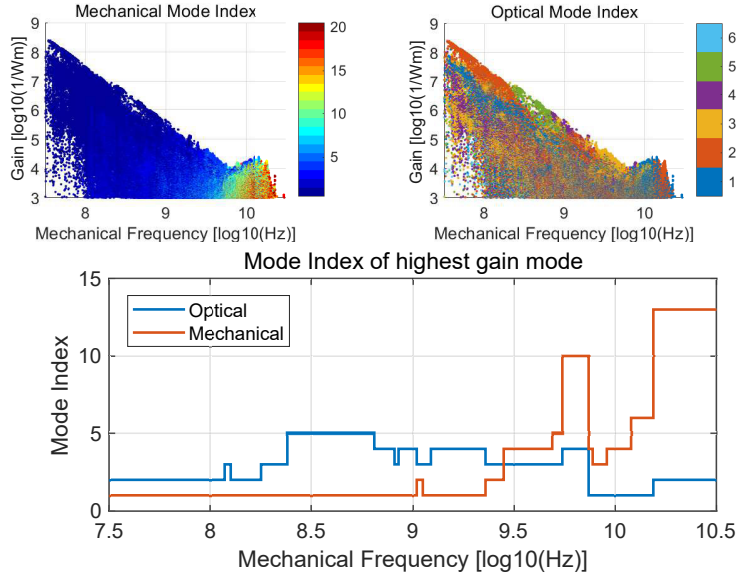


Figure 5.3: The modes index and ranked according to (a) lowest mechanical frequency and (b) highest effective refractive index of the waveguide. (c) the ranks of the highest gain modes as per their respective frequency.

frequency increases the fifth optical mode (a higher order slot mode) take over as the highest gain mode.

By including the more directly influencing parameter such as effective mass and optomechanical force it is possible to find several clusters of waveguides that are for some reason interesting.

5.4.2 Unique waveguides

Figure 5.4 shows the gain plotted against the mechanical frequency of all the optomechanical mode pairs generated. It also marks a few interesting mode pairs, which are displayed in detail in table 5.1 indexed by the letters a-i. These waveguides have been more directly optimised. The method is described in a later subchapter called local optimisation.

The highest gain mode pairs are found at the lowest frequencies simulated. Of those the absolutely highest gain is generated by WG (a), as shown in figure 5.4 and table 5.1. It is a slot WG where the optical mode is forced into the slot between two high refractive index sections [5]. The slot mode is beneficial in two ways: the associated radiation pressure is high and air is less optically nonlinear than silicon, allowing for the use of higher optical powers. In this case the two WGs are mechanically connected by a soft spring. The spring is made from oxide as silicon is

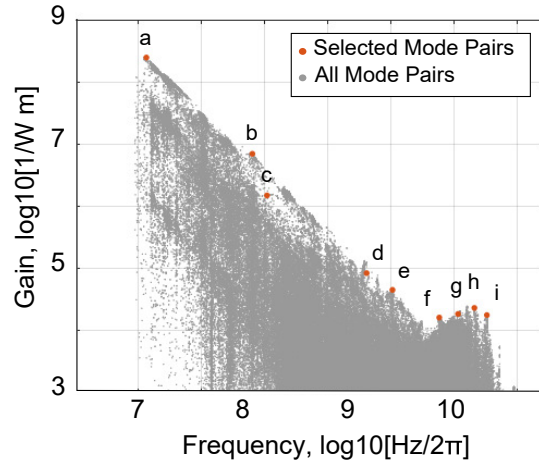


Figure 5.4: The gain and frequency of all simulated mode pairs. The modes and waveguides selected in table 5.1 are indicated by the dots labeled a-i.

stiffer, which would increase the mechanical frequency. Such an intricate mechanical connection makes fabrication difficult, however. By radically simplifying the connection we arrived at WG (c). While in this waveguide the coupling is worse than, e.g. WG (a), it is easier to fabricate and still has a higher gain than anything previously demonstrated.

There is also a group of highly competitive structures, which involves higher order optical modes. For these WGs the slot is situated above and connected to a slab of silicon. By introducing a high refractive index in the proximity of a slot that can guide a higher order slot mode, the degeneracy of the mode is broken and it splits up. This leaves modes, e.g. in WG (b) and WG (e), where the electric field is confined mostly in the top part of the slot where it is overlapping well with the mechanical mode.




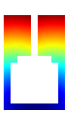
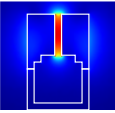

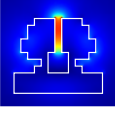
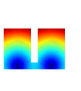

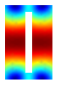
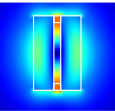
A way to avoid disturbing the optical mode with the mechanical connection is to have an identical connection on both sides, e.g. WG (d). It has the added benefit that it confines the mechanical mode so that the overlap of optical power and mechanical motion is better. It does however also, unfortunately, add some effective mass to the mode. Overall these mode combinations still result in a relatively high gain.

WG (f) demonstrates yet another type of mechanical connection. By moving the connecting parts towards the centre, the optical field in the slot now results in a significant radiation pressure that has the same phase as the electrostriction. As such, these forces can constructively add up to a respectable gain for the given frequency. It is also possible to increase the forces by increasing the group index.

A waveguide near the cut-off of an optical mode is usually more sensitive to the wavelength, which in turn results in a large group index. Designing for that effect leads to waveguides such as WG (g), which support higher order modes with very high group index.

Finally, the highest frequency range is populated by lamb wave modes, WG (h-i). These modes are the ones that are most common among the integrated SBS WGs already demonstrated in the literature, such as wire WGs [6].

So far missing from our discussion in this paper are rib WGs [7] and double slots [8]. Rib WGs are used mainly because they can have very low optical losses, something difficult to include in the optimisation process. They do however have a worse SBS coupling, which leaves the gain below the Pareto-curve. Double slots do not support forward SBS as the forces in both slots pull equally on the centre beam but in opposite directions and as such the forces cancel itself. The net forces suggested in [8] come from inter-modal SBS where the overlap between a symmetric and an asymmetric optical mode change the sign of the force on one side of the symmetry line, summing up to a substantial force.

INDIVIDUAL MODES					
Shape	Mech.	Optical	Simulated Performance		
 ■ Silicon ■ Oxide	Mech. Disp. 	Optical Amp. 			
a)			Gain: 2.5×10^8 1/Wm	Eff. Mass: 169 ng/m	
			Freq.: 37 MHz	Group Ind.: 3.14	
			Eff.Ind.: 1.50	ES: 217 nN/Wm	
			RP: 29.9 mN/Wm		
b)			Gain: 7.0×10^6 1/Wm	Eff. Mass: 103 ng/m	
			Freq.: 253 MHz	Group Ind.: 3.95	
			Eff.Ind.: 1.34	ES: 39.2 μ N/Wm	
			RP: 27.1 mN/Wm		
c)			Gain: 1.5×10^6 1/Wm	Eff. Mass: 85.3 ng/m	
			Freq.: 330 MHz	Group Ind.: 2.87	
			Eff.Ind.: 1.38	ES: 10.1 μ N/Wm	
			RP: 15.0 mN/Wm		
d)			Gain: 8.4×10^4 1/Wm	Eff. Mass: 191 ng/m	
			Freq.: 2.04 GHz	Group Ind.: 4.69	
			Eff.Ind.: 1.25	ES: 2.86 mN/Wm	
			RP: 29.9 mN/Wm		

Continued on the next page

Continued from the previous page

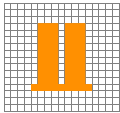
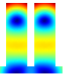
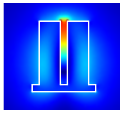
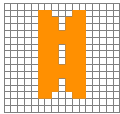
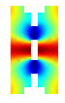
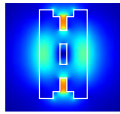
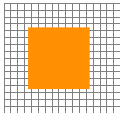
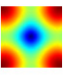
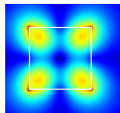
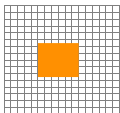
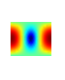
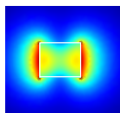
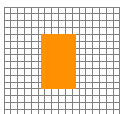
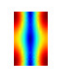
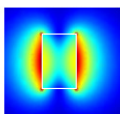
e)				Gain: 4.5×10^4 1/Wm Freq.: 3.27 GHz Eff.Ind.: 1.17 RP: 22.7 mN/Wm	Eff. Mass: 91 ng/m Group Ind.: 5.0271 ES: 3.90 mN/Wm
f)				Gain: 1.6×10^4 1/Wm Freq.: 7.68 GHz Eff.Ind.: 1.50 RP: 27.0 mN/Wm	Eff. Mass: 163 ng/m Group Ind.: 4.74 ES: 23.1 mN/Wm
g)				Gain: 1.9×10^4 1/Wm Freq.: 10.8 GHz Eff.Ind.: 1.31 RP: 70.9 mN/Wm	Eff. Mass: 203 ng/m Group Ind.: 8.58 ES: 13.6 mN/Wm
h)				Gain: 2.3×10^4 1/Wm Freq.: 14.6 GHz Eff.Ind.: 1.56 RP: 49.0 mN/Wm	Eff. Mass: 154 ng/m Group Ind.: 5.75 ES: 26.9 mN/Wm
i)				Gain: 1.8×10^4 1/Wm Freq.: 18.3 GHz Eff.Ind.: 1.44 RP: 75.6 mN/Wm	Eff. Mass: 91.5 ng/m Group Ind.: 5.57 ES: 18.5 mN/Wm

Table 5.1: A selection of competitive, distinct and noteworthy waveguides. They are indicated in figure 5.4 with red points. Shown, starting from the left, in each row are: material composition and shape, mechanical mode, optical mode and simulated performance. The shape is shown on top of a 50 by 50 nm grid. ES and RP are the electrostrictive and radiation pressure force. The forces are in all the given examples interfering constructively.

5.5 Local Optimization

5.5.1 Optimising the matrix representation of the waveguide

The way we have set up the genetic algorithm is not the most effective method for the last part of the local optimisation. The random search aspect of these optimisation schemes makes it difficult to exhaust the search space something that becomes realistic to do now that we are so close at least a local maximum. For the last step we have instead relied on deterministic methods. By following the small changes to the waveguide shape that gives the best improvement it steps towards an optimum.

The material interfaces are found by searching the waveguide matrix for in-

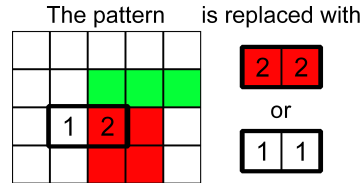


Figure 5.5: Two different integers found next to each other indicates a boundary. That pattern is then replaced.

teger pairs that signify a material intersection as shown in figure 5.5. Once two different integers are found next to each other they are replaced to move the interface in either direction. The list of new candidates is filtered to remove duplicates and evaluated. As a search method, it is exhaustive under the assumptions that reaching the optimum is not conditioned on the simultaneous introduction of several changes. It is worth to also include candidates that symmetrically apply these changes on both sides of the waveguide. The results of the simulation indicate it is often detrimental for the gain to break waveguide symmetry.

5.5.2 Reparametrizing the waveguide

When optimising around certain shapes it becomes clear that the resolution puts a limit on how close the process allows us to go. The speed of the gain simulation however also sets a practical limit to how fine the spatial resolution can be. Since we expect to be close to the maximum we can also assume that there are no drastic changes to the shape. Therefore the arguments for why we have been using the rasterised waveguide matrix are no longer as strong. We can re-express the waveguide as a polygon where the individual nodes can have arbitrary precision.

If we take a look at the highest gain waveguides we have found we can see that it is a slot waveguide where the strain components of the mechanical mode has migrated away from the optical field. The result is that the electrostrictive coupling for this mode pair is low so radiation pressure is the dominant part of the optomechanical coupling. Since the optic and strain fields are mostly separated it is now easier to manually redesign the waveguide. When doing so we find that we can push down the mechanical frequency to almost arbitrarily low values but that the shape to get such frequencies is increasingly difficult for a genetic algorithm to generate.

If we therefore for the moment consider the mechanical frequency and mode to be something we can choose as we want, we can simplify the simulation goal. By normalising the SBS gain to the mechanical frequency and assuming mechanical mode results in a modulation of the slot width much of the complications in SBS waveguide design disappear.

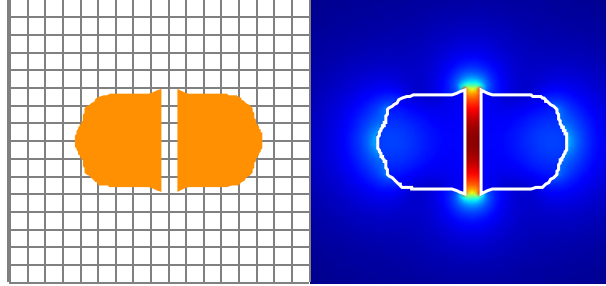


Figure 5.6: Optimized slot when the waveguide is re-expressed as a polynomial and the mechanical frequency independent of the optics.

We can then use a gradient descent method by approaching the coordinates of all the vertices as a single vector and then following the steepest decent towards the local optimum. The result is illustrated in figure 5.6, with a frequency normalized gain of $k_{opt} = 1.45 \times 10^{25} m^{-1} W^{-1} s^{-2}$, as displayed relative to the rest of the data in figure 5.7. With the k_{opt} -curve as a reference it is now visible which waveguides exceeds it. A majority of these are concentrated at higher frequencies.

To compare with earlier results in the thesis, in this metric the optimized slot has an about 40 % higher k_{opt} than the slot waveguide of the mass sensor, if it had a 50 nm slot width. The improvement is in large part due to a slightly thicker waveguide and removing some unnecessary mass by rounding the outside of the waveguide.

5.6 The fitness landscape

All together about 24000 waveguides were simulated to get to the individual waveguides. This also means that well over 10^6 mode pairs were simulated and evaluated. While this is far less than the more than 10^{113} possible waveguides it is worth speculating on the fitness landscape, at least in the region where the algorithm converged. The hope is that it can work as a background for a discussion about the Brillouin scattering in less common frequency spans or as a part of devices where other metrics than gain play an important role. In a figure showing all the simulated results it is possible to see some of the more general trends and limits. Figure 5.7 shows the gain as dependent on frequency. The colour indicates the group index of the optical mode in the selected mode pair and the results are sorted so a higher group index will cover a lower one.

Something interesting with the figure is that the highest gain mode pairs do not have a high group index. This despite the inverse linear dependency on group velocity and therefore group index shown in the gain equation, equation 5.4. These high gain waveguides are slot waveguides like WG (a), table 5.1.

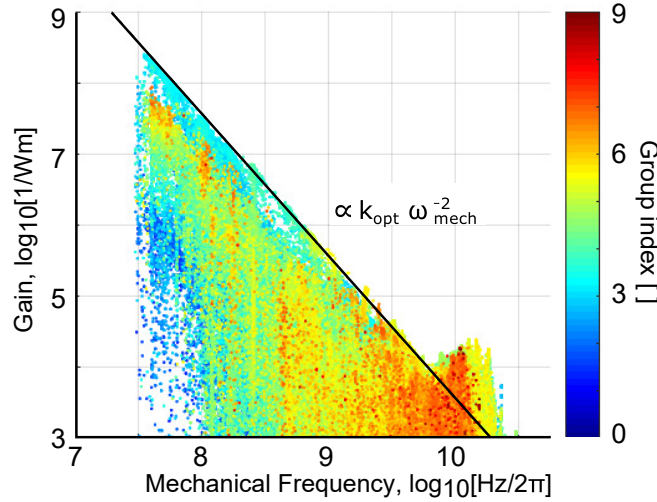


Figure 5.7: The gain, frequency and group index of all simulated mode pairs. The black line indicates the frequency normalised gain of the optimised slot waveguide shown in the inset. The mechanical quality factor is set to 1000.

If we instead focus on the spread in group index, results shown in figure 5.8a, it becomes apparent that while the trend is that a high group index does give a higher gain there is a group of waveguides around a group index of three that performs exceptionally well. It is also visible that this kind of optomechanical mode pairs operates at mechanical frequencies below the lamb wave modes, i.e. WG (g)-(i). Figure 5.8b show that a higher effective mass is needed for a high gain despite its direct contribution in the gain equation, $G \propto m_{eff}^{-1}$. It can be explained by that more moving mass should have a more substantial effect on the optical mode.

Figure 5.9 separates the contribution of the radiation force and the electrostriction. Figure 5.9a shows the two force components with the colour gradient marking the gain. The trend in the data is that for a high gain, strong radiation pressure coupling is paired with a very weak electrostrictive coupling. Achieving a high electrostrictive coupling at a low frequency is difficult. This is because the mechanical frequency depends on the ratio of stiffness to effective mass. The stiffness, in turn, depends on the strain of the mechanical mode normalised to the same point as the effective mass and the Young's modulus. Finally the strain then couples to the optical mode via the electrostrictive constant, so the electrostrictive force depends on an optical overlap with the same strain the mechanical frequency depends on. All together this means that a strong electrostrictive coupling becomes more difficult to achieve the lower the frequency is, see figure 5.9b. The radiation pressure, however, is not as dependent on mechanical frequency, see figure 5.9c,

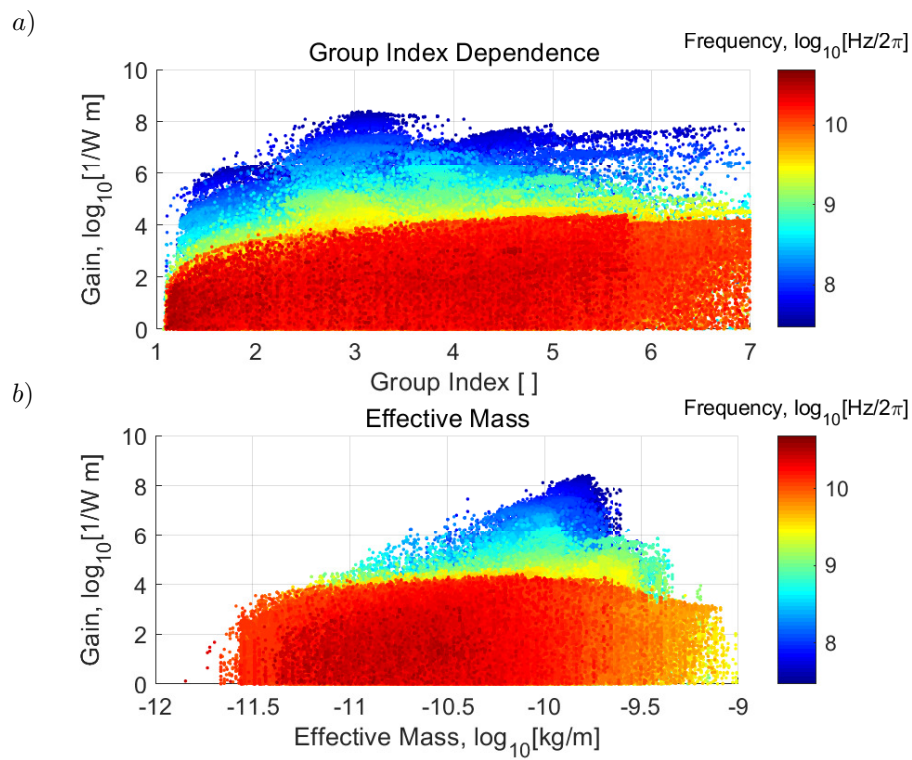


Figure 5.8: a) Gain as a function of group index and (b) effective mass. The color signify mechanical frequency. The effective mass is given relative to the maximum displacement.

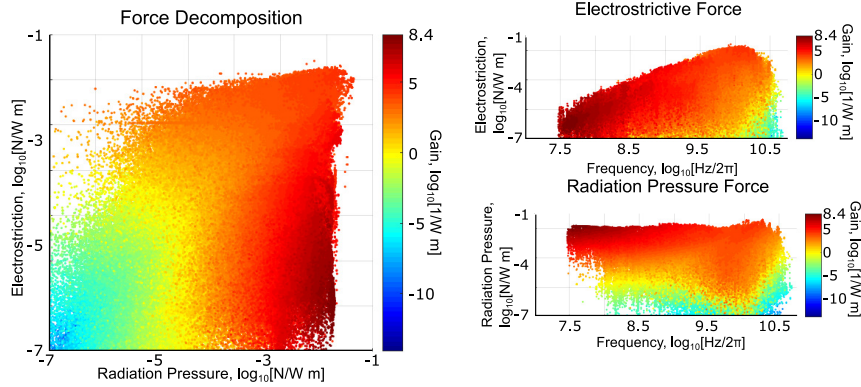


Figure 5.9: The separate power-normalised force components: a) relative to each other as well as b) electrostriction and c) radiation pressure separately. The colour signifies the highest gain found at the indicated place in the graph.

and can be strong in lower frequency WGs.

The electrostrictive contribution is maximised in the high-frequency region, where the highest gain is obtained for variations of wire WGs. The good coupling is due to the excellent overlap between the optical mode and the strain distribution of the mechanical mode as well as the high stiffness. The optomechanical coupling is improved further by a very good radiation pressure coupling.

Figure 5.7 also shows that it is difficult to get a good gain above 20 GHz. This is because the mechanical frequency is increased either by using smaller WGs, where less of the light is confined in the semiconductor, or by using a higher order mechanical mode, which has a worse overlap with the optical mode. In both cases, the optomechanical coupling decreases.

5.7 Conclusion

In this chapter we have discussed the results of the genetic algorithm both in detail about the individual waveguides and about the more general trends visible in the data. The goal was to use genetic algorithms to find new competitive waveguide geometries. Several thousands of waveguides have been simulated and many previously not suggested waveguides have been found and analyzed. As can be expected, slot waveguides where the mechanics and the optics can be separated are the best performing waveguides in the lower frequency range. However, several variations of the slot waveguide design have been shown to have their own advantages. Some slot waveguides exhibit a high group index, others have high electrostrictive coupling or by designing for a higher order optical mode allow to tailor the mode for a high coupling and a lower effective mass. We show several

waveguides that have a gain exceeding $10^8 \frac{1}{Wm}$, well above any previously demonstrated SBS WG. For higher frequencies, wire waveguides take over and generate the highest gain as they have a better optical overlap with the strain resulting in a much stronger electrostrictive coupling.

References

- [1] Wenjun Qiu, Peter T Rakich, Heedeuk Shin, Hui Dong, Marin Soljačić, and Zheng Wang. *Stimulated Brillouin scattering in nanoscale silicon step-index waveguides: a general framework of selection rules and calculating SBS gain*. *Optics express*, 21(25):31402–31419, 2013.
- [2] Raphaël Van Laer, Bart Kuyken, Dries Van Thourhout, and Roel Baets. *Analysis of enhanced stimulated Brillouin scattering in silicon slot waveguides*. *Optics letters*, 39(5):1242–1245, 2014.
- [3] Shirin Ghaffari, Saurabh A Chandorkar, Shasha Wang, Eldwin J Ng, Chae H Ahn, Vu Hong, Yushi Yang, and Thomas W Kenny. *Quantum limit of quality factor in silicon micro and nano mechanical resonators*. *Scientific reports*, 3:3244, 2013.
- [4] Ye Tao, Paolo Navaretti, Roland Hauert, Urs Grob, Martino Poggio, and Christian L Degen. *Permanent reduction of dissipation in nanomechanical Si resonators by chemical surface protection*. *Nanotechnology*, 26(46):465501, 2015.
- [5] Vilson R Almeida, Qianfan Xu, Carlos A Barrios, and Michal Lipson. *Guiding and confining light in void nanostructure*. *Optics letters*, 29(11):1209–1211, 2004.
- [6] Raphaël Van Laer, Bart Kuyken, Dries Van Thourhout, and Roel Baets. *Interaction between light and highly confined hypersound in a silicon photonic nanowire*. *Nature Photonics*, 9(3):199, 2015.
- [7] Nils T Otterstrom, Ryan O Behunin, Eric A Kittlaus, Zheng Wang, and Peter T Rakich. *A silicon Brillouin laser*. *Science*, 360(6393):1113–1116, 2018.
- [8] Raphaël Van Laer and Amir Safavi-Naeini. *Enabling strong coupling in nanoscale silicon optomechanical waveguides*. In *Lasers and Electro-Optics (CLEO), 2017 Conference on*, pages 1–2. IEEE, 2017.

6

Conclusions and perspectives

6.1 Conclusions

In this PhD research, we have investigated the potential of using slot waveguides as inertia mass sensors and designed novel waveguides for Brillouin scattering with the help of genetic algorithms.

In the first half, we have designed and fabricated an all-optically actuated and transduced inertia mass sensor. Both transduction and detection is optically broadband and the displacement sensitivity is measured over a span of 35 nm. The fabrication process has few steps, is CMOS compatible and it is able to operate without optical amplifiers, which should make fabricating the sensor much cheaper. The measured mass sensitivity is in line with published sensors [1, 2] and previously suggested all-photonicallly transduced mass sensors [3, 4] while using a significantly smaller pump power.

The following half, about the findings from the genetic algorithm show that this approach can generate a wide range of competitive stimulated Brillouin scattering waveguides. The best waveguides show a gain $> 10^8$, far beyond what previously has been demonstrated. By filtering the fitness function for a chosen frequency span we show that the algorithm can be altered to search a chosen parameter span or to converge towards waveguides that otherwise would be outcompeted by more competitive waveguides. We also provide a way to significantly speed up the optimization process by reusing the results of previous simulations. This way we managed to find several novel SBS waveguides, such as waveguides with a high group index or higher order slot modes where the radiation pressure coupling is

better.

We also managed to show some of the overarching trends for possible Brillouin waveguide designs, such as the difficulty of generating a high electrostrictive pressure at lower mechanical frequencies while the radiation pressure is significant down to arbitrarily lower mechanical frequencies. Plotting the gain against the mechanical frequency shows that there is a significant bump in gain just above 10 GHz. This is largely due to the electrostrictive pressure increasing with frequency and catching up in magnitude with the radiation pressure. It also shows the cut-off where a smaller waveguide, with a higher fundamental mechanical frequency, is worse at confining the optical mode and therefore reducing the electrostrictive coupling.

In this final chapter, we summarize the main conclusions of this work and elucidate promising roads for future research.

6.2 Future Work

6.2.1 A full integration of the mass sensor

Currently only the sensor itself and the routing to and from the sensor is on-chip. There is work underway to also integrate light sources, both for driving the sensor and detecting the vibration, as well as filters and photo-detectors. If successful this demonstrates the simultaneous integration all of the associated optical components on-chip. Avoiding the coupling losses from going in and out of the chip is expected to result in a vast improvement in the overall performance of the sensor.

6.2.2 A more robust mass sensor

One of the main problems with the longer slot waveguide mass sensors is that they collapse if dried in water. The narrow gap between the cantilevers is necessary for a slot waveguide but it makes stiction a problem. This can be extended to all demonstrated non-resonant optical drives for mass sensing as they in one way or another rely on the attractive force between two waveguides in the optical near-field. One option to get around this is to use the centrifugal force acting upon the waveguide as it guides light through a waveguide bend. The forces would be smaller but such a design with a broader waveguide would be possible to combine with on-chip Raman sensors, e.g. [5]. It would provide a way to cross reference a Raman signal against the deposited mass.

Another way of integrating a Raman sensing capacity to the mass sensor that simultaneously would increase the driving force would be to coat the slot waveguide in gold [6] and then with an anisotropic etch method like reactive ion etching (RIE) remove the gold facing upwards. This removes the gold connecting the two

sides of the slot. Even a fairly short stretch of gold gives a significant Raman signal and the broadband resonance enhances the optical field strength and thus the force.

6.2.3 Expanding the genetic algorithm

Expanding the genetic algorithm to other material combinations would be interesting. Several of the waveguides found have significant radiation pressure and electrostriction coupling but the components are counteracting each other. A material with a different sign of the elasto-optic coupling coefficient would perform very differently e.g. chalcogenide. A list of elasto-optic coupling coefficients can be found in table 2.2. Combining materials with different electrostrictive constants might also allow for higher order mechanical modes to have a high gain. By locally matching the material to the sign of the strain the force would add up constructively.

Finally, designing waveguides for inter-modal SBS is more complex than intra-modal SBS and there are even fewer waveguides were it has been demonstrated [7]. Since it offers a way to achieve single-sideband forward propagating SBS a good selection of waveguides for inter-modal SBS would be a fascinating prospect for a applications that require an energy efficient process as light is not lost to other sidebands.

References

- [1] E Forsen, G Abadal, Sara Ghatnekar-Nilsson, J Teva, J Verd, R Sandberg, W Svendsen, Francesc Perez-Murano, J Esteve, E Figueras, et al. *Ultrasensitive mass sensor fully integrated with complementary metal-oxide-semiconductor circuitry*. Applied Physics Letters, 87(4):043507, 2005.
- [2] Gabriel Vidal-Álvarez, Jordi Agustí, Francesc Torres, Gabriel Abadal, Núria Barniol, Jordi Llobet, Marc Sansa, Marta Fernández-Regúlez, Francesc Pérez-Murano, Álvaro San Paulo, et al. *Top-down silicon microcantilever with coupled bottom-up silicon nanowire for enhanced mass resolution*. Nanotechnology, 26(14):145502, 2015.
- [3] Mo Li, WHP Pernice, and HX Tang. *Broadband all-photonic transduction of nanocantilevers*. Nature nanotechnology, 4(6):377, 2009.
- [4] Dmitry Yu Fedyanin and Yury V Stebunov. *All-nanophotonic NEMS biosensor on a chip*. Scientific reports, 5:10968, 2015.

- [5] Frédéric Peyskens, Pieter Wuytens, Ali Raza, Pol Van Dorpe, and Roel Baets. *Waveguide excitation and collection of surface-enhanced Raman scattering from a single plasmonic antenna*. *Nanophotonics*, 7(7):1299–1306, 2018.
- [6] Ali Raza, Stéphane Clemmen, Pieter Wuytens, Muhammad Muneeb, Michiel Van Daele, Jolien Dendooven, Christophe Detavernier, Andre Skirtach, and Roel Baets. *ALD assisted nanoplasmonic slot waveguide for on-chip enhanced Raman spectroscopy*. *APL Photonics*, 3(11):116105, 2018.
- [7] Eric A Kittlaus, Nils T Otterstrom, and Peter T Rakich. *On-chip inter-modal Brillouin scattering*. *Nature communications*, 8:15819, 2017.

